Publication No. FHWA-HIF-18-062
Infrastructure Office of Bridges and Structures
September 2018

A Performance Based Approach for Loading Definition of Heavy Vehicle Impact Events

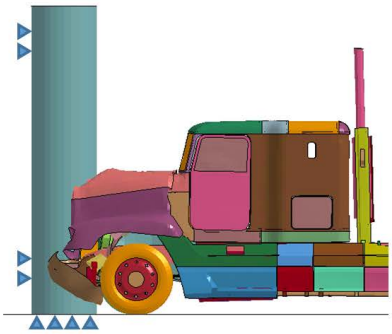

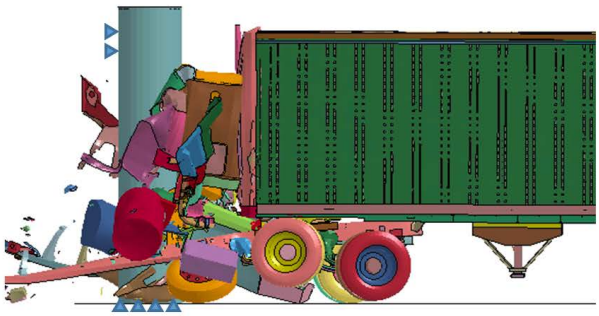

U.S. Department of Transportation
Federal Highway Administration

FOREWORD

This report presents a performance-based approach for designing a bridge pier subject to impact by a tractor-semi-trailer weighing up to 80,000 lbs, based on an extensive experimental and computational investigation. This work is important because bridge failure data compiled by the New York State Department of Transportation, indicate that collision, caused by vessels and vehicles, is the second leading cause of bridge failures after hydraulic causes. The current AASHTO-LRFD (2012) specifications recommend designing a bridge pier vulnerable to vehicular impacts for an equivalent static force of 600 kips (2,670 kN) applied in a horizontal plane at a distance of five feet above the ground level. However, the provisions do not account for the dynamic interaction that occurs between the colliding vehicle and bridge structure. More importantly, they do not articulate an impact-resistant performance philosophy or strategy, nor do they recognize the effects of vehicle characteristics on the equivalent static force.

The work reported herein addresses these limitations of the AASHTO-LRFD specifications for designing bridge piers against impact by heavy vehicles. A performance based approach that relates demands (in terms of the applied force time histories) and capacity (in terms of acceptable shear distortion and plastic rotation) is developed for the design of bridge piers vulnerable to heavy vehicle impact. This report will be of interest to bridge program personnel from Federal, State and local agencies as well as to parties engaged in bridge-related research, and the practicing bridge engineering community. The findings and recommendations will also support future development of the AASHTO Guide Specifications using the proposed approach.

Cheryl Allen Richter, P.E., PhD.
Director, Office of Infrastructure
Research and Development

1. Report No. FHWA-HIF-18-062	**2. Government Accession No.**	**3. Recipient's Catalog No.**
4. Title and Subtitle A Performance-Based Approach for Loading Definition of Heavy Vehicle Impact Events		**5. Report Date** May 2018 **6. Performing Organization Code:**
7. Author(s) Agrawal, A.K., El-Tawil, S., Cao, R., Xu, X., Chen, X. and Wong, W.		**8. Performing Organization Report No.**
9. Performing Organization Name and Address The City College of New York 160 Convent Ave, New York, NY 10031		**10. Work Unit No.** **11. Contract or Grant No.** DTFH61-14-D-00010/0003
12. Sponsoring Agency Name and Address Office of Research, Development, and Technology Federal Highway Administration 6300 Georgetown Pike McLean, VA 22101-2296		**13. Type of Report and Period** Final Report, 08/05/2014-08/04/2017 **14. Sponsoring Agency Code**
15. Supplementary Notes		

16. Abstract

Based on bridge failure data compiled by the New York State Department of Transportation, collision, both caused by vessels and vehicles, is the second leading cause of bridge failures after hydraulic. The current AASHTO-LRFD (2012) specification recommends designing a bridge pier vulnerable to vehicular impacts for an equivalent static force of 600 kips (2,670 kN) applied in a horizontal plane at a distance of 5.0 feet above the ground level. This report presents a performance-based approach for designing a bridge pier subject to impact by a tractor-semi-trailer weighing up to 80,000 lb based on an extensive experimental and computational investigation. The mechanics and modes of failure of bridge pier bents during vehicular impacts are investigated through two pendulum impact tests on a large scale physical model of a three-column bent system. The parameters of the computational model are calibrated to these two tests and further validated through comparisons to other published small-scale impact tests. Through extensive numerical simulation of heavy vehicle (tractor-semitrailer) impacts on piers, the impact force time histories are proposed in the form of analytical triangular pulse functions. The parameters of these functions are derived through numerical regression based on the simulation results. A performance-based approach that relates demands (in terms of the applied force time histories) and capacity (in terms of acceptable shear distortion and plastic rotation) is proposed for the design of bridge piers vulnerable to heavy vehicle impact. Since many collision failures have been observed to be dominated by shear failure, the proposed performance-based approach uses capacity design concepts from earthquake engineering to mitigate collapse by minimizing shear distortion of piers impacted by heavy vehicles.

17. Key Words Vehicular impacts, truck impacts on bridge piers, performance-based approach, heavy vehicle impact event	**18. Distribution Statement** No restrictions. This document is available to the public through the National Technical Information Service, Springfield, VA 22161. http://www.ntis.gov		
19. Security Classif. (of this report) Unclassified	**20. Security Classif. (of this page)** Unclassified	**21. No. of Pages**	**22. Price**

Form DOT F 1700.7 (8-72) Reproduction of completed page authorized

SI* (MODERN METRIC) CONVERSION FACTORS

APPROXIMATE CONVERSIONS TO SI UNITS

Symbol	When You Know	Multiply By	To Find	Symbol
		LENGTH		
in	inches	25.4	millimeters	mm
ft	feet	0.305	meters	m
yd	yards	0.914	meters	m
mi	miles	1.61	kilometers	km
		AREA		
in^2	square inches	645.2	square millimeters	mm^2
ft^2	square feet	0.093	square meters	m^2
yd^2	square yard	0.836	square meters	m^2
ac	acres	0.405	hectares	ha
mi^2	square miles	2.59	square kilometers	km^2
		VOLUME		
fl oz	fluid ounces	29.57	milliliters	mL
gal	gallons	3.785	liters	L
ft^3	cubic feet	0.028	cubic meters	m^3
yd^3	cubic yards	0.765	cubic meters	m^3
	NOTE: volumes greater than 1000 L shall be shown in m^3			
		MASS		
oz	ounces	28.35	grams	g
lb	pounds	0.454	kilograms	kg
T	short tons (2000 lb)	0.907	megagrams (or "metric ton")	Mg (or "t")
		TEMPERATURE (exact degrees)		
°F	Fahrenheit	5 (F-32)/9 or (F-32)/1.8	Celsius	°C
		ILLUMINATION		
fc	foot-candles	10.76	lux	lx
fl	foot-Lamberts	3.426	$candela/m^2$	cd/m^2
		FORCE and PRESSURE or STRESS		
lbf	poundforce	4.45	newtons	N
lbf/in^2	poundforce per square inch	6.89	kilopascals	kPa

APPROXIMATE CONVERSIONS FROM SI UNITS

Symbol	When You Know	Multiply By	To Find	Symbol
		LENGTH		
mm	millimeters	0.039	inches	in
m	meters	3.28	feet	ft
m	meters	1.09	yards	yd
km	kilometers	0.621	miles	mi
		AREA		
mm^2	square millimeters	0.0016	square inches	in^2
m^2	square meters	10.764	square feet	ft^2
m^2	square meters	1.195	square yards	yd^2
ha	hectares	2.47	acres	ac
km^2	square kilometers	0.386	square miles	mi^2
		VOLUME		
mL	milliliters	0.034	fluid ounces	fl oz
L	liters	0.264	gallons	gal
m^3	cubic meters	35.314	cubic feet	ft^3
m^3	cubic meters	1.307	cubic yards	yd^3
		MASS		
g	grams	0.035	ounces	oz
kg	kilograms	2.202	pounds	lb
Mg (or "t")	megagrams (or "metric ton")	1.103	short tons (2000 lb)	T
		TEMPERATURE (exact degrees)		
°C	Celsius	1.8C+32	Fahrenheit	°F
		ILLUMINATION		
lx	lux	0.0929	foot-candles	fc
cd/m^2	$candela/m^2$	0.2919	foot-Lamberts	fl
		FORCE and PRESSURE or STRESS		
N	newtons	0.225	poundforce	lbf
kPa	kilopascals	0.145	poundforce per square inch	lbf/in^2

* SI is the symbol for the International System of Units. Appropriate rounding should be made to comply with Section 4 of ASTM E380. (Revised March 2003)

TABLE OF CONTENTS

LIST OF FIGURES

LIST OF TABLES

LIST OF ABBREVIATIONS

AASHTO	American Association of State Highway and Transportation Officials
ACI	American Concrete Institute
ASCE	American Society of Civil Engineers
ASTM	(formerly American Society for Testing and Materials)
CCNY	City College of New York
CP	Collapse Prevention
CSCM	Continuous Surface Cap Model
D/C	demand/capacity
FE	finite element
FEM	finite element method
FHWA	Federal Highway Administration
FOIL	Federal Outdoor Laboratory
HSLA	high-strength low-alloy
IO	Immediate Occupancy
KCC	Karagozian & Case Concrete
LRFD	load and resistance factor design
NHTSA	National Highway Traffic Safety Administration
NRB	nodal rigid body
NTSB	National Transportation Safety Board
PBD	performance-based design
PR	plastic rotation
SAE	Society of Automotive Engineers
SD	shear distortion
TTI	Texas Transportation Institute

CHAPTER 1. INTRODUCTION

BACKGROUND

Highway bridges form critical nodes in the transportation infrastructure network and are exposed to various types of hazards, e.g., earthquakes, hurricanes, floods, impacts, etc. Based on 2016 National Bridge Inventory Database available at FHWA[1], there are a total of 614,387 bridges in the United States. Quoting from the National Highway Traffic Safety Administration (NHTSA) Fatal Accident Reporting System, a 1994 National Transportation Safety Board (NTSB) study noted that "The NHTSA estimates that annually 1,000 trucks and buses (10,000 pounds gross weight or greater) collide with bridge structures" (Zimmerman 2012). Based on bridge failure data compiled by New York State Department of Transportation, figure 1 shows causes of bridge failures in the United States between 1967 and 2006 (Lee et al. 2006). It is observed that collision, both caused by vessel and vehicles, is the second leading cause of bridge failures after hydraulic.

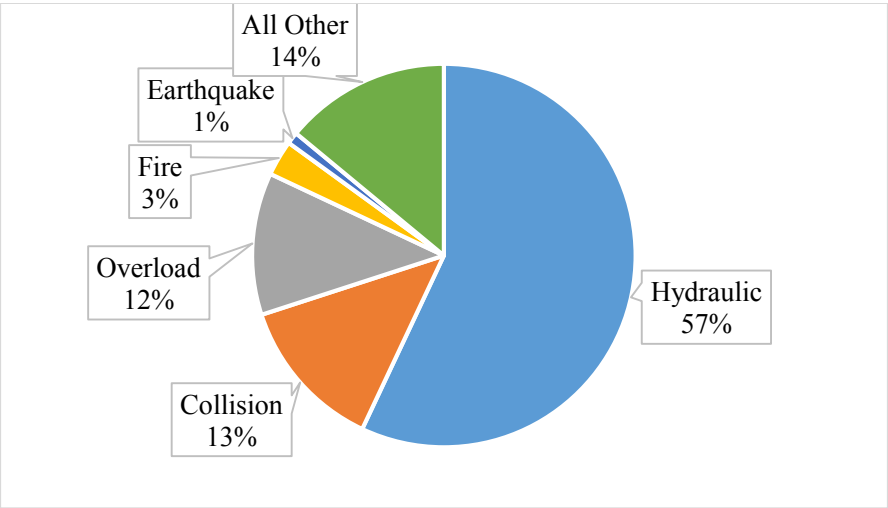

Figure 1. Chart. Causes of failure of bridges.

A significant rise in vehicular collision on bridges has been reported in the United States as well as in other parts of the world. Harik et al. (1990) analyzed 114 bridge failures in the United States over a 38-year period (1951-1988). They found that approximately 17 out of 114 failures (15%) were due to the truck collision. In a similar study, Wardhana and Hadipriono (2003) analyzed 503 bridge failures over an 11-year period (1989-2000) and reported that 14 (3%) bridge failures were caused by collisions of trucks or other vehicles. Agrawal and Chen (2011) carried out a survey of transportation agencies to gauge their concern about the impact of over-height vehicles on highway bridges. They noted that a majority of highway agencies in the United States found the impact on bridges by trucks a major concern, as shown in figure 2.

[1] https://www.fhwa.dot.gov/bridge/nbi/ascii.cfm

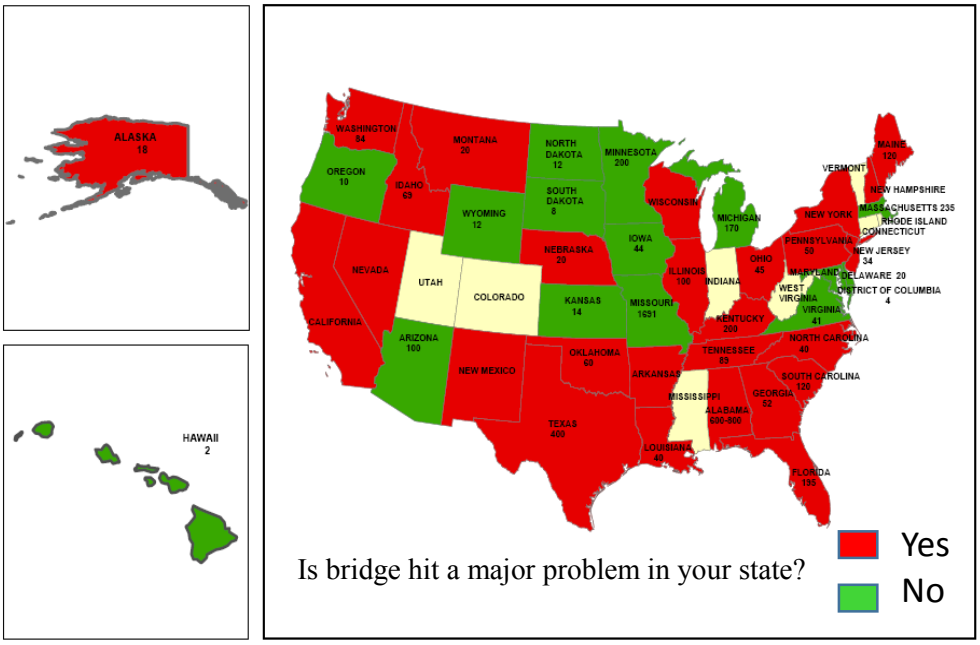

Figure 2. Graph. Survey of vehicle impacts on bridges in United States.

Vehicular impacts on bridge piers can have serious implications in terms of loss of human lives and on the economy (Joshi and Gupta 2012). For example, figure 3 shows the impact by a medium weight moving truck on the piers of the Tancahua Street Bridge over IH-37 in Corpus Christi, Texas, on May 14, 2004. As a result of this impact, one pier of the bridge was destroyed, although the bridge didn't collapse. Figure 4 shows the effect of truck impact on piers of the FM 2110 bridge over IH-30, Texarkana, Texas on August 8, 1994, where two spans of the bridge collapsed. A number of such accidents have been documented in Buth et al. (2010) and Xu (2017).

Figure 3. Photo. Truck impact on piers of Tancahua Street Bridge over IH-37, Corpus Christi, Texas on May 14, 2004.

Figure 4. Photo. Truck impact on FM 2110 bridge over IH-30, Texarkana, Texas on August 8, 1994.

To address the threat to the safety of bridges vulnerable to vehicular impacts, bridge design codes in the United States have provisions that implicitly or explicitly address the impact by trucks on piers. For example, New York State Department of Transportation has been using a Collision Vulnerability Manual [NYSDOT (1996)]. This manual presents an approach to estimate collision vulnerability of bridge piers based on pier type, the presence of protective barriers, structural redundancy, the volume of truck traffic, posted the speed limit, etc. However, this guideline is based on qualitative measures and doesn't take into account failure modes of the piers undergoing impact.

Older versions of the AASHTO-LRFD specifications, e.g., AASHTO-LRFD (1998), recommend designing bridge piers to resist an equivalent 400 kips (1,780 kN) static force when bridge piers are not protected by a crashworthy barrier and are located within a distance of 33 ft (10 m) to the edge of a roadway. This 400 kips (1,780 kN) static force should be applied 4.4 ft (1.35 m) above the ground level. In newer versions of the specifications, e.g., AASHTO-LRFD (2012), abutments and piers located within a distance of 30.0 ft (9.15 m) to the edge of roadway, or within a distance of 50.0 ft (15.25 m) to the centerline of railway track are required to be investigated for collision. Based on two full-scale truck impacts on rigid piers by Buth et al. (2011), AASHTO-LRFD (2012) recommends an equivalent static force of 600 kips (2,670-kN), instead of the 400 kips (1,780-kN) in earlier versions of the provisions, to be applied at a distance of 5.0 ft (1.52 m) above the ground level. Because of the concern related to vague justifications for the AASHTO-LRFD Specifications, Minnesota State DOT, the Bridge Office of Substructure Protection Policy comments that the vehicle collision article of AASHTO-LRFD is overly restrictive because it does not include any variation in requirement due to the probability of vehicle impact.

The understanding of damage modes of a bridge or its components after the collision is crucial for bridge safety assessment and its effect on the local transportation network. Full scale verification of impacts on bridges is difficult because of the high costs associated with such tests and logistical problems associated with conducting full-scale tests on bridge structures. An effective alternative is to carry out high fidelity numerical simulation using test data obtained

from small tests. EI-Tawil et al. (2005) simulated two truck models of 3,150-lb (14 KN) and 15,000-lb (66 KN) weight colliding with elastic piers at various approach speeds. Although finite element models of the vehicle in the study included nonlinear material properties, this study considered concrete as an elastic material.

Boundary condition restraints provided by the bridge superstructure can influence dynamic behaviour of bridge piers during impact. Buth et al. (2010) simulated vehicle impact on round rigid piers of 24 in (610 mm), 36 in (915 mm) and 48 in (1,220 mm) diameters. Buth et al. (2011) conducted two full-scale crash tests with an 80,000-lb van-type tractor-semitrailer impacting an instrumented rigid bridge pier at 50 mph, as shown in figure 5. Ballast in the trailer consisted of bags of sand on pallets distributed throughout the trailer. Analyses of the data indicate that the equivalent static force reaches 700 kips over a very short time duration.

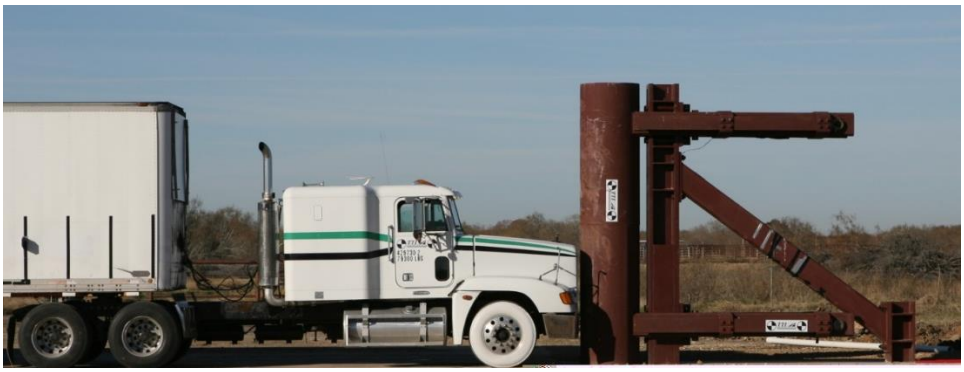

Figure 5. Photo. Full-scale crash tests with an 80,000-lb van-type tractor-semitrailer impacting an instrumented rigid bridge pier at 50 mph at Texas Transportation Institute.

Steel and Sorenson (2012) conducted a first-order, second-moment reliability analysis of circular bridge piers subjected to intentional vehicular impact through Monte Carlo simulation. They used five different vehicle classes to represent the likely vehicles types to participate in the impact event to identify reinforcement area, vehicle speed, and vehicle mass as factors contributing the most to the failure of a bridge pier. Sharma et al. (2012) investigated a performance-based response evaluation of reinforced concrete columns subject to vehicle impact, where the dynamic shear capacity of bridge piers was calculated through finite element simulation of impact of a design vehicle with different speeds. Their work shows that the dynamic shear capacity depends on the structural properties of piers as well as loading characteristics (e.g., velocity and inertia) and can be higher than the static capacity calculated based on codes. Sharma et al. (2014) developed a framework for performance-based analysis and design of RC columns subject to vehicle impact. Their approach involved a probabilistic model to accurately estimate the dynamic shear force demand on RC columns subjected to vehicular impact and estimation of the fragility of the columns.

Chung et al. (2014) investigated vehicular impact on precast prefabricated bridge columns by developing a five-point piecewise linear approximation function to represent impact loading. They used this loading function to compare the performance of cast-in-place reinforced concrete bridge columns and prefabricated bridge columns subjected to vehicular impacts. Recent studies by Liu (2012), Agrawal et al. (2013), Chen et al. (2016a), Chen et al. (2016b) and Xu (2017)

considered the impact of single unit trucks with total weight around 15,000 lb (66 kN) impacting bridge piers directly. These studies investigated the behaviour of bridge piers during vehicular impacts, various damage modes during vehicular impacts and performance guideline for design of bridge piers against vehicular impacts. For example, Liu (2012) investigated the impact of a single unit truck model in LS-DYNA on piers of a three span bridge with three column pier bent. The numerical model of the bridge with the truck is shown in figure 6. Based on numerical simulation of vehicular impact on bridge piers at various speed, he identified six damages mechanisms present during impact of the single unit truck with piers of a bridge. These damage mechanisms are illustrated in figure 7 and are: pier eroding, shear at footing, rebar severance, breakage of pier, spalling of pier and plastic hinge formation. Among these damage mechanisms, shear at footings, breakage of pier and plastic hinge formation can be considered as having potential for severe damage that may lead to collapse. Liu (2012) also presented a preliminary framework for a performance-based design approach; however, this approach didn't quantify damage levels.

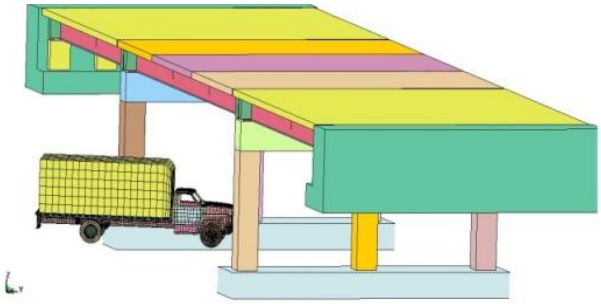

Figure 6. Photo. LS-DYNA model of the bridge with single unit truck.

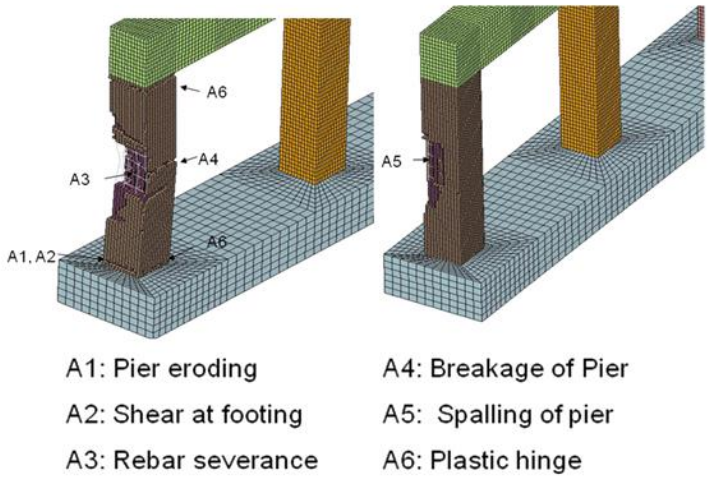

Figure 7. Photo. Damage modes present during impact of single unit truck with bridge piers.

An experimental study on impact to anti-ram bollards by a truck was carried out by Chen et al. (2015) at Hunan University, China. A Dongfeng EQ140 truck with a net weight of 11,400 lb

(5,170 kg) was selected to hit five 4.27 ft (1,300 mm) high concrete-filled steel tube columns with an outer diameter of 8.6 in (219 mm). The thickness of steel tube was 0.8 in (20 mm), and 6 ksi (C40) concrete was filled in the steel tube. The initial impact velocity of the truck was recorded as 43.2 km/h. The collision truck was crashed straight into the middle bollard. As noted from figure 8, the truck was damaged severely during the impact. Although the static capacity of the bollard was 79 kips (350 KN), which was one tenth of the average impact force of 822 kips (3,660 KN), the columns didn't undergo large deformation with a residual displacement of 1.3 in (33 mm) (a drift ratio of 2.54%).

Figure 8. Photo. Anti-ram bollard impact field test.

Abdelkarim and Elgawady (2016a) and Abdelkarim and Elgawady (2017) investigated the behavior of reinforced concrete bridge columns subjected to vehicle collision through an extensive parametric study to derive an equation for equivalent static force (ESF). This study found that the constant 600 kips (2,670 kN) force prescribed in the AASHTO load and resistance factor design was not conservative when the vehicle's velocity exceeded 75 mph and when the vehicle's weight exceeded 30 kips (134 kN). Abdelkarim and Elgawady (2016b) investigated the behavior of hollow-core fiber-reinforced polymer–concrete–steel (HC-FCS) columns, which are used for accelerated bridge construction, under vehicle collision. The HC-FCS columns consist of a concrete wall sandwiched between an outer fiber-reinforced polymer (FRP) tube and an inner steel tube. Research shows that the main resistance of the HC-FCS columns to the vehicle collision came from the inner steel tube. AuYeung and Alipour (2016) investigated the structural response of reinforced concrete bridge piers subjected to vehicle collisions using the single unit truck model offered by the National Crash Analysis Center and the National Transportation Research Center. This study showed that a multi-pier bent changes the trend of absorption of kinetic energy, failure modes, and distribution of impact forces, especially for lower impacting speeds. A multi-pier configuration results in higher impact forces but, due to higher stiffness, results in low lateral displacements, and higher resistance to shear and moment forces.

RESEARCH MOTIVATION AND NEEDS

It is noted from the discussion above that a number of research studies have been carried out during the last few years on vehicular collision with bridge piers. However, with the exception of the Buth et al. (2011) study, all of these studies focused on vehicle impact involving single unit trucks. On the other hand, as observed from case studies on truck impacts on bridge piers in Buth et al. (2010), the majority of cases involving truck impact on bridge piers are the heavy vehicles represented by tractor-semitrailers with 80,000 lb (356 kN) or higher weight. The most notable research using these heavy vehicles was carried out by Buth et al. (2011), where they performed two full-scale crash tests of 36 metric ton tractor-semitrailers crashing into rigid piers. Based on the findings from these two tests, AASHTO-LRFD (2012) increased the recommended equivalent static force from 400 kips (1,780 kN) to 600 kips (2,670 kN). However, the current provisions still do not account for the dynamic interaction that occurs between the colliding vehicle and bridge structure. More importantly, they do not articulate an impact-resistant performance philosophy or strategy nor do they recognize the effects of vehicle characteristics on the equivalent static force. For these reasons, further investigation needs to be carried out to address the current limitations of the AASHTO-LRFD specifications for designing bridge piers against impact by heavy vehicles.

RESEARCH OBJECTIVES

The overall objective of this research is to develop comprehensive guidelines for the design of bridge piers subjected to collision by heavy vehicles. Specific objectives include:

- Identification of parameters for the concrete material model in LS-DYNA to represent behavior of concrete in bridge piers during vehicular impact events.
- Thoroughly validating the computational model using existing test data.
- Simulation and impact testing of a large-scale reinforced concrete bent using a pendulum.
- Development of a comprehensive loading model based on an extensive parametric study to represent the effects of truck impact on bridge piers.
- Development of performance-based guidelines for the design of bridge piers impacted by heavy trucks.
- Quantification of performance levels in terms of plastic rotation and shear distortion.

Detailed work performed towards achieving these objectives is described in different chapters of this report as follows:

Chapter 2 describes the calibration of the material model for representing impact behavior.

Chapter 3 describes in detail the planning and results of the large scale testing, including comparison between test results and finite element model.

Chapter 4 presents the development of a proposed pulse loading model to represent tractor-semitrailer impact demands on a bridge pier.

Chapter 5 presents the proposed performance-based guidelines, including the quantification of performance levels.

Chapter 6 presents conclusions and recommendations for future work.

CHAPTER 2. MATERIAL MODEL

LS-DYNA (Hallquist 2006) is a popular general-purpose, multi-physics simulation software package that has been widely used for impact simulations. LS-DYNA provides several concrete constitutive models for analyzing the behavior of reinforced concrete structures under various types of loads. A successful concrete constitutive model should be capable of reproducing the most basic behaviors of concrete (Wu et al. 2012). In particular, it should be capable to modeling crushing behavior, confinement effects, cracking response and the effect of loading rate on all of these responses.

This chapter starts with a description of a number of key material models for representing the behavior of concrete and steel. The survey identifies Mat 159 (Continuous Surface Cap Model, referred to hereafter as CSCM) as one that is feasible for simulating the behavior of concrete structures subjected to dynamic loading. While default material parameters provided in LS-DYNA are commonly used, they do not necessarily produce the best results. Therefore, calibration of user input parameters for this material model is carried out through the simulation of a recent drop hammer test carried out by Fujikake et al. (2009).

CONCRETE AND STEEL MATERIAL MODELS IN LS-DYNA

Concrete material models available in LS-DYNA and their characteristics are summarized in table 1. Based on a literature review and the information in table 1, it is clear that material models Mat 72 (Concrete_Damage) and Mat 159 (Continuous Surface Cap Model) can predict concrete mechanical behavior under impact loading relatively well. Both of these models have the capability to generate default parameters requiring only basic material properties like unconfined compression strength, Poisson's ratio and aggregate size making them attractive alternatives for modeling concrete behavior. Although a detailed description of these two material models is provided in LS-DYNA help manuals, a brief description of these models is provided for the sake of reference.

Table 1. Concrete and steel material models in LS-DYNA.

Mat ID	Mat Name	Characteristics and Implementation
Mat 17	Isotropic Elastic-Plastic With Oriented Cracks	Does not consider the pressure hardening effect, strain rate effects, and damage softening effect. Potential applications include brittle materials such as ceramics as well as porous materials such as concrete in cases where pressure hardening effects are not significant.
Mat 72	MAT_CONCRETE_DAMAGE	Widely used for simulating blast and impact in concrete structures.
Mat 96	Brittle Damage Model	Mainly used to simulate cracks due to tensile stress.
Mat 111	Johnson-Holmquist Concrete Model	Used for concrete subjected to large strains, high strain rates, and high pressure.
Mat 159	Continuous Surface Cap Model	Developed to simulate the deformation and failure of concrete in roadside safety structures impacted by vehicles
Mat 3	Plastic Kinematic	This model is widely used to simulate isotropic and kinematic hardening plasticity considering rate effect.

Material Model 72R3: MAT_CONCRETE_DAMAGE

This model was first developed for DYNA3D to analyze buried steel reinforced concrete structures subjected to impulsive loadings. It became the material model 72R3 in LS-DYNA after a series of improvements. This material model, also known as Karagozian & Case Concrete (KCC) Model-Release III (Magallanes et al. 2010) uses three shear failure surfaces and includes damage and strain-rate effects. This material model is based on the Pseudo-Tensor model (Material Type 16). The KCC model has three independent strength surfaces: yield strength surface, maximum strength surface and residual strength surface. These surfaces are formulated in a generalized form as,

$$F_i(p) = \mathrm{a_{0i}} + \frac{\mathrm{p}}{\mathrm{a_{1i}} + \mathrm{a_{2i}}\mathrm{p}} \tag{1}$$

where i stands for y (yield strength surface), m (maximum strength surface) and r (residual strength surface), and $\mathrm{p} = -I_1/3$ is the pressure. Parameters a_{ji} (j=0, 1, 2) in the equation (1) above are calibrated from test data.

For hardening, the plasticity surface used in the model is interpolated between the yield and maximum surfaces based on the value of damage parameter, λ. For softening, a similar interpolation is performed between the maximum and residual surfaces. After reaching the initial yield surface, but before the maximum failure surface, the current surface is obtained as a linear interpolation between yield and maximum failure surfaces,

$$\Delta\sigma = \eta(\Delta\sigma_m - \Delta\sigma_y) + \Delta\sigma_y \tag{2}$$

where η varies from 0 to 1, depending on the accumulated effective plastic strain parameter λ. In other words, η(λ) is a function of the internal damage parameter λ, with $\eta(0) = 0$, $\eta(\lambda_m) = 1$, $\eta(\lambda \geq \lambda_m) = 0$. This implies that the failure surface starts at the yield strength surface, and it reaches the maximum strength surface as λ increases to λ_m, and then it drops to the residual surface as λ further increases up to λ_{max}. Here, λ_m, λ_{max} and η(λ) relationships are calibrated from experimental data.

Similar to the interpolation of the plasticity surface above, the current failure surface is interpolated between the maximum and the residual surfaces after reaching the maximum surface,

$$\Delta\sigma = \eta(\Delta\sigma_m - \Delta\sigma_r) + \Delta\sigma_r \tag{3}$$

Parameters a_{ji} (j=0, 1, 2; i = y, m, r) can be generated by the default parameter generation function based on the unconfined compressive strength of the concrete. Detailed information regarding these parameters can be found in Magallanes et al. (2010).

Material Model 159: Continuous Surface Cap Model

Material Model 159 is an elasto-plastic damage model for concrete with rate effects. This model was developed for roadside safety applications, such as concrete bridge rails and portable barriers impacted by vehicles (Murray 2007). In this model, a smooth and continuous intersection is formulated between failure surface and hardening cap. Figure 9 shows the general shape of the yield surface in the meridonal plane. Softening and modulus reduction in this model are simulated on the basis of isotropic constitutive equations, yield and hardening surfaces, and damage formulations. A rate effect formulation increases strength with strain rate.

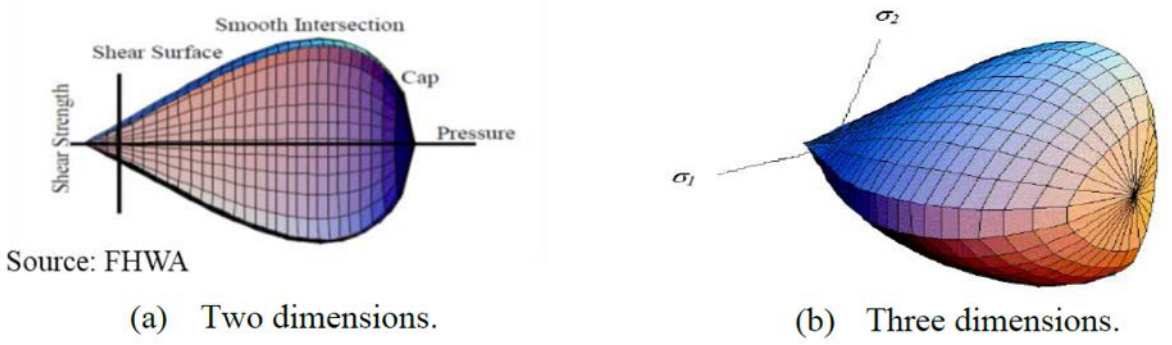

Figure 9. Graph. General shapes of the concrete model shear failure and cap hardening surfaces.

Concrete shows softening in both tensile and low to moderate compressive regimes. In this model, softening is modeled via a damage formulation. This formulation models both strain softening, which is decrease in strength during progressive straining after the peak strength has been reached, and modulus reduction, as shown in figure 10. In this figure, (1-d) factor, where *d* is a scalar damage parameter ranging between 0 for no damage to 1 for complete damage, is a reduction factor that reduces both bulk and shear moduli isotopically. Damage initiates and accumulates when strain-based energy terms exceed the damage threshold. Damage accumulation via the parameter d is based on two distinct formulations of brittle and ductile damage.

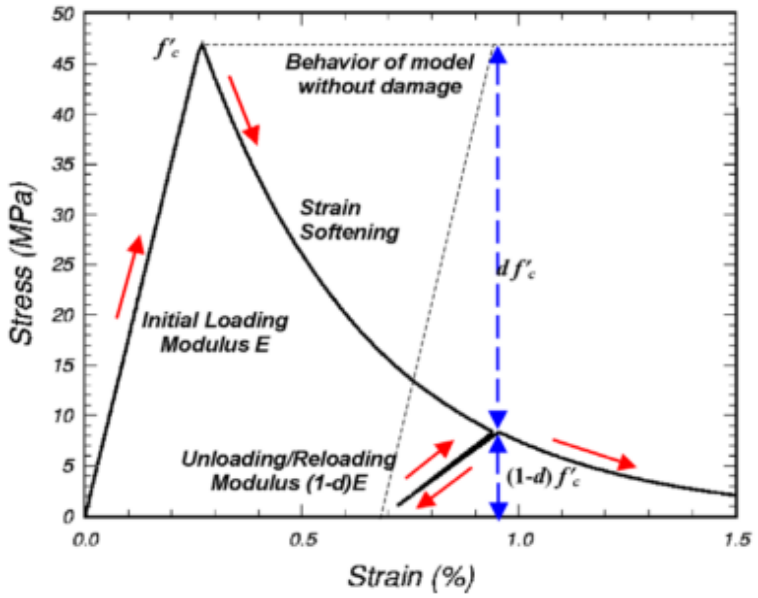

Source: FHWA

Figure 10. Graph. Illustration of strain softening and modulus reduction.

Mat 3: Kinematic Plasticity Model for Steel Rebars

Steel bars are modeled using Hughes-Liu beam elements and are represented using Model 3, which accounts for yielding and kinematic hardening plasticity. Figure 11 shows the elastic-plastic behavior of Model 3 with kinematic and isotropic hardening. In the plot, E_t is the slope of the bilinear stress strain curve. Perfect bond is enforced between steel and concrete components, implying that the effect of bond-slip behavior is assumed to be negligible.

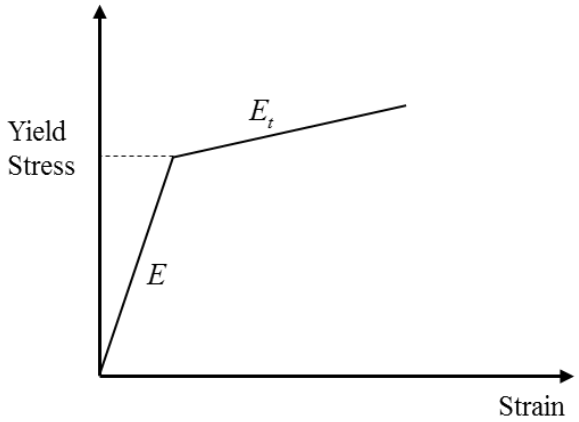

Figure 11. Graph. Elastic-plastic behavior with kinematic and isotropic hardening.

SELECTION OF CONCRETE MATERIAL MODEL

As noted from the discussion above, both Mat 72 and Mat 159 in LS-DYNA could be used for simulation of vehicular impacts on bridge piers. In order to further investigate the suitability of one of these two models, numerical simulations for a single element of concrete are carried out. The single element used here is a 1 inch (25.4 mm) solid element with the bottom four nodes restrained against vertical motion, and prescribed vertical motion applied on the top 4 nodes (see figure 12). The compressive strength of the concrete is 6 ksi (42MPa). Stress is considered positive in tension and negative in compression.

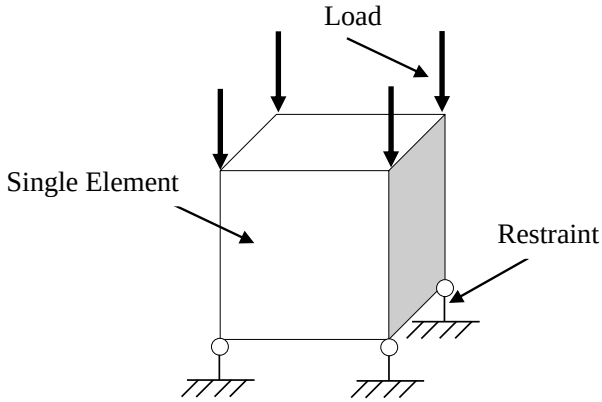

Figure 12. Illustration. Boundary condition and load application for single element simulation.

Figure 13 shows the plot of stress-strain curves for CSCM and 72R3 concrete models under uniaxial tension and uniaxial compression simulations. It can be observed from figure 13(a) that

the stresses using CSCM and 72R3 increase linearly to the peak value with the same slope under uniaxial tension. Maximum tensile strengths for CSCM and 72R3 are approximately 0.4 ksi (3 MPa) and 0.5 ksi (3.5 MPa), respectively. After the tensile stress reaches the maximum value, the tensile stress using CSCM softens smoothly to zero, while the tensile stress using 72R3 model drops almost linearly to zero.

Figure 13(b) shows plots of stress-strain curves for the uniaxial compression simulations. It is observed that the compressive stresses in cases of both CSCM and 72R3 increase linearly to the maximum value of 6 ksi (42 MPa). The slopes of the stress-strain curves for both CSCM and 72R3 are the same. After the compressive stress reaches the maximum value, the compressive stress in case of the CSCM softens gradually, whereas the compressive stress in case of the 72R3 model drops more sharply. Since the stress-strain relationships plots in figure 13 are for a case without any confining pressure, the ductility in case of the CSCM is better than that in case of the 72R3 model.

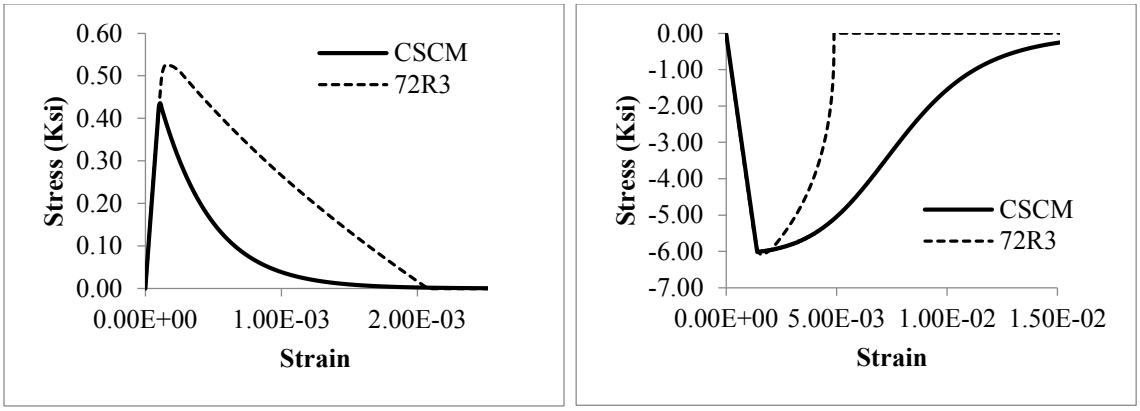

(a) Uniaxial tension. (b) Uniaxial compression.

Figure 13. Graphs. Stress-Strain curves for CSCM and 72R3.

In tri-axial compression simulations, lateral confining pressure around the element is held constant while the axial compressive load is quasi-statically increased. As shown in figure 14, the compressive strengths of both material models will increase with an increase in the confining pressure. This behavior is in qualitative agreement with typical test data. However, the 72R3 material model is more sensitive to the confining pressure changes than the CSCM. Under 1.16 ksi (8 MPa) confinement, the compressive strength in case of the CSCM is 9.57 ksi (66 MPa), which is 57% higher than that for the case without any confinement. In case of the 72R3 material model, this increase is approximately 110% higher than that for the case without any confinement.

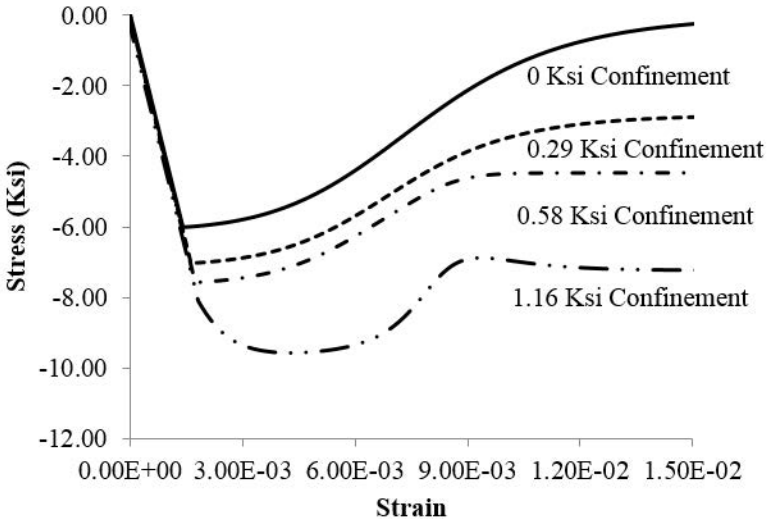

(a) CSCM.

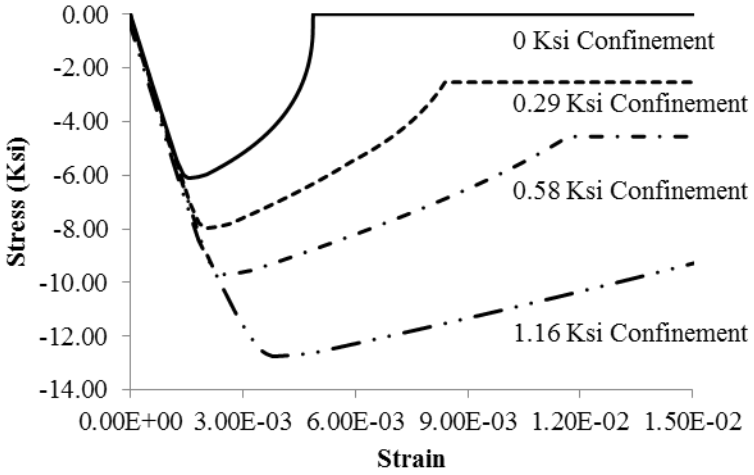

(b) 72R3.

Figure 14. Graphs. Confining effect of concrete models.

The strength of concrete increases with an increase in the strain rate during high speed dynamic loading. The strain rate is normally between 1/s to 10/s during slow speed impacts. Figure 15 shows a plot of the relationship between tensile strength and the strain rate for the CSCM and 72R3 models. It is observed that the tensile strength for the CSCM increases by 79% when the strain rate is 10 /sec, whereas this increase is 200% in case of 72R3.

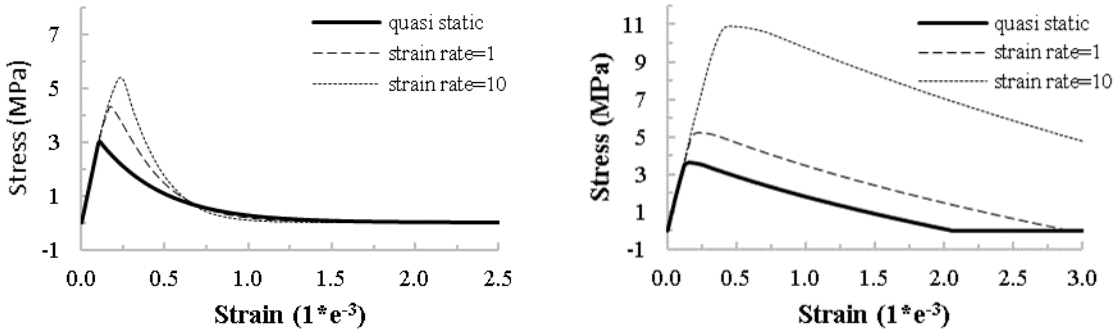

(a) CSCM. (b) 72R3.

Figure 15. Graphs. Relationship between tensile strength and strain rate.

Abu-Odeh (2008) compared the results of two bogie impact tests with finite element simulation results carried out in LS-DYNA. The initial bogie impact speed for the first and second tests are 15 mph and 20 mph, respectively. Damage profiles for the impact tests and LS-DYNA simulations are shown in figure 16 and figure 17 respectively. The barrier was able to absorb the energy of impact with minor damage in the first test, although some minor cracking developed as shown in figure 16(a). The barrier was severely damaged in the second test, as shown in figure 17. The top of the barrier failed around the impact location as shown in figure 17(a). It is clear from figure 16 and figure 17 that the CSCM shows a comparable damage profile to the overall test pattern, whereas 72R3 shows more deformation and a larger damaged area of the barrier than that observed in the test.

Source: Abu-Odeh (2008)

(a) Test. (b) CSCM. (c) 72R3.

Figure 16. Photos. Damage profile for the 15 mph test.

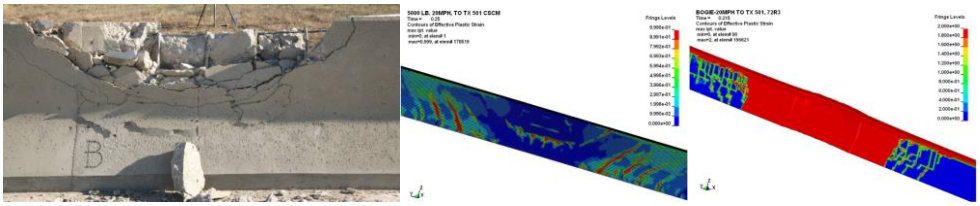

Source: Abu-Odeh (2008)

(a) Test. (b) CSCM. (c) 72R3.

Figure 17. Photos. Damage profile for the 20 mph test.

Based on the results in figure 13 to figure 17, it is concluded that the CSCM more realistically represents the behavior of concrete structures under dynamic loads. As such, the CSCM is

chosen for the simulations conducted in the rest of this report. Calibration of the model is based on test data presented by Fujikake et al. (2009) and confirmed through the large scale bent tests.

CALIBRATION OF CONTINUOUS SURFACE CAP MODEL

The stress-strain analysis of a single concrete element presented in the previous section shows that the CSCM can qualitatively capture key concrete behaviors, including post-peak softening, confining effect, and strain rate effects using the default parameters provided in LS-DYNA. However, these parameters need to be calibrated based on impact tests to ensure that they accurately simulate test conditions.

Input Cards for CSCM

LS-DYNA allows two types of input cards for CSCM. The user has the option of inputting their own material properties, or using default material properties (MAT_CSCM) for normal strength concrete (MAT_CSCM_CONCRETE). In the MAT_CSCM_CONCRETE card, only limited parameters need to be defined, including density, maximum aggregate size, uniaxial compressive strength, and the units. The uniaxial compressive strength affects all aspects of comparisons with test data, including stiffness, three-dimensional yield strength, hardening, and damage-based softening. The aggregate size affects only the softening behavior. The default properties are recommended for use with concrete with unconfined compressive strength between 2.9 ksi (20 Mpa) and 8.41 ksi (58 MPa), and aggregate sizes between 0.31 inch (8 mm) and 0.94 inch (24 mm).

The default material properties were developed without adequate consideration of: 1) softening behavior in pure shear; 2) rate effects for stress states other than uniaxial tensile and compression stresses. The latter point includes the effect of strain rate on fracture energy as well as strength (Murray et al. 2007). The sample input card for MAT_CSCM_CONCRETE is shown in table 2.

Table 2. Sample input card for MAT_CSCM_CONCRETE.

*MAT_CSCM_CONCRETE
$ MID RO NPLOT INCRE IRATE ERODE RECOV ITRETRC
8 2.44e-9 1 0 1 1.1 10 0
$ PRED
$ FPC DAGG UNITS
42 10 2

In the MAT_CSCM card, a user needs to define all input values including moduli, strengths, hardening, softening, and rate effects etc. Default parameters for MAT_CSCM can be obtained from the “d3hsp” file by running the simulation using the default MAT_CSCM_CONCRETE card. A sample input card for MAT_CSCM is shown in table 3.

.

Table 3. Sample input card for MAT_CSCM (compressive strength 42MPa).

*MAT_CSCM							
$ MID	RO	NPLOT	INCRE	IRATE	ERODE	RECOV	ITRETRC
8	2.44e-9	1	0	1	1.1	10	0
$ PRED							
0							
$ G	K	alpha	thita	lamda	beta	Nh	Ch
1.282E+04	1.404E+04	1.570E+01	3.362E-01	1.051E+01	1.929E-02		
$ alpha1	thita1	lamda1	beta1	alpha2	thita2	lamda2	beta2
7.473E-01	7.827E-04	1.700E-01	5.603E-02	6.600E-01	9.439E-04	1.600E-01	5.603E-02
$ R	X0	W	D1	D2			
5	9.724E+01	5.000E-02	2.500E-04	3.492E-07			
$ B	Gfc	D	Gfs	Gft	pwrc	pwrt	pmod
1.000E+02	7.182E-00	1.000E-01	7.182E-02	7.182E-02	5	1	0
$ eta0c	Nc	eta0t	Nt	overc	overt	Srate	repow
1.478E-04	7.800E-01	7.471E-05	4.800E-01	2.805E+01	2.805E+01	1	1

Calibration of CSCM Using Test Data

The dynamic behavior of the CSCM is influenced by rate effects, which is controlled by the parameters in the last line in the user-controlled card. According to Murray et al. (2007) , the user has the option of increasing the fracture energy as a function of effective strain rate through the parameter *repow* as an input parameter as shown in equations 4 and 5,

$$G_f^{rate} = G_f\left(1+\frac{E\dot{\varepsilon}\eta}{f^{'}}\right)^{repow} \tag{4}$$

$$f^{rate} = f^{'} + E\dot{\varepsilon}\eta \tag{5}$$

where G_f is either the brittle or ductile fracture energy calculated from the user-specified input values, $G_f{}^{rate}$ is the value that is scaled up with rate effects, and f' is the yield strength before application of rate effects. The term in brackets is the approximate ratio of the dynamic to static strength. The dynamic strength f^{rate} (viscoplastic) is equal to the static strength (inviscid) plus a dynamic overstress equal to $E\dot{\varepsilon}\eta$, where E is Young's modulus and $\dot{\varepsilon}$ is the effective strain rate and η is the effective fluidity coefficient. In order to fit tensile and compressive strain rate data with different viscoplastic fluidity parameters, four user-specified input parameters are defined. These are η_{0t} and n_t for fitting uniaxial tensile stress data, and η_{0c} and n_c, for fitting the uniaxial compressive stress data. For stress states between uniaxial tensile stress and uniaxial compressive stress, the fluidity parameter is interpolated as a function of stress invariant ratio using the algorithm in figure 18 below.

If the pressure is tensile ($J_1 < 0$)

$$\eta = \eta_s + trans(\eta_t - \eta_s)$$

$$trans = \left[\frac{-J_1}{\sqrt{3J_2'}}\right]^{pwrt}$$

$$trans = \min(1, trans)$$

$$trans = \max(0, trans)$$

If the pressure is compressive ($J_1 \geq 0$)

$$\eta = \eta_s + trans(\eta_t - \eta_s)$$

$$trans = (\frac{J_1}{\sqrt{3J_2'}})^{pwrc}$$

$$trans = \min(1, trans)$$

$$trans = \max(0, trans)$$

Figure 18. Algorithm. Algorithm for interpolation of fluidity parameter in continuous surface cap model.

In the algorithm in figure 18, $\eta_t = \frac{\eta_{0t}}{\dot{\varepsilon}^{n_t}}$, $\eta_c = \frac{\eta_{0c}}{\dot{\varepsilon}^{n_c}}$, $\eta_s = SRATE \cdot \eta_t$. The input parameters are η_{0t} and n_t for fitting uniaxial tensile stress data, η_{0c} and n_c for fitting the uniaxial compressive stress data, and $SRATE$ for fitting shear stress data. The effective strain rate is $\dot{\varepsilon}$. Parameters n_c and n_t are constant parameters in the model, so their default values are adopted. "$SRATE$" is a single input scaling parameter to determine the effective fluidity parameter in shear. A default value of 1 for "$SRATE$" has been adopted in this study. In figure 18, *pwrt* and *pwrc* are two user-defined parameters, which are used for interpolation in tensile-to-shear and shear-to-compression transition respectively.

This viscoplastic model may predict substantial rate effects at high strain rates ($\dot{\varepsilon} > 100$). However, overstress limits in tension (overt) and compression (overc) can be set to limit rate effects at high strain rates. Hence, "overc" and "overt" are set to be a very large value in this study to eliminate their influences.

As shown in equation (4), *repow* is a power coefficient which increases fracture energy with rate effects. An inconsistency has been found concerning the interpretation of the fracture energy (Brara and Klepaczko 2007). Tests performed by Weerheijm (1992) did not reveal an increase in the total fracture energy of concrete with increasing strain rates. On the other hand, Doormaal et al. (1994) found higher fracture energies in the dynamic loading experiments. Because of conflicting information on dependency of fracture energy on strain rate, one can either model fracture energy independent of strain rate ($repow = 0$) or increase the fracture energy with strain rate by multiplying the static fracture energy by the DIF ($repow = 1$) (Murray 2007). With a value of 1, the increase in fracture energy with rate effects is approximately proportional to the increase in the strength with rate effects. According to Murray (2007), fracture energy should be increased with the strain rate; hence, default value of $repow = 1$ has been adopted in this research.

In order to study the dynamic behavior of Mat_159 model, three parameters: “Gfs”, “Gft” and “Gfc” have been calibrated based on data on impact tests performed by Fujikake et al. (2009). In their experiment, an 882 lb (400 kg) hammer was dropped freely onto the top surface of the RC beam at mid-span from different heights. The striking head of the drop hammer had a hemispherical tip with a radius of 3.54 inch (90 mm). The RC beam was supported over a span of 55.11 inch (1,400 mm) with a specially designed devices to allow it to freely rotate while preventing it from moving out of plane. The cross-sectional dimensions of the RC beams are 10 inch (250 mm) in depth, 5.91 inch (150 mm) in width and 66.93 inch (1,700 mm) length, as shown in figure 19. The setup of the RC beam hammer impact test is shown in figure 20.

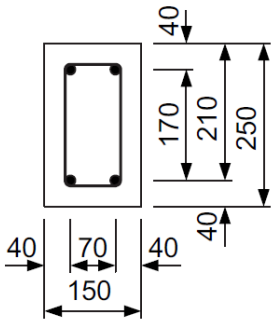

(a) Cross section view.

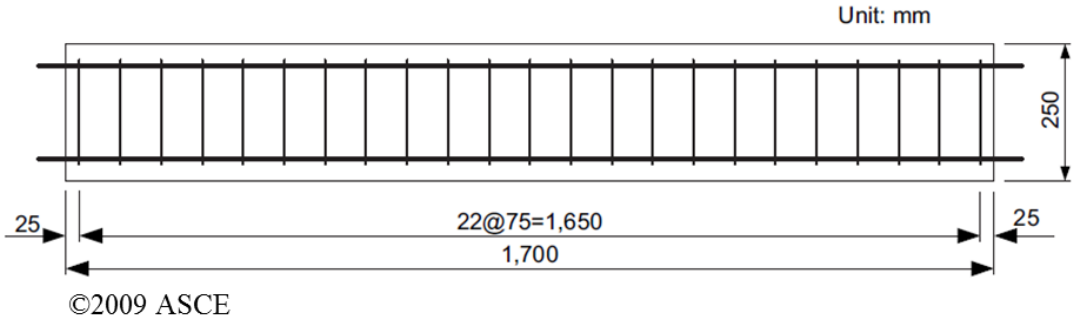

(b) Side view.

Figure 19. Illustration. Geometry and rebar detailing of the RC beam specimen.

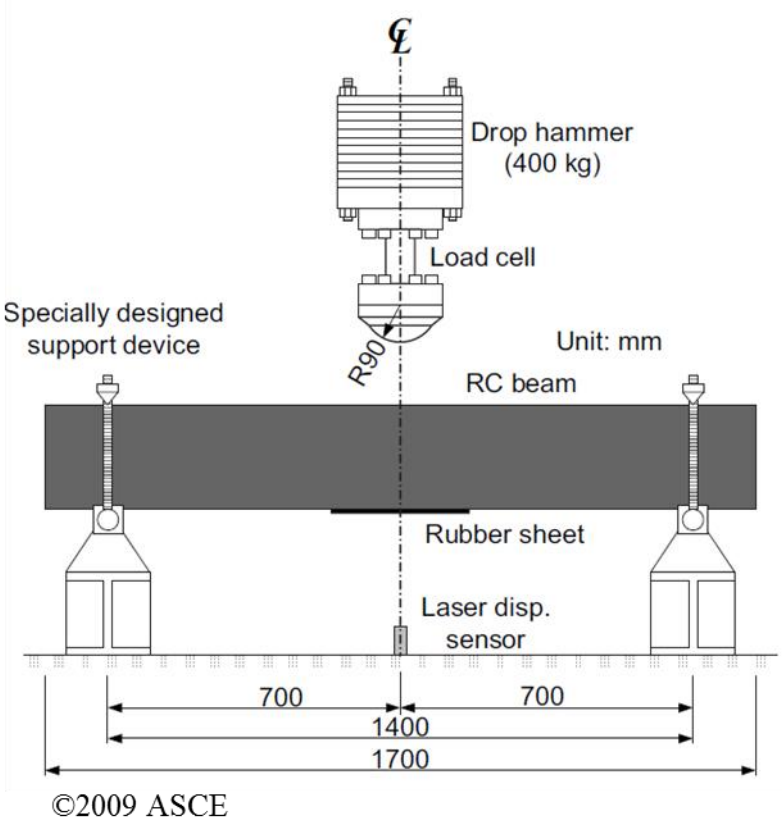

Figure 20. Illustration. RC beam hammer impact test setup.

Four impact test scenarios were simulated in LS-DYNA to calibrate parameters of the CSC model. A unique descriptive name is given to each run for reference. For instance, Gf_0.4_0.1_0.4 implies that parameters Gfs, Gfc, and Gft are 0.4, 0.1, and 0.4 times their default values, respectively. Based on extensive experience with the software, parameters eta0c and eta0t in the user-controlled card are set to be 7 times the default values.

The rebar arrangements and the impact scenarios during the experiment are presented in table 4. The size of longitudinal reinforcements for S1616 and S2222 beams in table 4 are D16 and D22, with yield strengths of 60.6 ksi (418 MPa) and 61.8 ksi (426 MPa), respectively. D10 bars at a spacing of 3 inch (75 mm) and with a yield strength of 42.79 ksi (295 MPa) are used as stirrups. The aggregate used in the concrete has a maximum size of 10 mm, and the concrete compressive strength at the time of testing was 6 ksi (42.0 MPa). The third case in table 4, i.e., S2222 beam with the longitudinal reinforcement of D22 impacted by the dropping hammer from a height of 4 ft (1.2m), was considered first for the purposes of calibration. Figure 21 shows the failure mode observed from experiments. The S2222 beam exhibits overall flexural failure and local failure with heavily crushed concrete near the loading point.

Table 4. Rebar arrangements and impact scenarios.

Designation	Drop height	Compression side		Tension side	
		Number and size (mm)	Area A'_s (mm^2)	Number and size (mm)	Area A_s (mm^2)
S1616	0.6m	2-D16	397	2-D16	397
S1616	1.2m	2-D16	397	2-D16	397
S2222	1.2m	2-D22	774	2-D22	774
S2222	2.4m	2-D22	774	2-D22	774

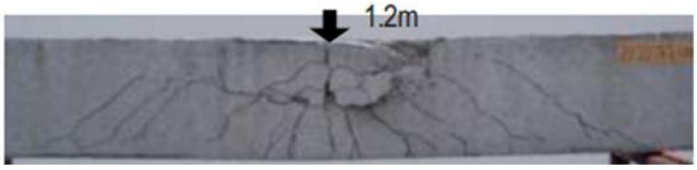

Figure 21. Photo. Damage pattern for S2222 with drop hammer height of 4 ft (1.2 m).

Figure 22 shows the finite element model of the experiment. In this model, concrete components were modeled with eight-nodes solid element of 1 inch (25 mm) size. Steel reinforcements was modeled with beam elements with the same mesh sizes as the solid elements. Perfect bond was considered to model contact between the concrete and steel elements.

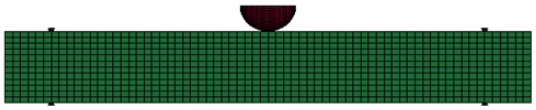

Generated through LS-DYNA

Figure 22. Photo. Finite element model of the drop hammer test.

In order to find the most appropriate material parameters that can accurately capture the dynamic behavior of a concrete beam under impact loading, a parametric study was carried out with different combinations of the parameters Gfs, Gfc and Gft. Damage modes and response quantities of the beam for different combinations of material parameters are plotted in figure 23 to figure 36. Although the default CSCM is simple to use, as shown in figure 23 and figure 24, it underestimates the mid-span deflection by approximately 20%. This shows the necessity of calibrating the default material parameters.

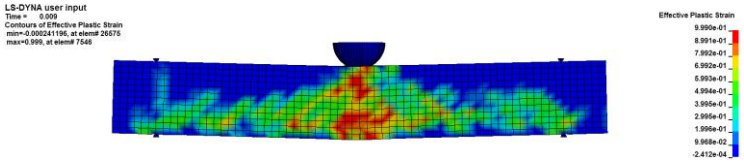

Figure 23. Photo. Damage mode by using default CSCM parameters.

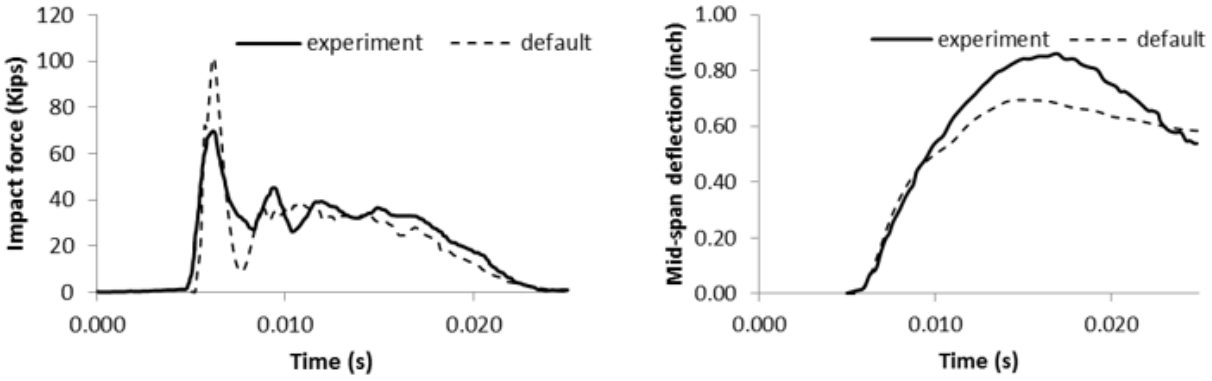

(a) Impact force. (b) Mid-span deflection.

Figure 24. Graphs. Impact response for S2222 beam with 1.2 m drop height using default CSCM parameters.

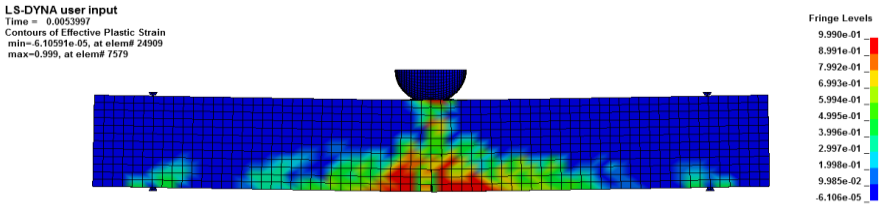

Figure 25. Photo. Damage mode for the case of Gf 0.5_1_1.

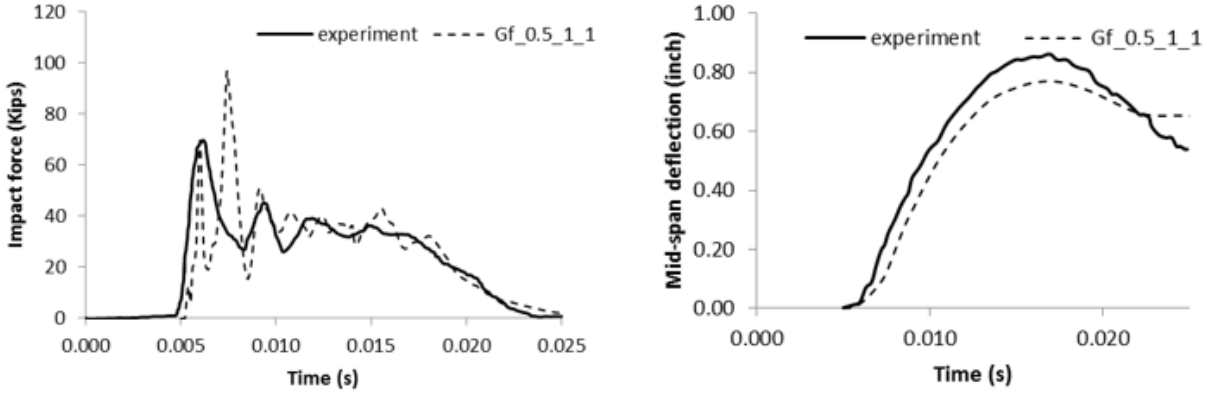

(a) Impact force. (b) Mid-span deflection.

Figure 26. Graphs. Impact response for S2222 with 1.2m drop height for Gf 0.5_1_1.

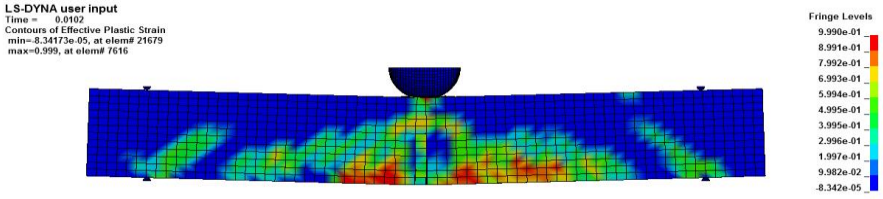

Figure 27. Photo. Damage mode by using Gf 0.5_1_0.5.

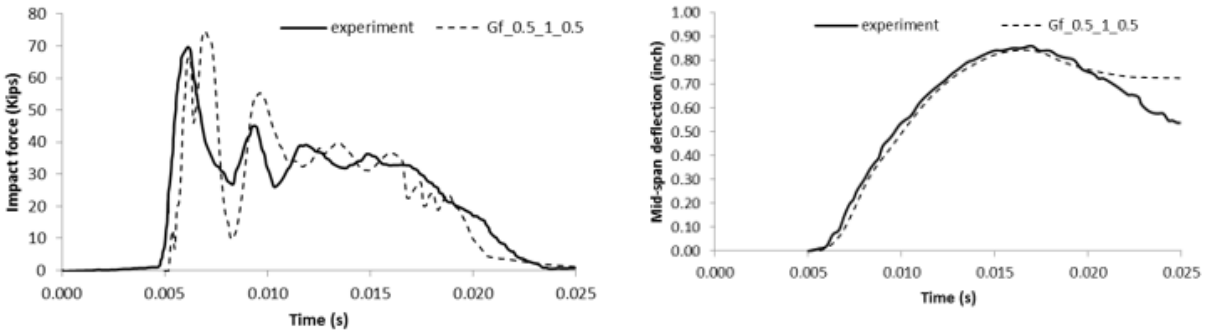

(a) Impact force. (b) Mid-span deflection.

Figure 28. Graphs. Impact response for S2222 with dropping height 1.2 m by using Gf 0.5_1_0.5.

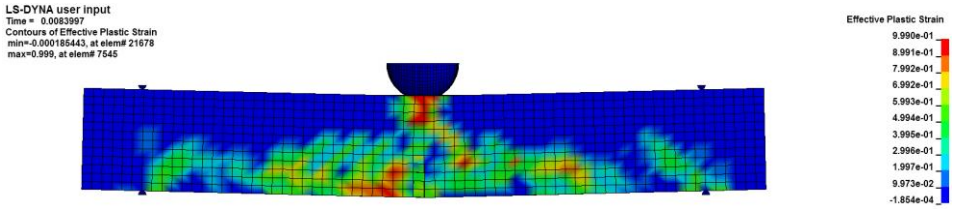

Figure 29. Photo. Damage mode by using Gf 0.5_0.8_0.5.

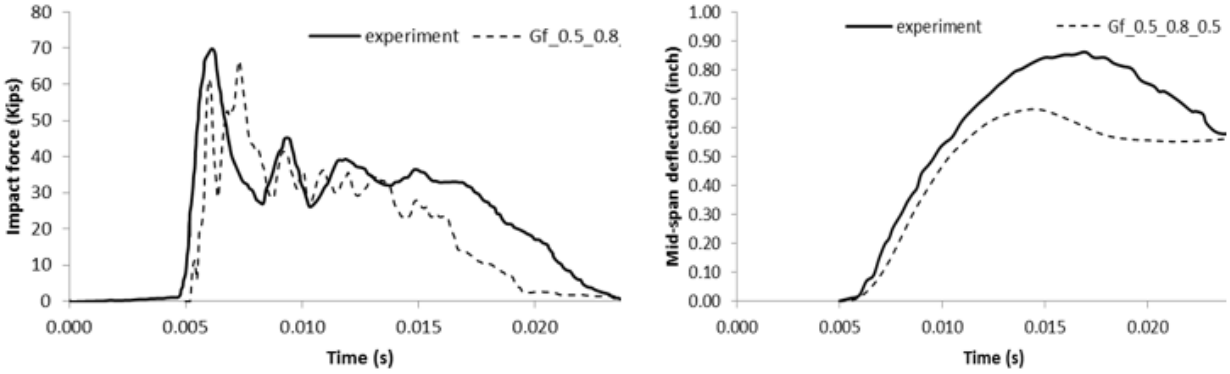

(a) Impact force. (b) Mid-span deflection.

Figure 30. Graphs. Impact response for S2222 with dropping height 1.2 m by using Gf 0.5_0.8_0.5.

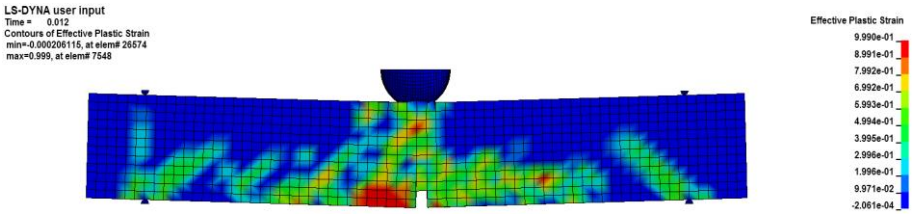

Figure 31. Photo. Damage mode by using Gf 0.5_0.5_0.5.

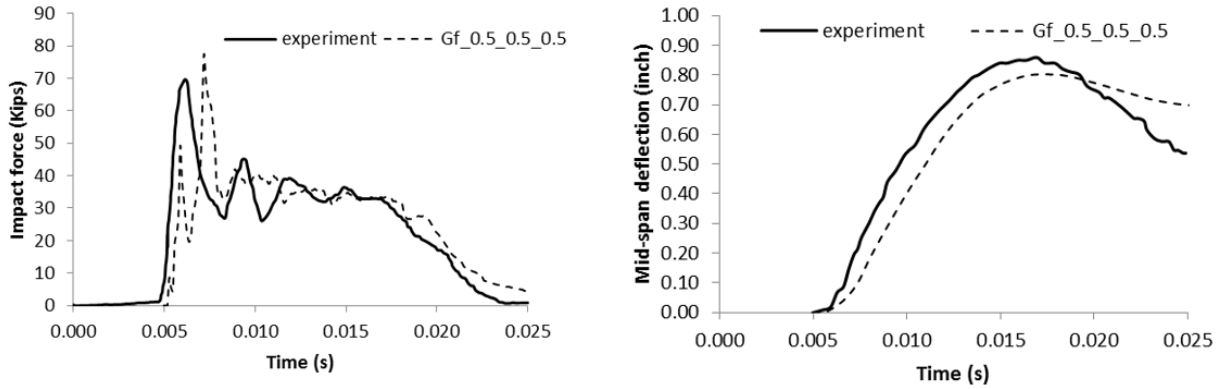

(a) Impact force. (b) Mid-span deflection.

Figure 32. Graphs. Impact response for S2222 with dropping height 1.2 m by using Gf 0.5_0.5_0.5.

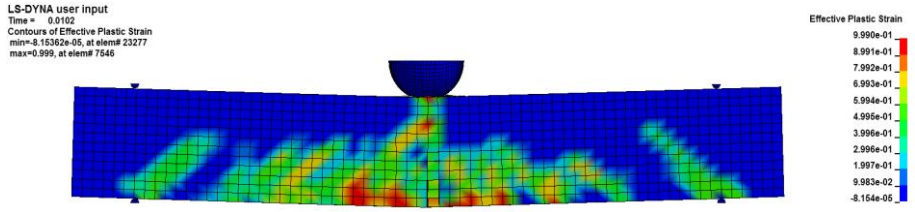

Figure 33. Photo. Damage mode by using Gf 0.4_1_0.5.

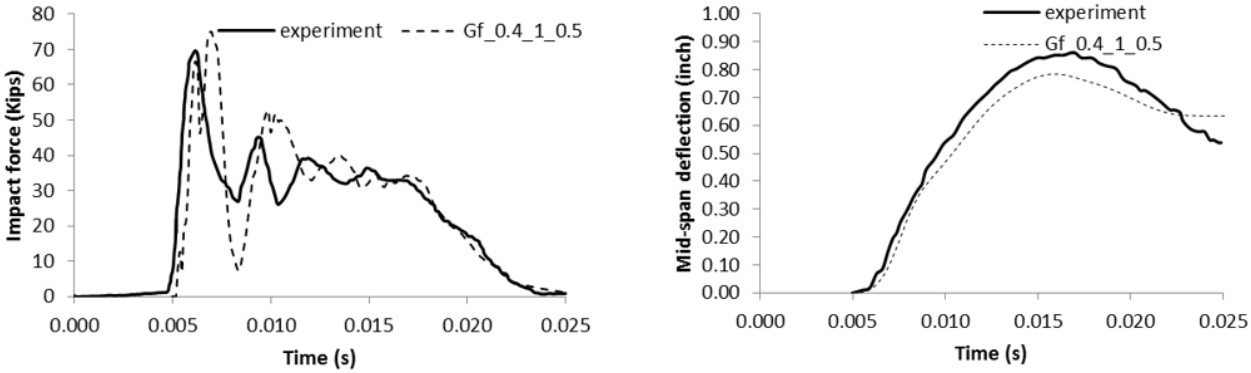

(a) Impact force. (b) Mid-span deflection.

Figure 34. Graph. Impact response for S2222 with dropping height 1.2 m by using Gf 0.4_1_0.5

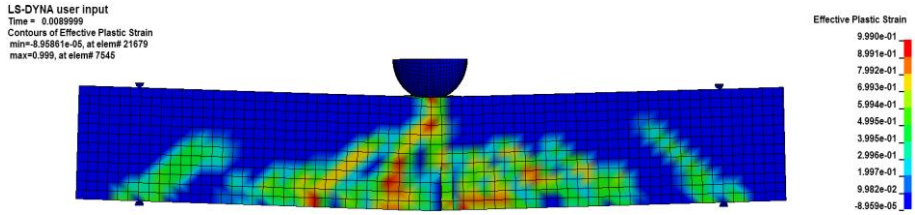

Figure 35. Photo. Damage mode by using Gf 0.4_1_0.4.

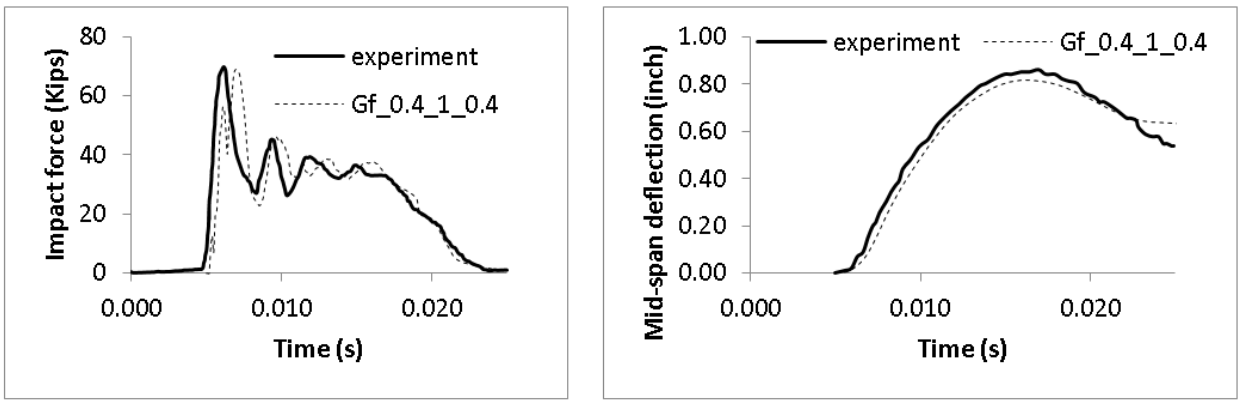

(a) Impact force. (b) Mid-span deflection.

Figure 36. Graphs. Impact response for S2222 with dropping height 1.2 m by using Gf 0.4_1_0.4.

It is clear from the simulation results above that both the mid-span deflection and damage pattern match reasonably well with the experimental data for Gf_0.4_1_0.4 in figure 36. To further demonstrate the appropriateness of these parameters, 3 more impact scenarios (presented in table 4) were carried using Gf_0.4_1_0.4. Results for these cases are shown in figure 37 to figure 42. It is observed from these figures that the differences in peak impact forces are 11.6%, -14.0%, and 30.2%, with a mean of 9.3% for these three cases. The differences in mid-span displacements are -13.3%, 7.4%, and 6.1%, with a mean of 0.1%. These differences are acceptable, given the complexity of the impact process being modeled. Moreover, the damage patterns computed using LS-DYNA match reasonably well with those from the experiments.

The simulation and experimental results exhibited overall flexural failure for the S1616 beam impacted by the drop hammer from 4 ft (1.2 m) and the S2222 beam impacted by the drop hammer from 8 ft (2.4 m). Moreover, the simulations also captured the local crushing of concrete near the load point as observed in the experiments. These results suggest that concrete behavior under impact loading can be modeled realistically using material model Mat_159 with the parameters represented by the case Gf_0.4_1_0.4.

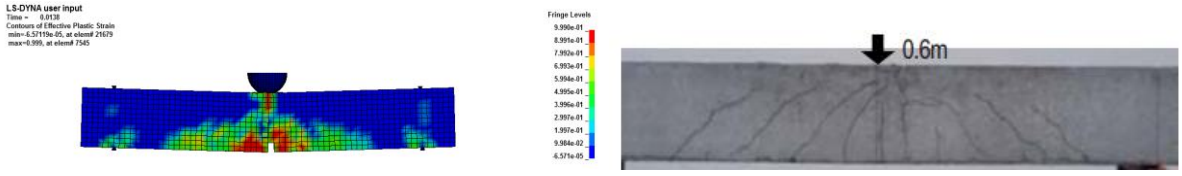

Figure 37. Photos. Damage mode by using Gf 0.4_1_0.4.

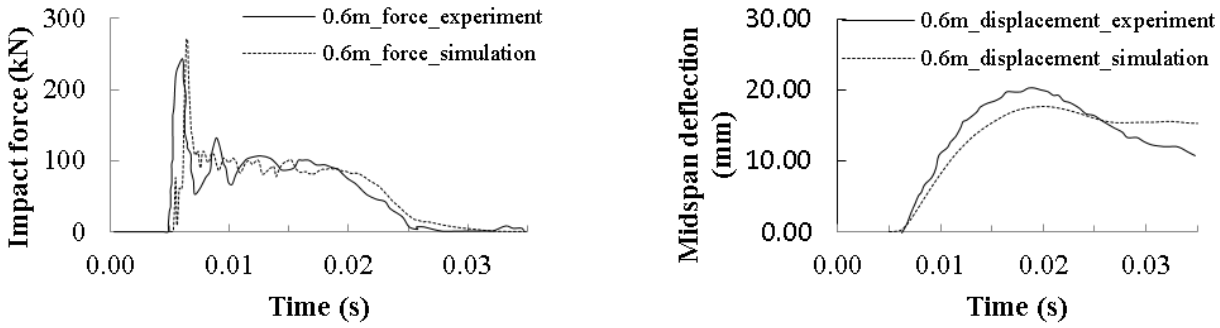

(a) Impact force. (b) Mid-span deflection.

Figure 38. Graphs. Impact response for S1616 with dropping height 0.6 m by using Gf 0.4_1_0.4.

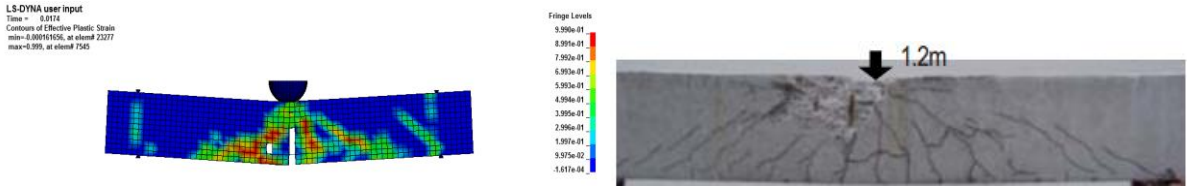

Figure 39. Photos. Damage for Gf 0.4_1_0.4.

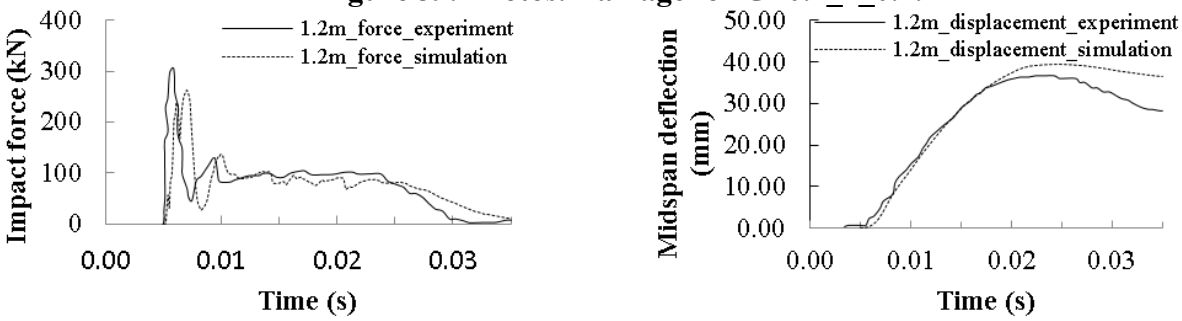

(a) Impact force. (b) Mid-span deflection.

Figure 40. Graphs. Impact response for S1616 with dropping height 1.2 m by using Gf 0.4_1_0.4.

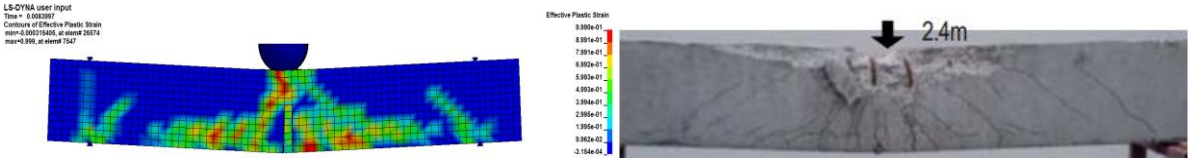

Figure 41. Photos. Damage mode by using Gf 0.4_1_0.4.

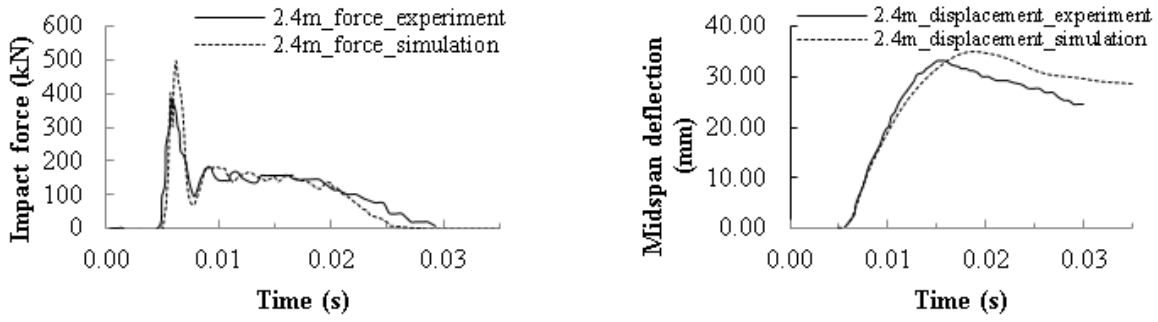

(a) Impact force. (b) Mid-span deflection.

Figure 42. Graphs. Impact response for S2222 with dropping height 2.4 m by using Gf 0.4_1_0.4.

Simulation of Shear Failure by the Calibrated CSC Material Model

Brittle shear failure is frequently observed in bridge piers during vehicular impact accidents. Relatively stiff members tend to attract a greater portion of the impulsive loading to the bridge pier during an impact event and require the generation of large shear forces as the moment capacity of the columns is mobilized. Hence, it is crucial to demonstrate that the calibrated CSCM is capable of simulating shear failure of a bridge pier impacted by a vehicle.

A shear test carried out by Priestley et al. (1994) is used in this research for additional validation. The test setup for this case is shown in figure 43. In this experiment, a 16-in-wide and 24-in-deep rectangular column with 22 No. 6 Grades 60 bars, distributed evenly along the sides of the column was tested. The column has a constant cover of 0.8 in (20 mm). Figure 44 shows the cross-section of the specimen. Transverse reinforcement in the test specimen consisted of No. 2 (6.35-mm-diameter) Grade 40 rectangular hoops at a spacing of 5 in (127 mm).

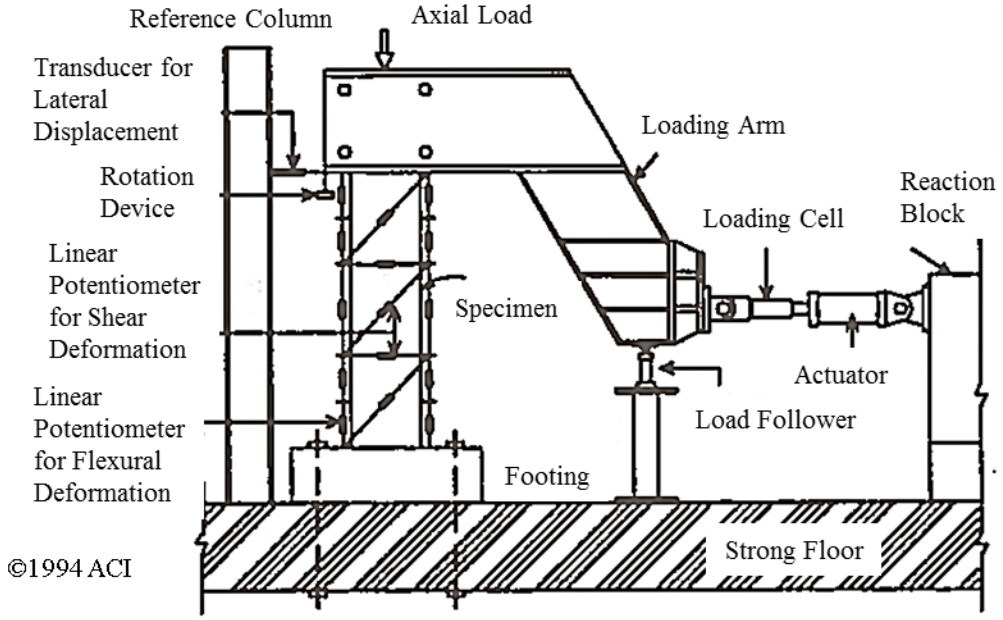

Figure 43. Illustration. Details of shear test setup (Priestley et al. 1994).

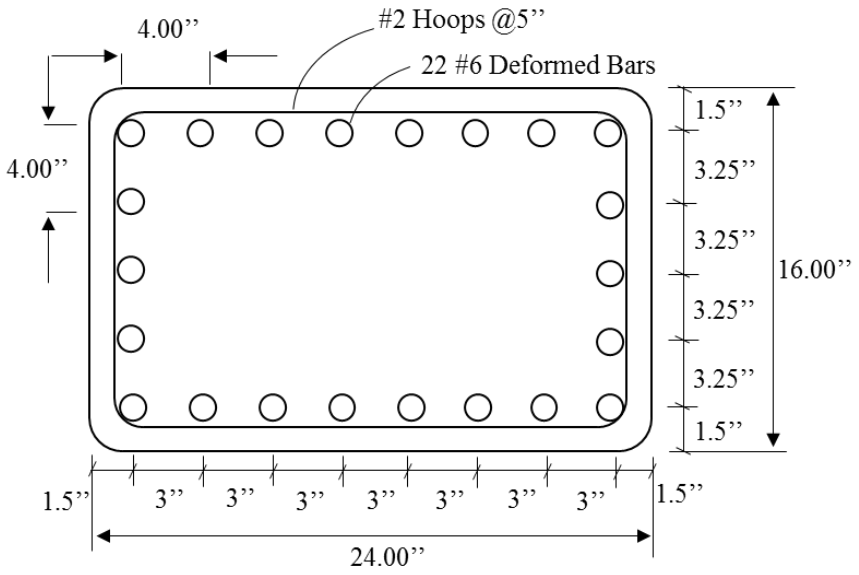

Figure 44. Illustration. Reinforcement details of test rectangular column.

The test column was built using materials and design details appropriate for typical columns designed in the mid-1960s. A target compressive strength of $f_c' = 5{,}000\ psi$ $(34.5\ MPa)$ at 28 days was used to represent the probable overstrength associated with a typical 3,000 psi (20.7 MPa) design strength achieved during the 1960s. A summary of the material strengths for the test column and initial prediction of the column flexural capacity V_{if} is provided in table 5.

Table 5. Test column details.

Test unit	Aspect ratio, $M/_{VD}$	Axial load P, kips	f_c', ksi	Pf_c'/A_g	V_{if}, ksi
R5A	1.5	114	4.7	0.063	213

The test column was subjected to a standard cyclic loading pattern, which consisted of an initial force-controlled stage, followed by displacement control after first yielding of the longitudinal reinforcement. As shown in figure 45, three complete cycles of displacement to displacement ductility factors of $\mu_\Delta = 1, 1.5, 2, 3, 4, 5, 6, 8, and\ 10$ were imposed until column failure occured. The displacement ductility factor μ_Δ is defined as the ratio of the displacement Δ to the yield displacement Δ_y of the column.

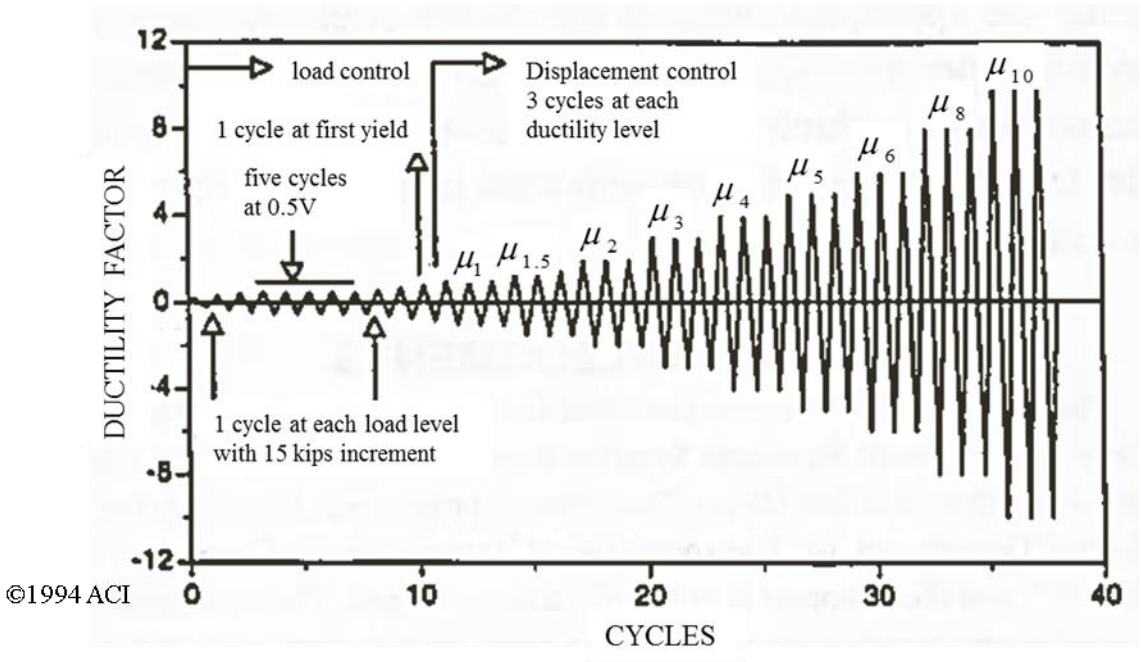

Figure 45. Graph. Static loading history for the shear tests.

It was observed from the experiment that the test column with an aspect ratio of $M/VD = 1.5$ developed brittle shear failure at a displacement ductility factor of less than $\mu_\Delta = 1$. A detailed finite element pushover analysis of column R5A was carried out in LS-DYNA. Figure 46 shows plots of the computed damage patterns at different time sequences. It is observed from simulation results in figure 46 that the test column started developing shear cracks around 0.022s, and the shear cracks increased and extended as the time progressed. This shows that the calibrated CSCM can capture and demonstrate the shear damages in concrete when the piers are subjected to vehicular impacts.

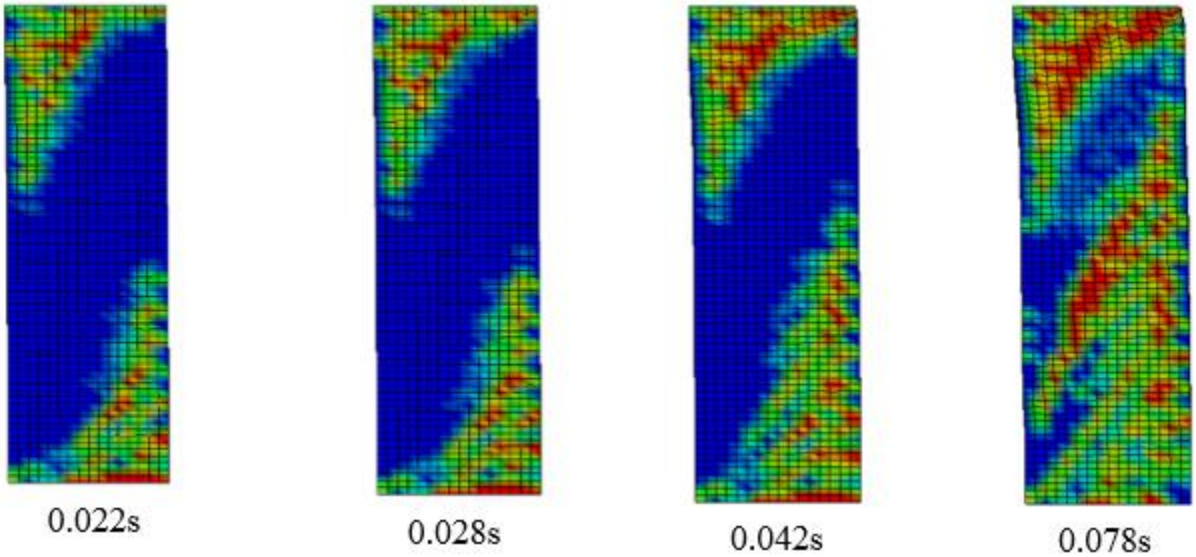

Figure 46. Photos. Column damage levels.

CHAPTER 3. LARGE SCALE TESTING AND SIMULATION

INTRODUCTION

Vehicular impacts on concrete bridge piers is a complex and fast dynamic process, which is usually accompanied by high strain rate loading. Shkolnikov (2004) investigated strain rates based on data recorded by testing machines with velocities up to 3.7 mph. The strain rates were measured up to 850 s^{-1} in the beginning and end of the loading; it was measured to be 50 s^{-1} during the loading. Grote et al. (2001) carried out experimental characterization of strain rate effects of concrete in the strain-rate range of 10^{-3} to 1700 s^{-1}. They found weaker rate dependency for strain rates below 400 s^{-1} and significantly stronger dependency above this rate. Their work also shows that the shapes of the stress-strain curves at different rates are similar to each other. Depending on the speed of impact, strain rate during vehicular impacts on bridge piers may be significant and must therefore be accounted for properly.

Typical impact tests for reinforced concrete members are carried out by dropping a weight onto a specimen. For example, data from impact tests by Fujikake et al. (2009) were used in chapter 2 to calibrate the parameters of the concrete material model. These tests are typically carried out on small concrete members, e.g., beams and cylinders. Other representative dropping weight tests available in literature are Kishi et al. (2001, 2002), Krauthammer et al. (2003), Remennikov and Kaewunruen (2007), Lifshitz et al. (1995), Zineddin and Krauthammer (2007), and Adhikary, Li, and Fujikake (2012).

Although dropping weight tests can be utilized to calibrate material model of concrete, these tests cannot be used to characterize and validate damage mechanism in large scale bridge piers impacted by trucks. Drop hammers used in dropping weight tests are usually rigid, whereas trucks impacting bridge piers get deformed severely during crashes, leading to significant dissipation of energy. Dropping weight tests are also limited to individual components and don't include interaction of the entire structural system during impacts on bridges.

Carrying out full-scale tests on bridge components is cost-prohibitive and poses numerous logistical challenges. Although full-scale tests were carried out by Buth et al. (2011) to develop guidance on the design of bridge piers vulnerable to vehicular impacts, the pier model in their test was rigid, which doesn't represent concrete bridge piers impacted by trucks.

Liu (2012) and Xu (2017) investigated the impact of single unit trucks on bridge piers. In particular, Liu (2012) investigated the effect of truck impact on piers of a three span bridge by using a computational model of the full bridge and a three-column bent structure representing the portion of the bridge directly affected by the impact. His results showed that the three-column bent model is sufficient for simulating the impact of trucks on the bridge pier. Hence, either a full-scale or scaled model of three-column bent structure can be used for impact testing to adequately investigate the effects of vehicle impact on the bridge system.

With the objective of additionally validating the capability of the computational model outlined in chapter 2 for simulating damage modes and high strain rate effects during vehicular impacts on bridges, a large scale impact test was carried out on a three-column bent model. In this test, a

pier bent model was impacted by a pendulum that could be swung from a predetermined height. Figure 47(a) shows conceptual sketch of the concrete model considered for testing. The red arrow in this figure shows the direction of impact by a pendulum. The full-scale testing was done at the Federal Outdoor Laboratory of the Federal Highway Administration in Mclean, VA, using the outdoor pendulum impact system shown in figure 47(b).

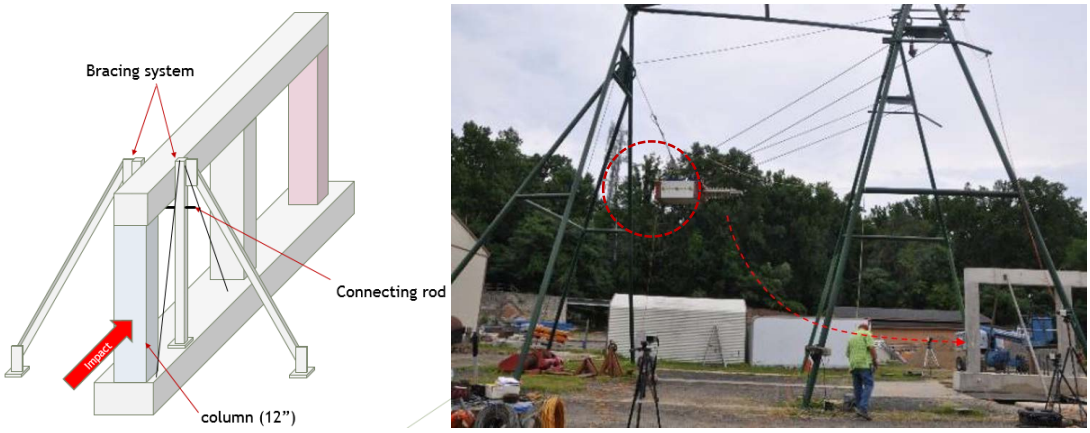

(a) Column-bent model setup for testing. (b) Outdoor pendulum impact system.

Figure 47. Sketch and photo. Conceptual model of the column-bent structure for testing and pendulum test frame system.

DESIGN OF THE TEST MODEL

The large-scale three-column bent structure constructed for testing was based on an existing bridge built in 1956 in New York State. Figure 48 shows plan and elevation views of this bridge. Yi et al. (2013a, b) investigated the effects of blast loads on this bridge. Liu (2012) and Agrawal et al. (2013) investigated impact of a single unit truck on piers of this bridge. Figure 49(a) shows a computational model of the piers of the bridge that were impacted by a single unit truck. Liu (2012) also proposed a modified three-column bent model, shown in figure 49(b), for the simulation of vehicular impact.

The large scale three-column bent structure was generally a half scale model of the prototype bridge in figure 49. However, the scaling factor for the cross-section of the piers was 1/3rd so that damage could be induced by the pendulum type impactor. Figure 50 shows reinforcement details of the pier-bent model. Section size and height of each of the piers are 12x12 in and 96 in (8 ft), respectively. The two end piers of the three-column bent were designed such that one of the end piers behaved as a strong pier whereas the other pier behaved as a weak pier. The two end piers were designed differently so that two impacts tests could be carried out. After the weak pier was impacted by the pendulum, the model was rotated 180º horizontally so that the strong pier could be impacted.

Reinforcements in the two piers were designed through computational simulation so that the weak pier suffered moderate damage whereas the strong pier suffered mild damage. This was achieved by using Grade 60 eight #4 steel rebars in the weak pier and Grade 60 eight #6 steel rebars in the strong pier. Foundation and top beams and middle pier of the model were designed

not to suffer any damage during the testing. The thickness of the cover concrete in the model was approximately 1.5 in. Total estimated weight of the model was 19.2 kips.

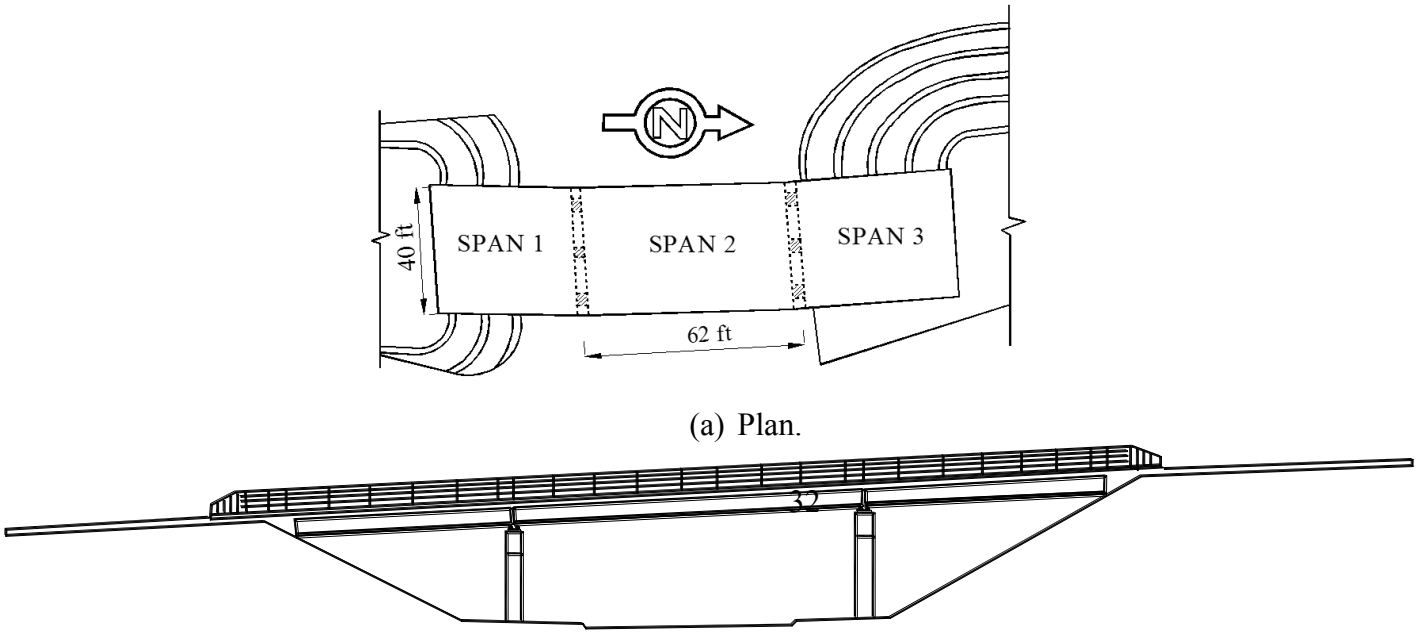

(a) Plan.

(b) Elevation.

Figure 48. Sketch. Plan and elevation of the prototype bridge.

(a) Impacted piers of the bridge. (b) Pier-bent model for vehicular impacts.

Figure 49. Sketch. Prototype model of the bridge for large scale testing.

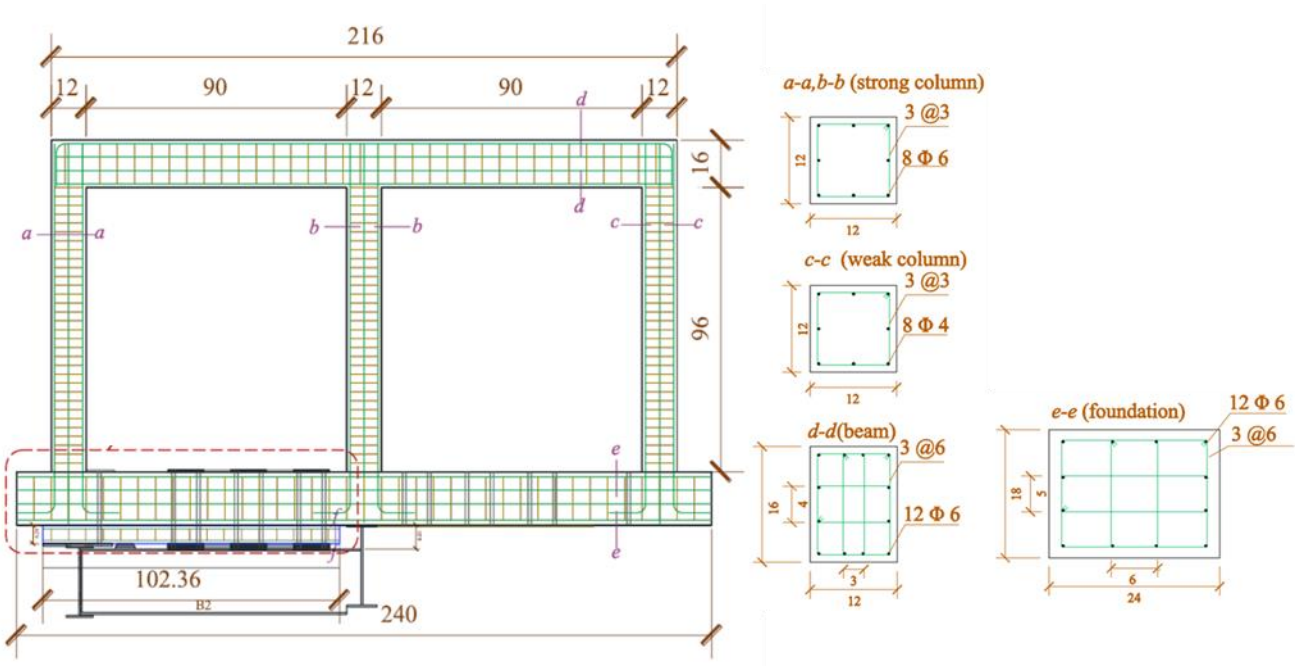

Figure 50. Sketch. Reinforcement details of the bent (inch).

DESIGN OF THE IMPACTOR

The heaviest impactor available at the FOIL facility weighed 4,338 lb and was developed by Marzougui et al. (2013) to approximate the weight of a pickup truck for testing roadside hardware. Figure 51(a) shows the impactor of the pendulum. It consisted of a reinforced concrete block with steel end-plates on the front and rear surfaces. Concrete was used to minimize vibratory "ringing" in the accelerometers mounted on the rear end-plate. A crushable front surface, designated as "nose", consisting of collapsible honeycomb aluminum cartridges was mounted on the front plate. These cartridges were designed to approximate the crush of a pickup truck when colliding into a rigid pole at 20 mph speed (Marzougui et al. 2013).

During the testing, the impactor was hoisted to a pre-determined height and then was released to swing like a pendulum to impact the pier-bent model at the lowest point of the trajectory, which is indicated by broken red arrows in figure 47(b). Following the principal of conservation of energy, the velocity of the impactor at the point of impact, after dropping through a height of h, is given by,

$$V = \sqrt{2gh} \tag{6}$$

where g is the acceleration of gravity with a value of 32.2 ft/s^2 and h is the hoisted height of the pendulum from the impact point.

Figure 52 shows various views of the pendulum. As shown in figure 51(a), the pendulum nose was connected to the body of the impactor on a sliding sleeve system. The space between the nose and the front plate of the impactor was divided into many compartments where aluminum honeycombs were installed. Type and strength of honeycombs in figure 51(a) were designed by

Marzougui et al. (2013) to simulate actual tests on MASH1100C vehicles, such as 2006 Kia Rio, on a rigid pole.

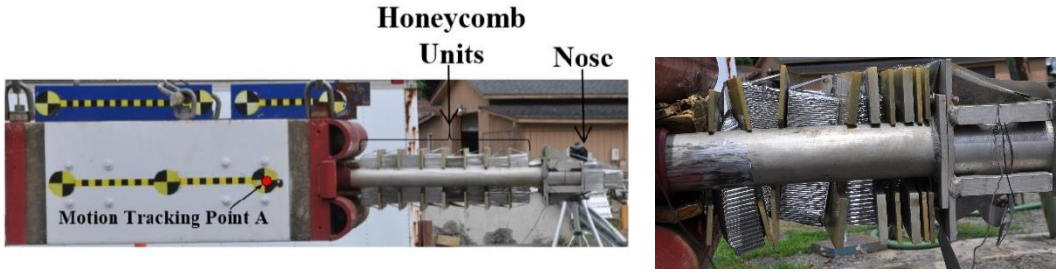

(a) Pendulum impactor before test. (b) Nose of the impactor after test.

Figure 51. Photos. Pendulum impactor before and after test.

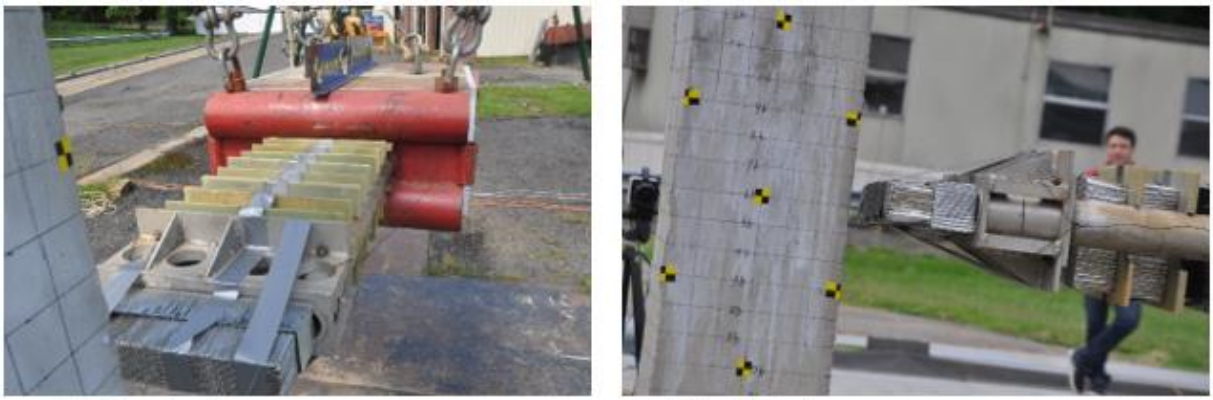

(a) Front view. (b) Side view.

Figure 52. Photos. Various views of the pendulum.

Figure 51(b) shows the nose of the impactor after the test. It is observed that the honeycomb units on the nose tip were crushed first. As the nose slid on the sleeve system towards the main body of the impactor, it crushed additional honeycomb units. Impact demands because of vehicular impacts can be emulated during large scale tests by carefully selecting the type of honeycomb units and arranging them in a specific sequence. The design of honeycombs for the MASH 1100C test was conducted by Marzougui et al. (2013). For example, figure 53 shows a very good agreement in the behavior of the pendulum after the test and a LS-DYNA simulation for 20 mph speed when pendulum weight was 2,420 lb.

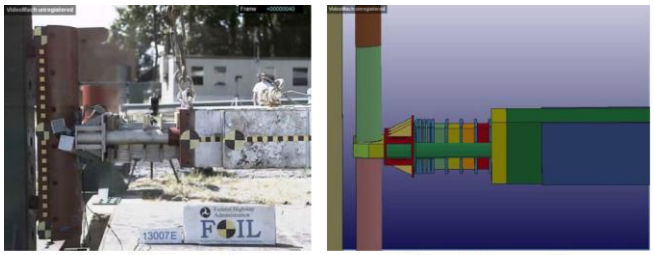

(a) Test. (b) Simulation.

Figure 53. Photos. Behavior of pendulum nose during testing by Marzougui et al. (2013).

In order to investigate the capability of the pendulum for representing vehicular impacts on concrete piers, impact demands due to vehicular impact were generated by impacting a 1995 F800 truck model shown in figure 54 against the pier-bent model at different speeds. The F800 truck has been used by others to investigate the effects of truck collision with bridge piers (Agrawal et al. 2013, Chen et al. 2016a, Chen et al. 2016b, Liu, 2012). Figure 54(b) shows a pretest comparison between the simulated force demand imposed by the impactor and that by a 1995 F800 truck approaching at a speed of 30 mph. The truck's speed was selected such that the scaled kinetic energy of the truck matched that of the impactor. The truck's nominal weight was 8 metric tons, which was scaled down to 1 metric ton at half scale. The impactor's weight was approximately 2 metric tons and could achieve a speed of approximately 20 mph at the instant of impact. Figure 54(b) shows that the computed impact force time histories matched reasonably well, including the sharp spike at 62 ms, which corresponded to the engine block impacting the pier in the truck model.

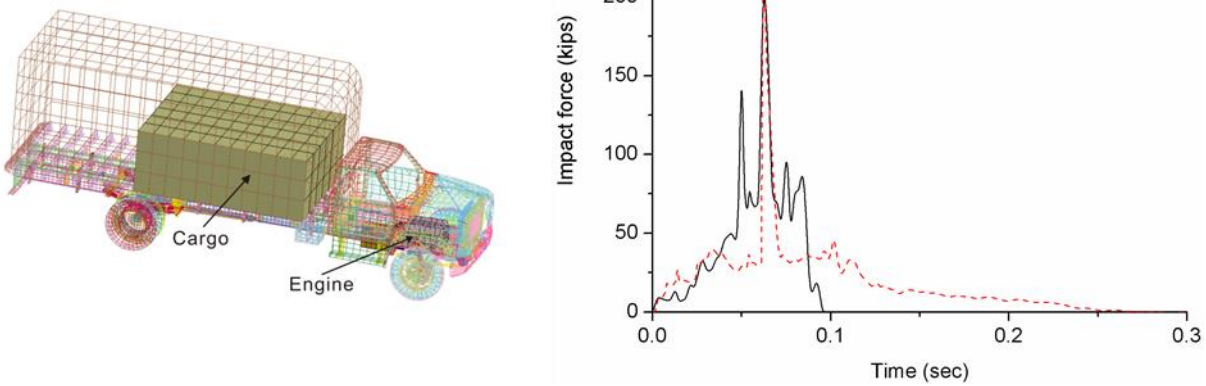

(a) Ford F800 truck model. (b) Computed force time histories.

Figure 54. Illustration. Generation of impact force time history of the impactor.

TEST SETUP

The large scale concrete model was built onsite at the FHWA FOIL site and was moved over the test pit for impact testing, as shown in figure 55. The test pit has a foundation system consisting of a strong steel frame attached to a concrete substructure. In order to attach the pier-bent

model to the foundation system, a 2 ½ inch thick steel plate was welded on top of this foundation frame system. However, since the top of this steel plate was 20 inches below the ground level, a concrete pedestal with predetermined pattern of holes was placed on top of the steel plate, which also had the same pattern of holes. Figure 55 shows the top of the pedestal with predetermined pattern of holes. During the casting of the pier-bent model, a template of the holes was fabricated and placed below the pier-bent model. The pattern and size of holes in the bottom beam of the pier-bent model were secured during the cast of concrete by 2-inch diameter PVC pipes.

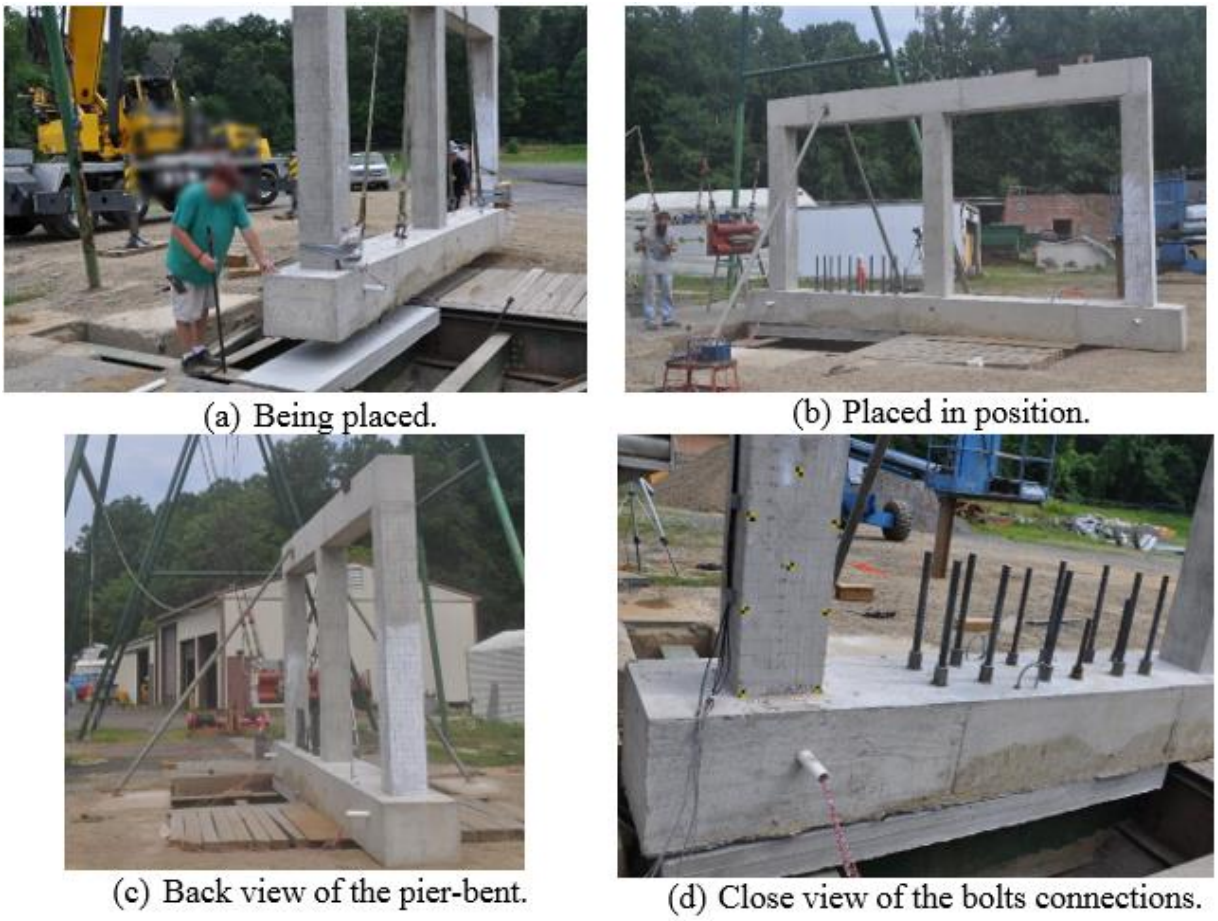

Figure 55. Photo. Pier-bent model being placed over the test pit and attached to foundation system.

The pier-bent model was connected to the foundation system through a number of bolts as shown in figure 55(b). The size of the foundation steel frame was long enough to support only one bay of the two-bay model. The other bay extended beyond the steel frame onto ground, as shown in figure 55(b). Portion of the model over the steel foundation system was carefully aligned with 12 bolt holes in the pedestal and the steel plate and connected to the foundation system through high strength bolts. These bolt holes in the steel plates, foundation beam of the model and the concrete pedestal were made 1 inch (25 mm) larger than the diameter of the bolts to address any concern about misalignment of holes during casting of the concrete. The bolts were tightened sufficiently to ensure friction between the model and the foundation system so that the model

could transfer impact forces to the foundation. The final setup of the test is shown in figure 56. The model was braced in the out of plane direction at the top beam, close to the point where the pier was impacted, to avoid any out of plane movement or instability. Two braces, one on either side of the frame, were used to connect the top beam to the foundation concrete block.

Figure 56. Photo. Setup of field test.

Instrumentation

A laser measurement device placed on the ground under the impactor was used to determine its height. Based on the height achieved in the test, the velocity of the impactor at impact was calculated to be 18 mph. Four high-resolution, high-speed digital cameras with frame rate of 500 frames per second and a resolution of 1280x1024, three standard-resolution, high-speed digital cameras, a digital camcorder, and a digital still camera were used to film the tests. The high-speed digital cameras were positioned to record overhead, left, right, rear and isometric views of the crash event.

Location markers were placed along the height of each pier at intervals of 12 inch. The displacement of these markers was tracked via special image processing software applied to the high speed camera views. Other markers were placed on the foundation beam and the top beam. Strain gauges were installed on the bar reinforcement at multiple locations. The surface of the bars was ground to ensure good contact with the gauges and a layer of waterproof coating was applied around the gauges before concrete pouring to protect them. Figure 57 shows the locations of key strain gauges. Strain gauge data was processed using a SAE-180 filter with a frequency of 300 Hz.

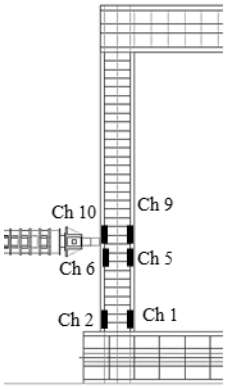

(a) Longitudinal bars for strong pier.

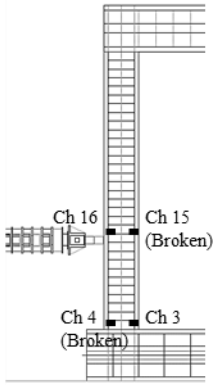

(b) Stirrups for strong pier.

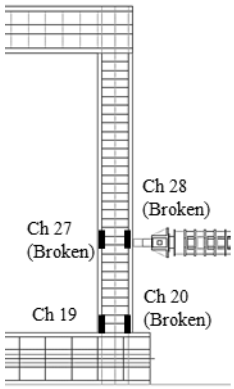

(c) Longitudinal bars for weak pier.

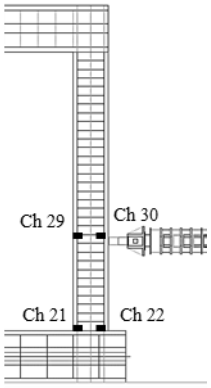

(d) Stirrups for weak pier.

Figure 57. Sketch. Strain gauges on the pier.

Material Properties for Concrete and Rebars

Twenty four concrete test cylinders, each of 10 cm in diameter and 20 cm in height, were made out of concrete used for the pier bent structure. The cylinders were divided into three groups that were used to obtain the compressive strength, elastic modulus and Poisson's ratio at three ages (7, 14 and 28 days) according to ASTM specifications. Table 6 shows compressive test results for cylinders. Reinforcing bar coupons (in sets of three) for the #3 and #4 bars were tested only up to 1.5% strain because higher strain levels were not expected during the test. The stress versus strain plots for these rebars are shown in figure 58. Yield strengths of these rebars are listed in table 6. Coupons from the #6 bars were not tested because their yield strength exceeded the capacity of the test machine, but their yield strength is estimated as shown in table 6 and their stress-versus-strain behavior is assumed to mirror that for the #4 bars.

Table 6. Properties of reinforcing steel and concrete.

Material		Experiment items	Measured values
Longitudinal reinforcement	#3	Yield strength, ksi	74.0
	#4	Yield strength, ksi	71.1
	#6	Yield strength, ksi	72.5
Concrete		Compression strength, ksi	5.4
		Elastic modulus, ksi	4,485.0
		Poisson's ratio	0.2

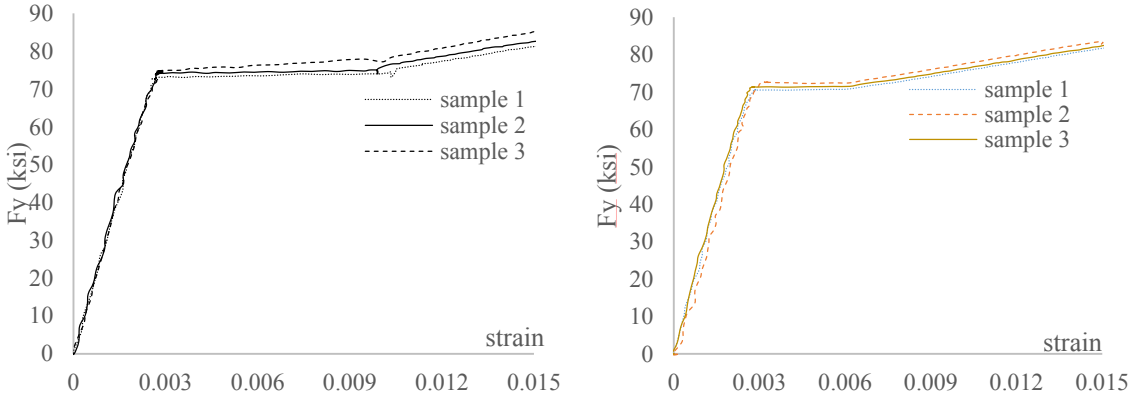

(a) #3 rebar. (b) #4 rebar.

Figure 58. Graphs. Steel rebar stress-strain relationship for rebar.

TEST RESULTS

Main objectives of the large-scale pier-bent test were (i) to demonstrate the capability and reliability of the computational modeling scheme in simulating vehicular impacts on bridge piers, (ii) to demonstrate the similarity of damage modes and crack patterns between the test and actual accidents of vehicular impacts on bridge piers and (iii) to calibrate the simulation models of the piers in the computational model, particularly the element size and parameters of the material model. As discussed in chapter 2, parameters of the concrete material model were calibrated based on test data from Fujikake et al. (2009). One of the objectives of the test was to demonstrate that these calibrated parameters could be used to show an agreement between test and simulation results.

Crack Development

Figure 59 shows permanent crack formation on all sides of the weak pier during impact by the pendulum. These cracks tended to concentrate at the impact points and at upper and lower ends of the pier. This behavior of damage has also been observed during actual impacts on bridge piers, where plastic hinges were seen to form at the impact point and at the bottom and top of the pier. It was observed that the main crack, with a width of 0.39 in (10 mm), penetrated through the entire section width. Figure 60 shows crack growth with time at the impact location. All the cracks were observed to be flexural.

The pattern of cracks during the impact on the strong pier was generally the same as that for the weak pier, as observed from figure 61. The main difference in the test results for these two piers was that the crack widths in case of the strong pier test were much lesser, with a maximum crack width of 0.12 in (3 mm), less than those in case of the weak pier.

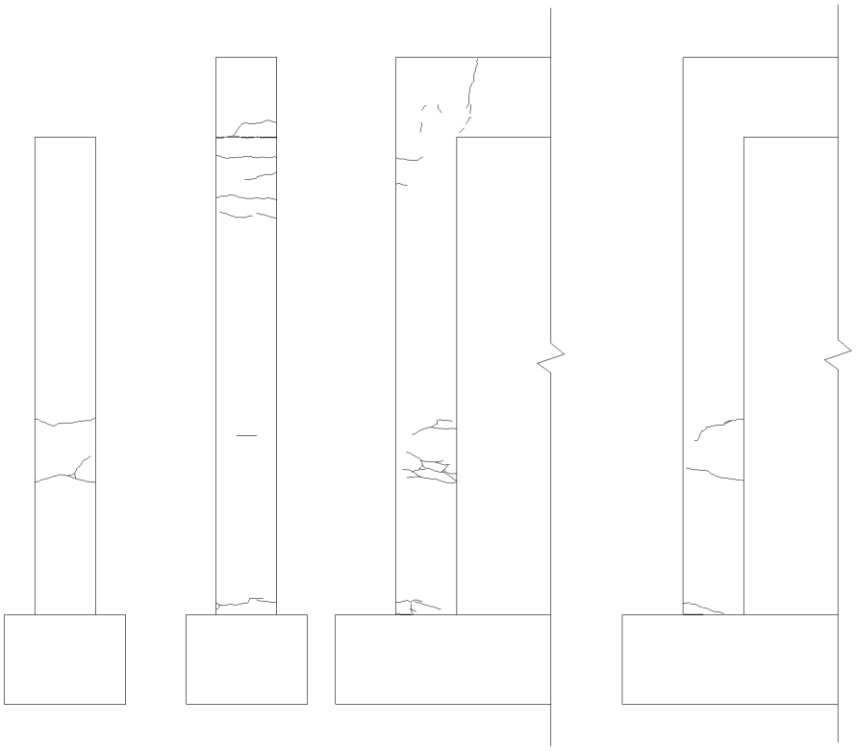

(a) Inner. (b) Outer. (c) Front. (d) Back.

Figure 59. Sketches. Permanent crack pattern of the weak pier four sides' displays.

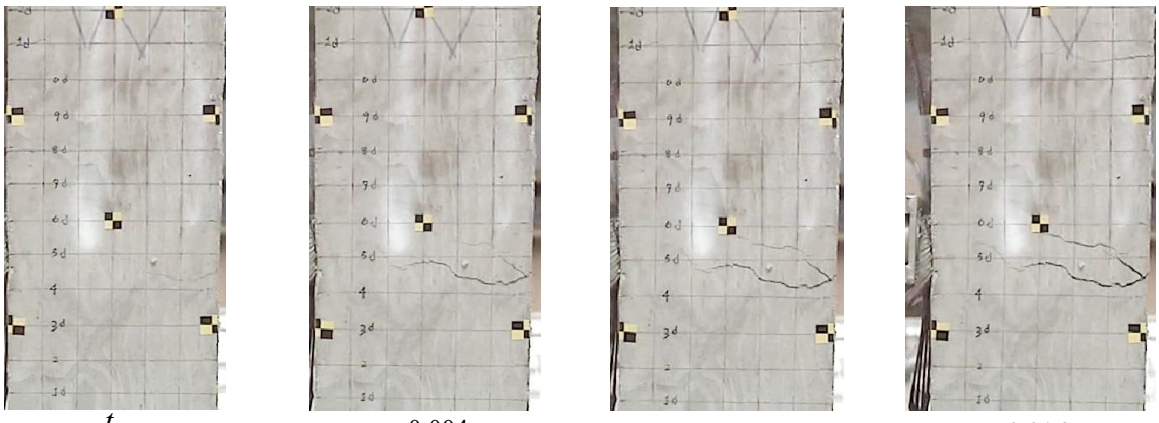

t *t*+0.004s *t*+0.010s *t*+0.016s

Figure 60. Photo. Crack evolution for the weak pier impact.

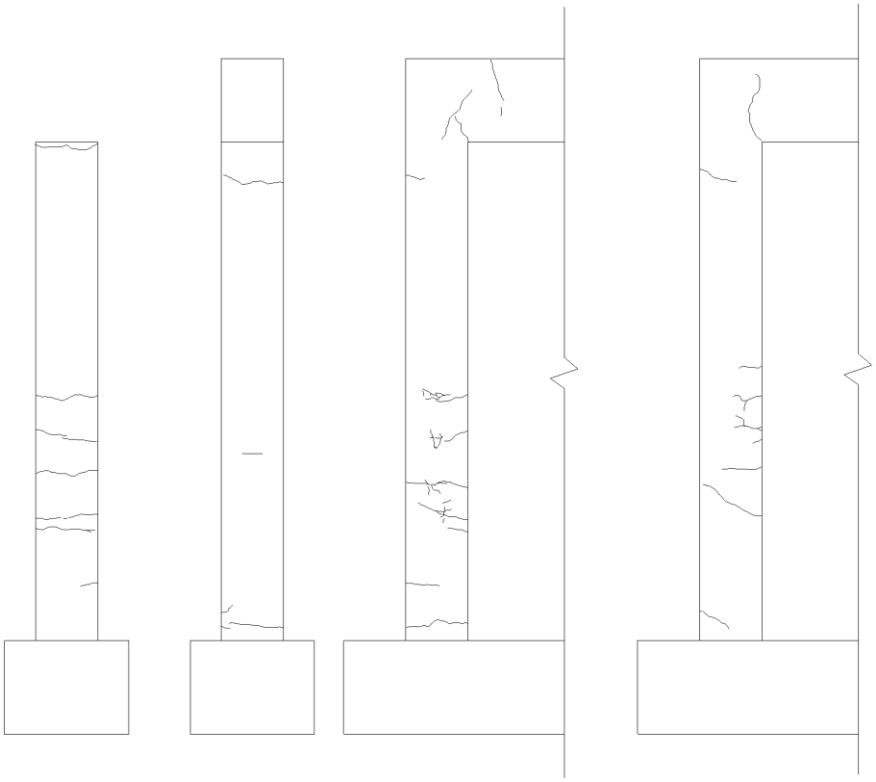

(a) Inner. (b) Outer. (c) Front. (d) Back.

Figure 61. Sketches. Permanent crack pattern of the strong pier four sides' displays.

VERIFICATION OF THE TEST THROUGH FINITE ELEMENT MODEL

The pier-bent structure was modeled using finite elements, as shown in figure 62, in LS-DYNA (Hallquist 2006). As done in chapter 2, concrete is modeled using reduced integration, eight-node, and brick elements whereas steel bar reinforcement is modeled using Hughes-Liu beam elements. Full bond is assumed between both concrete and steel elements. The original pre-simulation model was calibrated for elements that are 1.5 inch (38 mm) in size. This same size is maintained in this model to void mesh size dependency effects. Mild damping is introduced with a global damping factor of 6. To avoid the uncertainties associated with modeling the steel foundation frame and its interactions with the concrete substructure and ground underneath, the recorded motion of key points on the foundation beam was assigned as a prescribed motion to the nodes of the foundation beam in the model.

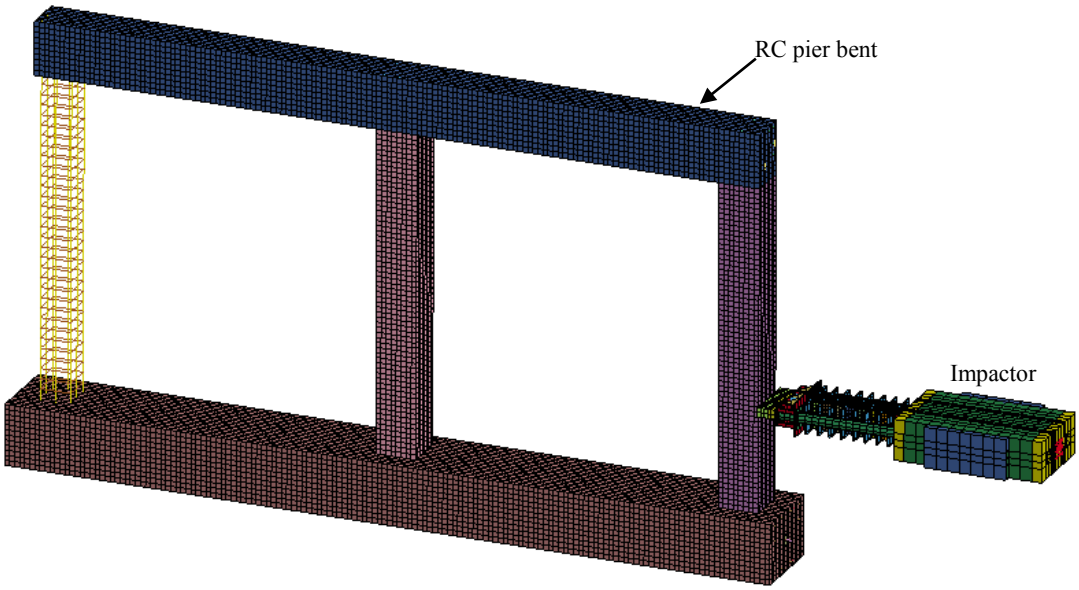

Figure 62. Illustration. Finite element model with mesh size 1.5 inch (38 mm).

Material model 159 was selected to model concrete behavior. The parameters for this material model were modified through calibration of the material model parameters to published test data in Abu-Odeh (2008) and Fujikake et al. (2009). Details of the calibration process and the actual calibration parameters can be found in chapter 2. Material model 3 was selected for modeling steel bar behavior which accounts for yielding and kinematic hardening plasticity. Rate effects are accounted for by using a Cowper-Symonds relationship, where the model parameters are taken as C=40s^{-1} and p=5, respectively. The measured material properties have been assigned to both concrete and steel models.

The impactor, consisting of the crushable components, slider and mass blocks, is modeled as shown in figure 63. Both the mass blocks and the various honeycomb parts in the impactor nose are modeled using reduced integration, eight-node, brick elements. Material properties of honeycombs are assigned using Material model 26 according to Marzougui et al. (2013).

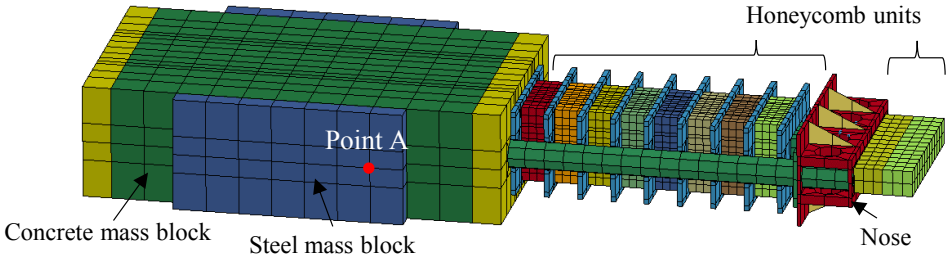

Figure 63. Illustration. Computational model of pendulum impactor.

EXPERIMENTAL VS. COMPUTATIONAL RESULTS

Impactor Crash Process

Figure 64 compares the impactor's computed versus observed behaviors. Clearly, the process was simulated well, at least from visual and qualitative points of view. Figure 65 shows a quantitative comparison of the simulated and "measured" force delivered by the impactor and its velocity. The "measured" force was computed from the accelerometer attached at the tail of the pendulum, which measures acceleration time history in the X (longitudinal, i.e., along the axial of the bent) and Z (vertical) directions. The accelerometer data was processed with an SAE filter with a 100 Hz frequency and multiplied by the impactor's mass to compute the applied force as shown in figure 65(a). The discrepancy between the force computed from the simulation model and "measured" force is due to the inertial effects being ignored as noted in Banthia et al (1987). Figure 65(b) shows the velocity time histories. The velocity time history from the test was obtained by integrating the acceleration data. The comparison is clearly good even up to the negative bounce back effect that occurs after impact at about 100 ms.

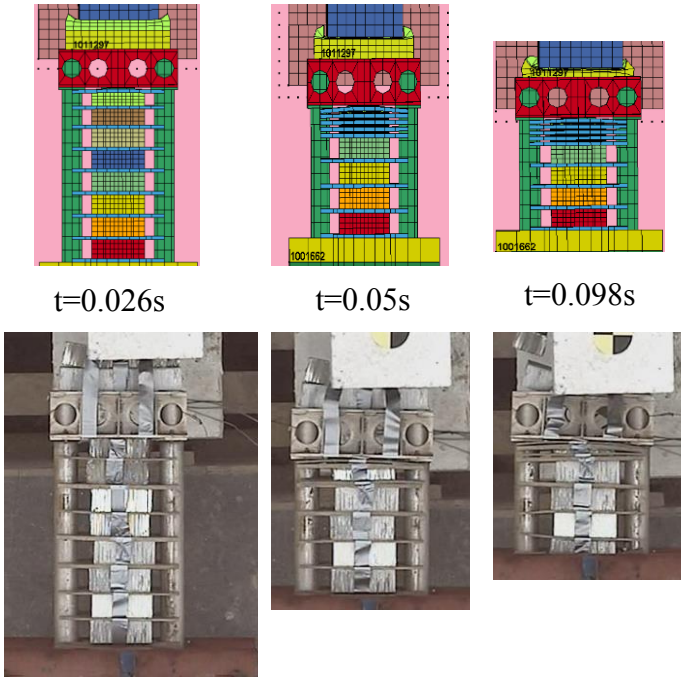

Figure 64. Photos. Pendulum nose crash process.

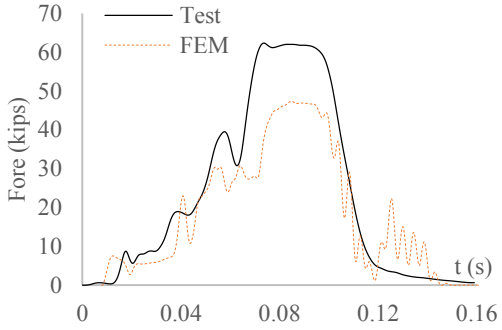

(a) Pendulum induced impact force time history derived from acceleration.

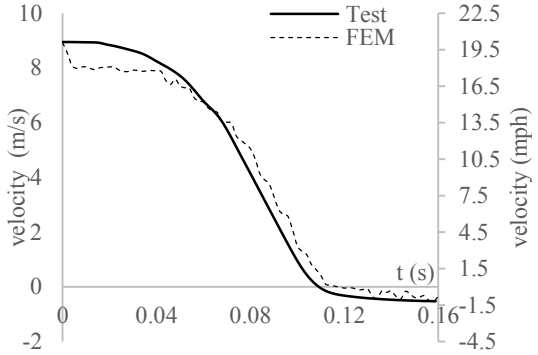

(b) Velocity integrated from the acceleration of point A.

Figure 65. Graphs. Test result of impact force and velocity of point A (see figure 63).

Displacement Time History

Figure 66 (a) shows a comparison between the computed and measured displacement time histories of 3 nodes for the weak pier. Node 1 is near the bottom of the pier, almost at the foundation beam, while node 3 is close to the top beam. Node 2 is located at the impact height. The three solid lines represent the test results while the dashed lines are for the corresponding finite element (FE) results.

The results for node 1 match very closely because the foundation beam displacement history is prescribed and node 1 is close to the foundation beam. The comparison between the computed and measured displacements of the two other nodes is a measure of the validity of the modeling scheme. Clearly, both match well in terms of initial growth and peak values. For example, the measured peak displacement for node 2 is 1.36 inch (34.6 mm) and the computed one is 1.41 inch (35.7 mm), i.e., it is 3% off. The measured peak displacement for node 3 is 1.79 in (45.5mm) and the computed one is 1.62 inch (41.1 mm), i.e., it is 10% off.

Figure 66 (b) shows a similar comparison for the strong pier. As expected, the results for node 1 match well. The comparisons for node 2 appear as accurate as seen in the test for the weak pier. For example, the measured peak displacement for node 2 is 1.42 inch (36.0 mm) and the computed one is 1.33 inch (33.8 mm), i.e., it is 6% off.

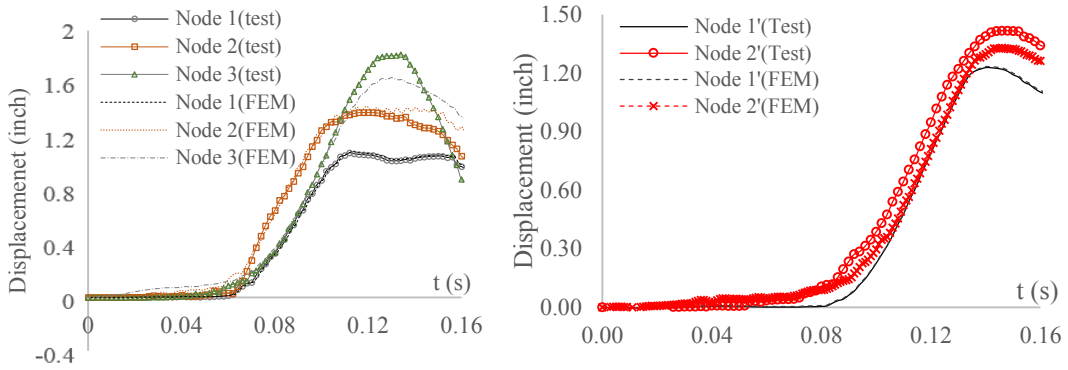

(a) Weak column. (b) Strong column.

Figure 66. Graphs. Critical points displacement for the impacting into the weak and strong column scenario.

Strain Time History

Figure 67 shows a comparison between the computed and measured strain time histories up to 160 ms at selected locations. For strain gauges on longitudinal bars on the weak pier, strain gauges at CH20, 27 and 28 broke during the testing. Hence, figure 67 shows comparison between strain time history for CH19 and CH21 (strains in stirrups). For CH19, strain levels were close to the yield strain level of 2,450. Strain levels in the stirrups in figure 67(b) were quite low, indicating that shear demands were not high, which is confirmed in the simulation results as well. The simulation results showed that strains at the locations of broken strain gauges were well in excess of the yield strains. Combined with the elevated strain rates associated with the impact event, these high strain demands may have contributed to breaking the strain gauges.

Figure 68 shows the strain history data for the strong pier at CH9 and CH10. Unlike the weak pier test, the strain in the main reinforcement did not achieve yield. For example, CH9, which has the highest strain level, reached 90% of the yield strain at impact. The lower strain levels are consistent with the observed smaller crack widths in this test compared to that for the weak pier.

Clearly, the computational and experimental results for strains do not match as well as the displacement data. However, they are nevertheless deemed acceptable because of: 1) the difficulty of modeling a field experiment, which is not as well controlled as a lab experiment, and 2) the fact that strains are quite sensitive to local effects such as cracking. Cracking can cause significant variations in the local steel strains, which cannot be captured by the FE simulation because it does not explicitly model the formation of a crack. The computational model also assumes strong bond between steel and concrete, which may not be the case in the experimental model.

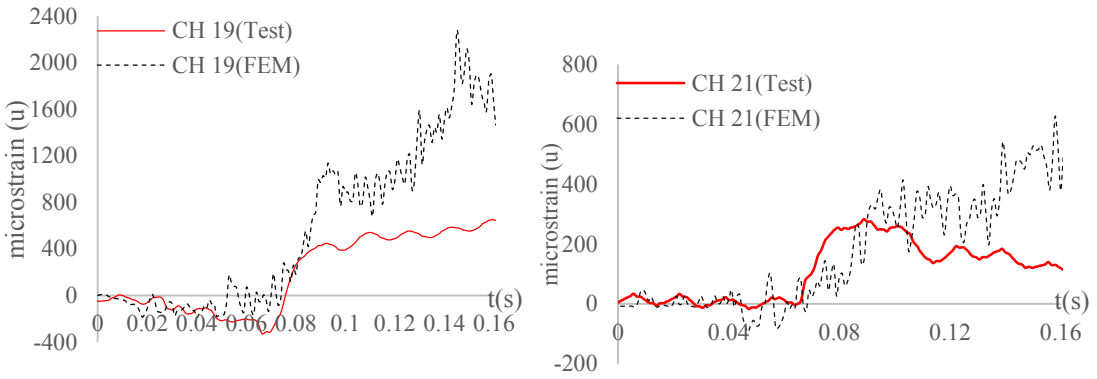

(a) Channel 19. (b) Channel 21.

Figure 67. Graphs. Strain time history at selected locations during weak pier test.

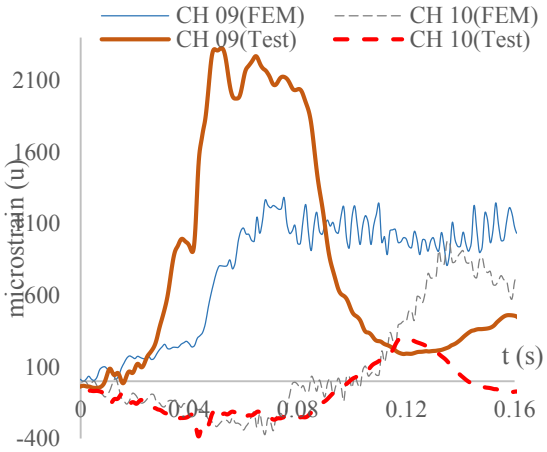

Figure 68. Graph. Strain time histories for CH9 and CH10 during strong pier test.

CHAPTER 4. HEAVY VEHICLE SIMULATION

INTRODUCTION

The literature review in chapter 1 shows that the majority of computational research on the truck-pier collision problem was conducted using the single unit truck model (e.g., El-Tawil et al. 2005, Liu 2012, Agrawal et al. 2012, Chen et al. 2016a, Chen et al. 2016b, Xu 2017). However, the majority of truck impacts on bridge piers have been caused by tractor-semitrailers weighing up to 80,000 lb load (Buth et al. 2011). These trucks are categorized as heavy trucks.

As noted in chapter 1, Buth et al. (2010) carried out a preliminary computational study using tractor-semitrailer models. In their simulation, the piers were modeled as rigid with fixed boundary conditions (top and bottom). The heavy truck model employed accounted for elastic-plastic material behavior of the steel components of the truck. The cargo (modeled as a single ballast) was assumed to be either rigid or deformable. Because of the rigid column assumption, the computational studies in Buth et al. (2011) and experiments carried out in Buth et al. (2010) don't provide loading definitions for impacts by heavy vehicles on concrete bridge piers, which are deformable and are damaged during impacts. This can affect the impact loading on the pier.

Recently, Miele et al. (2010) developed a model in LS-DYNA for a tractor-semitrailer with a total weight of 80,000 lb, as shown in figure 69. This model was originally developed for crashworthiness studies of barriers. The heavy truck model is a van-type tractor-semitrailer with dimensions of 66 ft x 9 ft x 13 ft. The tractor-semitrailer model is representative of models such as 1991 White GMC tractor with a 1988 Pines 48-ft (14.6-m) Semitrailer, 1979 International TranStar 4200 tractor with a 1977 Pullman van-trailer and 1992 Freightliner FLD120 with integral sleeper cabin and 1990 Stoughton box semitrailer (Miele et al. 2010). This model has approximately 472,000 finite elements, including shell, beam, and solid elements for different parts of the truck.

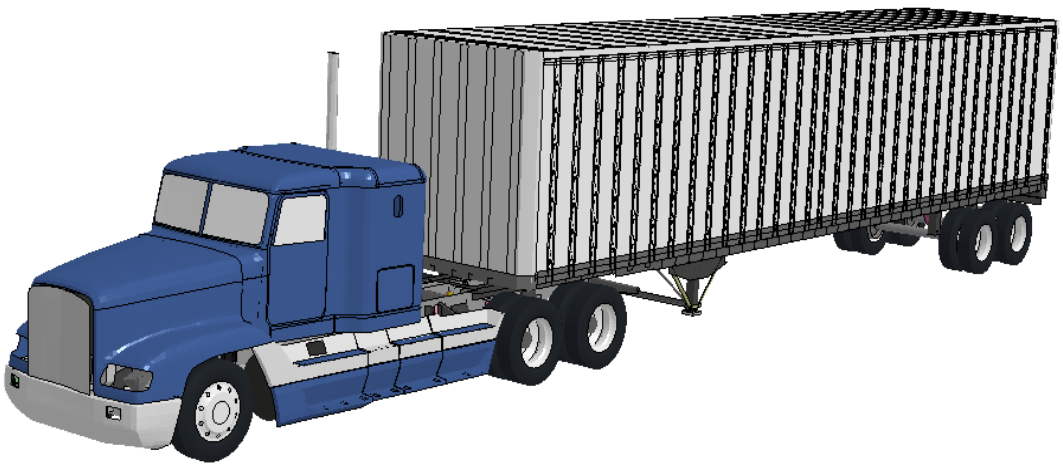

Figure 69. Photo. FE model of tractor-semitrailer in LS-DYNA.

The tractor-semitrailer model developed by Miele et al. (2010) was further modified for studying vehicular impacts on bridge piers and has been validated against the field test conducted by TTI (Buth et al 2011). Figure 70 shows the comparison between the real truck used during the TTI testing and the truck model in LS-DYNA. The LS-DYNA model developed by Miele et al. (2010) has been adapted to the dimensions and properties of this truck model. The major differences between the two models in figure 70 are:

- Wheel base length of FE tractor was 16.2 inches shorter than the test vehicle.
- Empty weight of FE vehicle was 6,300 lb lesser than that of test vehicle (17% less).
- The weight of ballast in the FEM model was 6,600 lb greater than that of the test vehicle (15% greater).

(a) Original truck model. (b) Truck model in LS-DYNA.

Figure 70. Photos. Comparison between the real and FEM truck models (Plaxico 2015).

Overall, the FEM truck model has very similar physical properties as the real truck model. Based on a calibration with full-scale test results at TTI, the following major modifications were made to the FEM model by Plaxico (2015)[2]:

- Changed failure strain for u-bolts to 0.16
- Repositioned u-bolts to eliminate initial penetrations
- Updated material properties for u-bolts based on material tests performed at Battelle
- Remeshed front components of tractor for impact with rigid pole
- Remeshed the fifth-wheel
- Changed nodal rigid body (NRB) connections to generalized- weld-with-failure for all frame-bracket connections
- Changed connection of cabin to frame rails to constrained joints with failure conditions
- Changed several NRB connections to spotweld with failure conditions
- Included failure strain for all materials (HSLA steel failure set to 0.2)
- Corrected thickness of drive shaft.
- Removed steel plates behind the cabin (these were included on the original model to replicate the mounting plates installed for mounting the data acquisition equipment on the FOIL vehicle).
- Changed engine material from elastic to elasto-plastic.
- Changed mass of engine to match the weight of a Detroit DD15 14.8L plus 45 quarts of oil.

[2] Chuck A. Plaxico (2015). FEA vs TTI Test 429730-2, Preliminary Validation Analysis. Roadsafe LLC.

- Added mass to the floor and firewall to make up for the reduction in engine mass from previous change.

In the full-scale test performed at TTI, the 80,000-lb test truck traveled at 50 mph and collided head on with the rigid column. Figure 71 shows the engine-impact scenario during the test and in the simulations performed by Plaxico (2015). It is noted that the simulations match the test results reasonably well. A closer comparison of the impact force time history is shown in figure 72. When the engine impacts the column, the peak force during the test is around 830 kips and that from the simulation is 928 kips, i.e., approximately 10% higher. Considering the complexity of the impact test, peak forces during the test and FEM simulation for the engine impact are considered in good agreement.

After the engine impact, the trailer hits the column generating another spike in the impact force. Figure 73 shows the trailer-impact scenario during the test and the FEM simulations. It is observed from figure 73 that the tractor is heavily squeezed and totally destroyed by the trailer impact. The damage mode and deformations of the truck model are similar to those observed from FEM simulation results. Figure 72 also shows time history of impact force during trailer impacts. The peak impact force during the test was measured as 513 kips. The peak impact force based on the LS-DYNA simulation by Plaxico (2015) was 465 kips, which is reasonably close to the measured value of 513 kips.

These results show that the modified FEM model of the tractor-semitrailer is capable of simulating impact effects on rigid piers. Considering the complexity of the vehicular impact process, this level of accuracy is acceptable for simulating the effects of vehicular impacts using the FEM model of the truck.

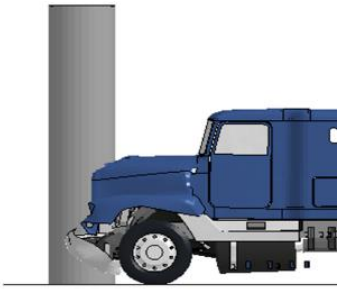

(a) Engine impact on pier during field testing. (b) Engine impact on pier in LS-DYNA.

Figure 71. Photos. Engine impacts with the rigid steel pier during test and simulations.

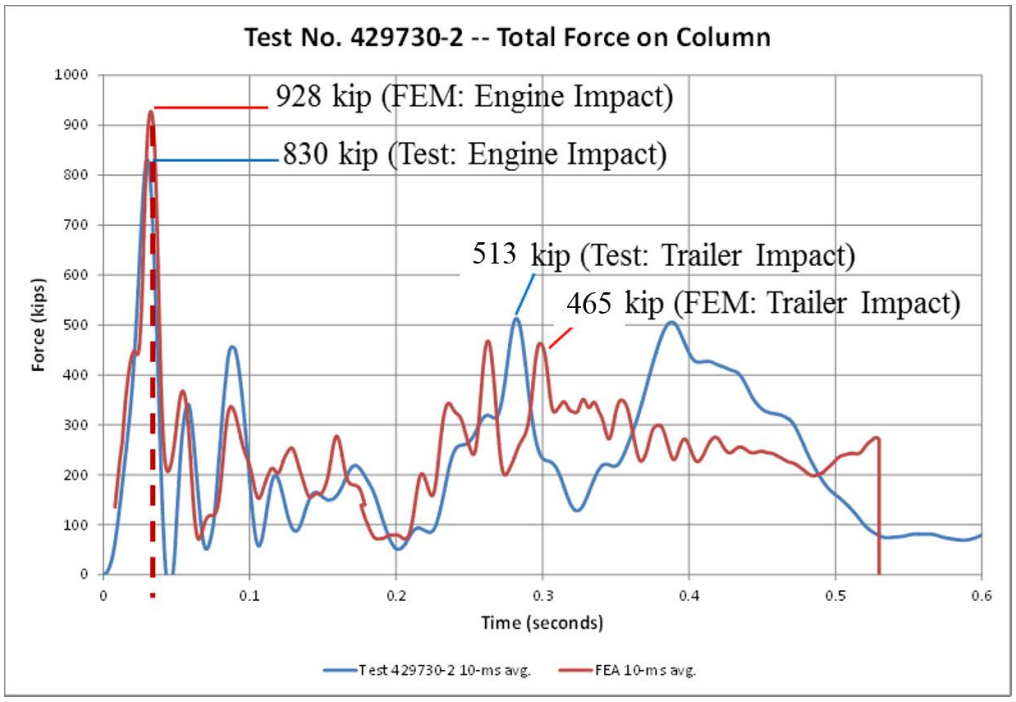

Figure 72. Graph. Impact force time histories during the test and FEM simulation in LS-DYNA.

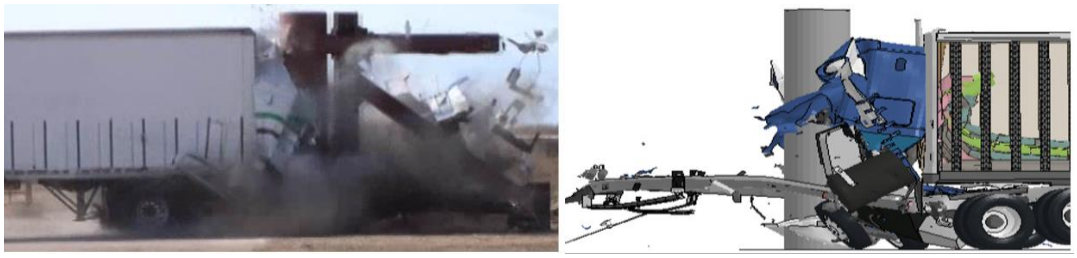

(a) Trailer impact on pier during field testing. (b) Trailer impact on pier in LS-DYNA.

Figure 73. Photo. Trailer impacts with pier during test and LS-DYNA simulation.

CALIBRATION OF THE FEM MODEL OF TRACTOR-SEMITRAILER FOR DEFORMABLE PIERS

The tractor-semitrailer model is the most advanced among its vehicle class because of its sophisticated geometric details, physical functions, and the accuracy of its material properties. It has been found to be stable during simulation of impacts on concrete piers. However, further modifications were made to the FEM model to ensure acceptable simulation results.

Ground Contact

In the original truck model, contact is defined between the tires and the ground through the command RIGIDWALL_PLANAR. However, the nodal set of slave nodes defined in the rigid wall is applied to all nodes in the model, which means all the elements of the simulation and any

new ones interact with the ground as if it were a rigid support. The generality of the contact specification implies that the newly added pier interacts incorrectly with the ground, i.e., it is rigidly supported in the horizontal direction at the ground plane, which is 2.4 ft higher than the bottom of the pier (figure 74(a)). The improper contact disrupts the analysis as shown in figure 74(b). As noted in figure 74(b), the underground portion of the pier is undeformed and the shear failure plane starts from the ground level instead at the bottom of the pier where fixity actually exists. To correct the contact between the ground and pier, the nodes of the pier model are exempted from the slave nodal set to the ground in the updated model. Figure 74(c) shows the damage mode of the pier with corrected ground contact. It is observed that the shear failure plane starts from the bottom of the pier where the fixed boundary condition is defined.

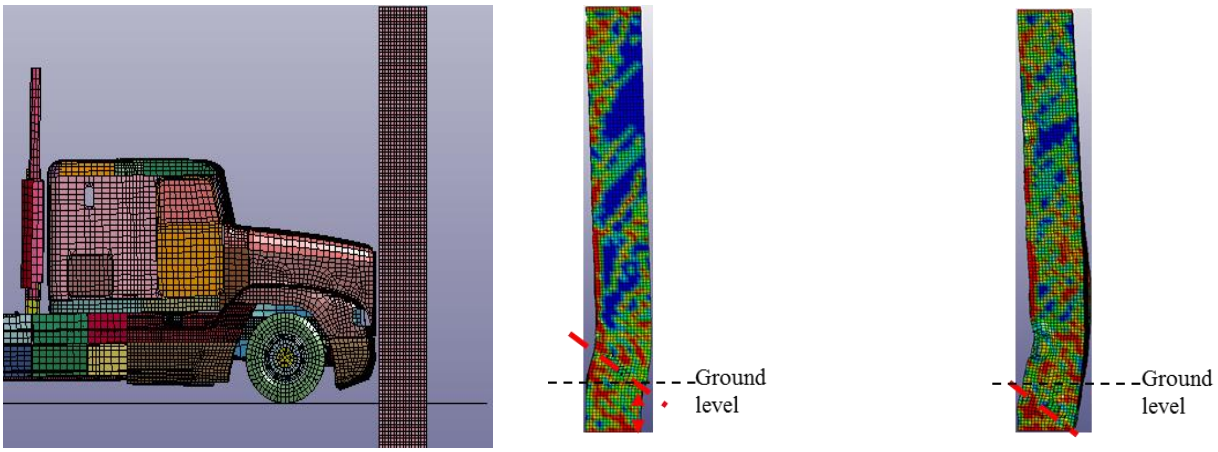

(a) FE model setup. (b) Original ground contact. (c) Corrected ground contact.

Figure 74. Illustration. Ground contact issue during LS-DYNA simulation.

Sharp Edges in Engine

Based on the work by Plaxico (2015), it was noted that engine impact delivers the highest demand to the pier. However, the engine geometry isn't regular (figure 75) and one of its parts (radiator) that comes in contact with the pier has a sharp edge. The sharp edge bears against the inter-element boundary of some of the pier's elements. Since these elements are underintegrated, the high contact force at the inter-element boundary promoted severe hourglassing in the pier.

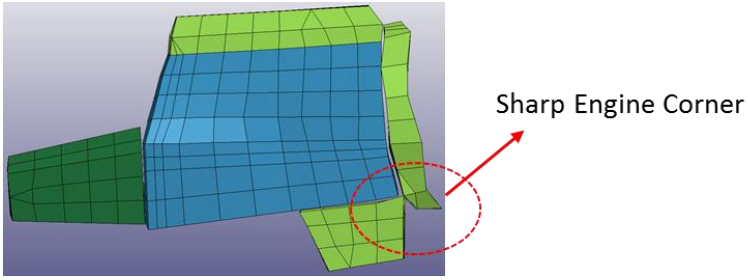

Figure 75. Photo. Sharp engine corner.

To reduce the occurrence of hourglassing, the engine cover was made softer in an effort to reduce the contact force and stave off hourglassing. The thickness of the shell element of the engine cover part is reduced to 40% of its original value, while its density is increased

accordingly to ensure the same mass. This modification eliminated any discernable hourglassing. Figure 76 shows a comparison of the impact force computed using the updated and the original models.

The updated model, incorporating the two modifications noted above, was adopted for subsequent simulations of tractor-semitrailer impacts on bridge piers.

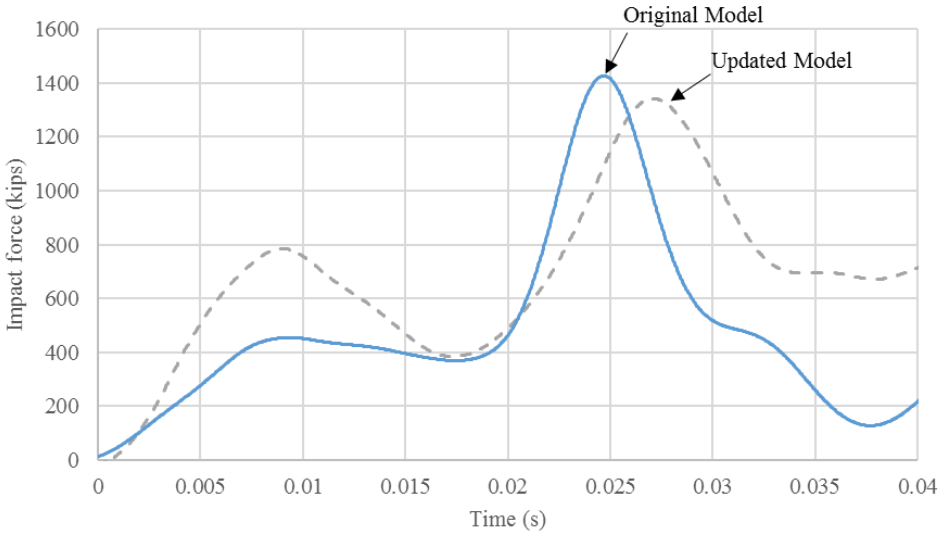

Figure 76. Graph. Impact force using the original and updated truck models.

Pier Model

Liu (2012) investigated impacts by a single unit truck on a three-span simply supported bridge through numerical simulations in LS-DYNA. The three-span simply supported bridge developed by Yi (2009) was first adopted to study the behavior of the bridge piers during vehicular impact loading. Figure 77 shows the FE model of the whole bridge.

However, simulating a whole bridge model requires a significant level of modeling and computational resources. Liu (2012) proposed a simplified pier-bent model for studying vehicular impact hazards on bridge piers. In that model, shown in figure 78, an equivalent mass of the deck, calculated as the sum of the mass contributions from each span, was applied on the top of the bent. For the boundary condition, the top of the bent was fixed in the horizontal direction and the foundation beam was fully fixed. Figure 79 shows comparisons between displacement time-history for 50 mph impact. It is observed that the pier bent model can represent the behavior of the pier during vehicular impact well. The computation time required for simulating the pier bent model is significantly smaller than that for the full bridge.

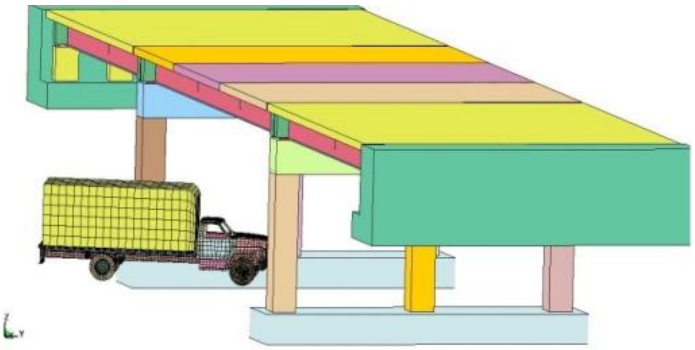

Figure 77. Photo. FE model of the three-span bridge with single unit truck.

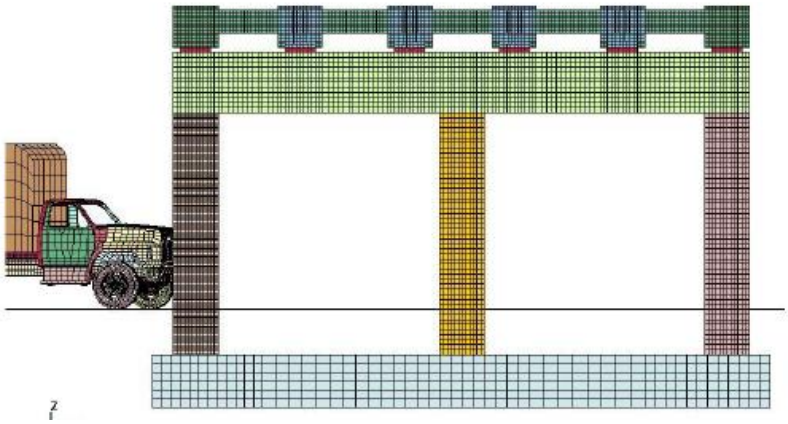

Figure 78. Illustration. Pier-bent model proposed by Liu (2012).

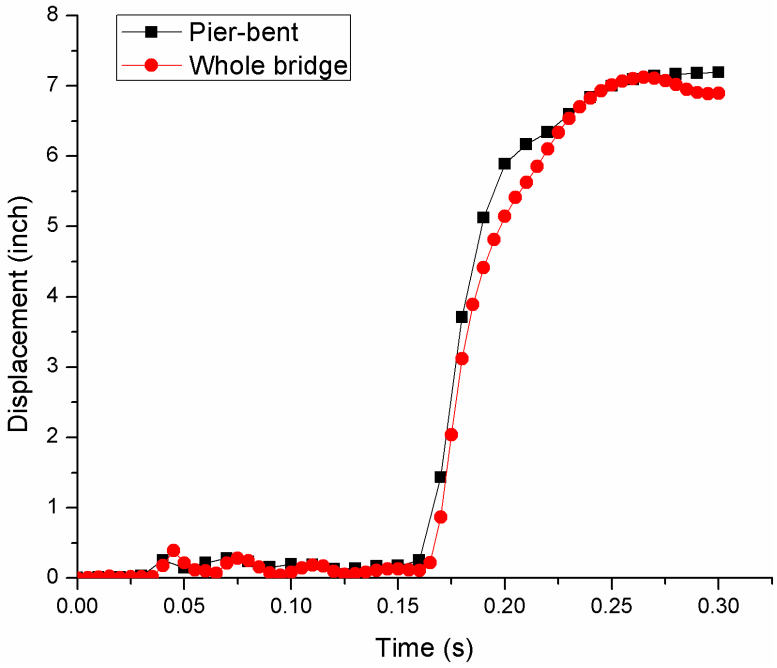

Figure 79. Graph. Displacement time history at impact point considering full-bridge and pier bent models.

To further simplify the pier bent model and still achieve good accuracy, Xu (2017) studied two alternate boundary conditions for piers, as illustrated in figure 80. The medium weight truck with 8-ton weight and an initial impact velocity of 50 mph was chosen as the impact scenario. The truck weight was changed by modifying the density of the cargo.

Figure 81 shows the damage modes for the three cases: pier bent model, pier bent model with fixed boundary condition at the top and a pier with fixed top and bottom boundary condition. It is observed from figure 81 that damage modes for the latter two cases are almost the same as those for the pier-bent mode in figure 81(a). Figure 82 shows time history plots of impact forces and displacement at the impact point. It is observed from figure 82 (a) that the time histories of impact forces for three cases (pier bent, pier bent with fixed boundary condition at top and pier with fixed boundary condition at top and bottom) are almost the same except for some differences in peak values. It is observed that the maximum of the peak impact forces calculated for the pier bent with fixed top and pier with fixed top and bottom boundary conditions are approximately 4.4% and 0.3% higher than that for the pier bent model. The maximum displacements at the impact point for the pier with fixed top and bottom boundary condition is 1.7% less than that for the pier bent model.

The results presented above show that the boundary conditions considered have a minor effect on behavior. Therefore, the bridge pier model with top and bottom fixed boundary conditions can be used to represent the vehicle impact scenario with reasonable accuracy. Hence, all further simulations on vehicular impacts on bridge piers have been carried out by utilizing this simplified condition as shown in figure 83.

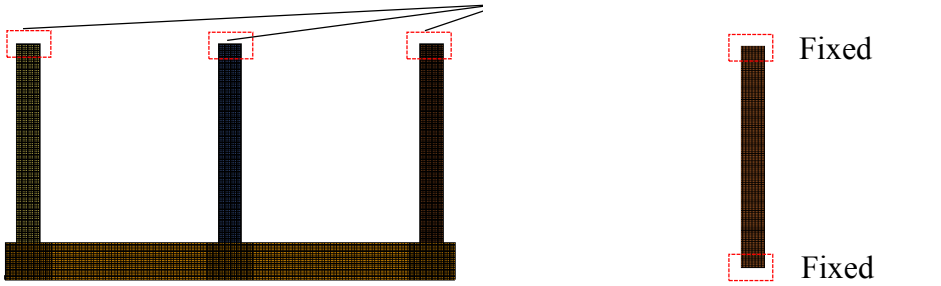

(a) Fixed top. (b) Fixed top and bottom.

Figure 80. Illustration. Boundary condition of the pier.

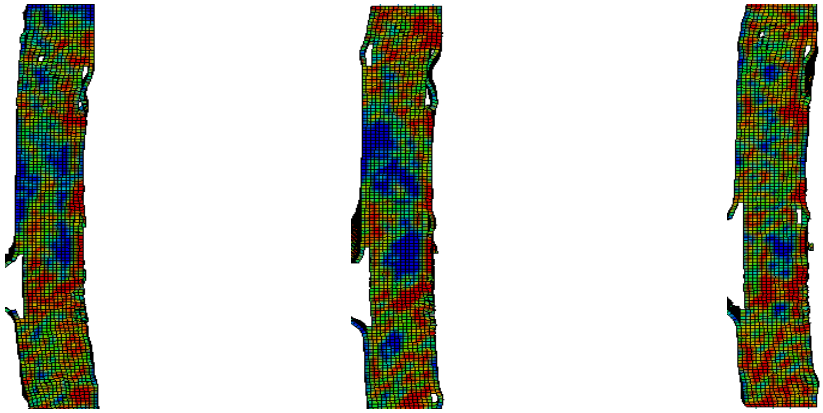

(a) Pier bent. (b) Pier with fixed top. (c) Pier with fixed top and bottom.

Figure 81. Illustration. Damage modes of piers with different boundary conditions.

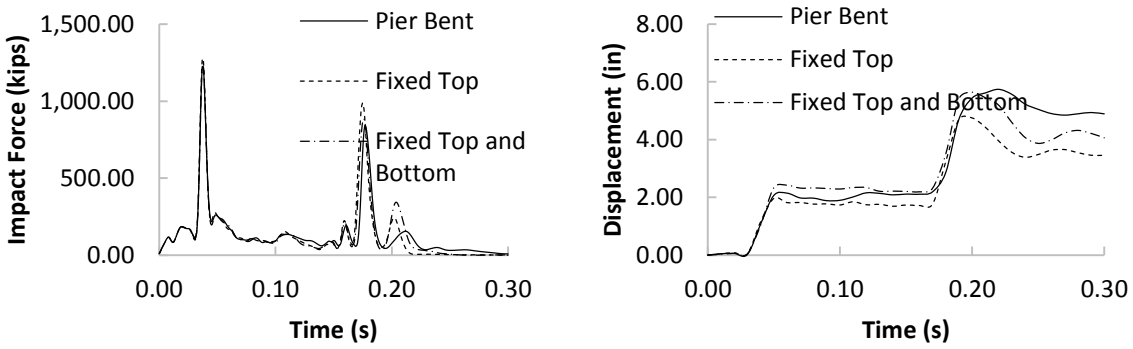

(a) Impact force time history. (b) Displacement time history at impact point.

Figure 82. Graph. Force and displacement time histories for piers with different boundary conditions.

Figure 83. Illustration. Finite element model with fixed-fixed boundary condition pier.

Both rectangular and circular piers are considered in this project. The sizes of the pier considered are 24, 30, 36, and 42 inches. The pier height is assumed to be 16 feet, which is a commonly used height. The details of the various pier sections are shown in table 7**.** The different rectangular piers represent prototypes adopted from Liu (2012) that were designed for different seismic zones. The reinforcement design for circular piers is based on that used in Buth et al. (2010). Section details of these piers are shown in figure 84.

Table 7. Geometry and reinforcement arrangement of piers in the example bridges.

Column ID	Column Size (in)	Pier Height (ft)	Longitudinal Bars	Stirrups Bars
1	24 (square)	16	#14 4 x 4	4 x #3 6 in Spacing
2	30 (square)	16	#10 4 x 4	4 x #3 12 in Spacing
3	36 (square)	16	#11 4 x 4	4 x #3 12 in Spacing
4	42 (square)	16	#14 4 x 4	4 x #4 12 in Spacing
5	30 (circular)	16	8 x #10	#3 Circular 6 in Spacing
6	36 (circular)	16	8 x #14	#3 Circular 6 in Spacing
7	42 (circular)	16	8 x #14	#4 Circular 6 in Spacing

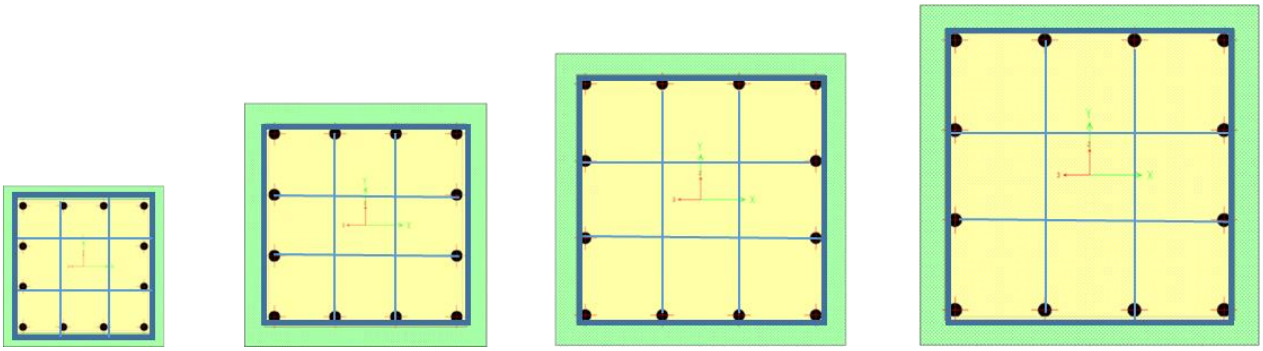

(a) 24 inch. (b) 30 inch. (c) 36 inch. (d) 42 inch.

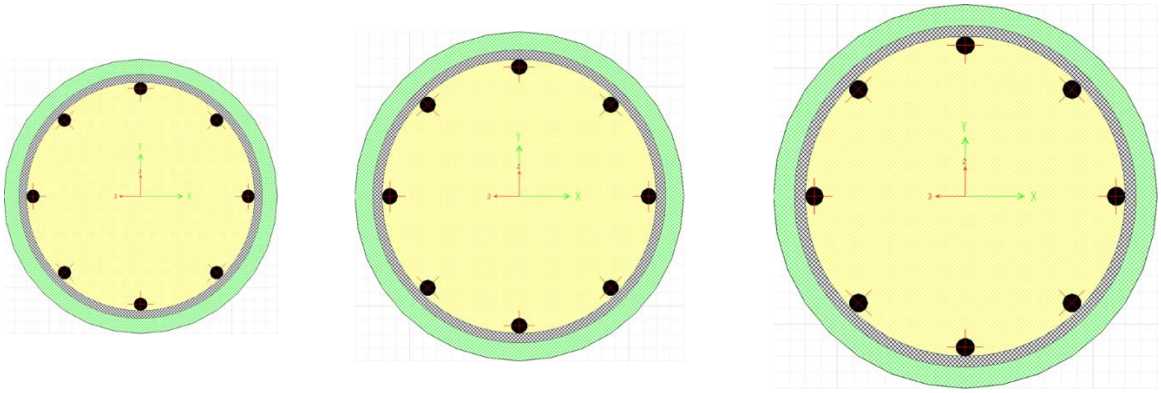

(e) 30-in circular pier. (f) 36-in circular pier. (g) 42-in circular pier.

Figure 84. Illustration. Different sections of the pier.

MODELING OF VEHICULAR IMPACT FORCE

Rectangular Pier

Liu (2012) investigated the impact force demand caused by single unit trucks. The force time-history for such situations has two peaks, one corresponding to the engine impact and other corresponding to the cargo impact. He proposed an equation that is function of the truck weight and velocity to represent the peak impact force through regression analysis of impact force data. Liu (2012) did not consider dynamic effects of impact on bridge piers in his proposed design methods.

Chung et al. (2014) investigated the performance of precast pre-fabricated bridge columns subjected to vehicular impacts. They derived an impact-loading time function, which was derived by approximating the impact time history by a 5-point piecewise approximation such that the area under the impact force time history is the same as than under the piecewise linear function. Response of the column under vehicular impact and piecewise function loading was observed to be the same.

More recently, Xu (2017) proposed a pulse model to present the impact force time history. In this model, the impact force time history is modeled by a time-history function with two triangular

pulses, as illustrated in figure 85. Extensive simulation results by Xu (2017) have shown that the proposed pulse model is capable of representing vehicular impact force time history quite reasonably.

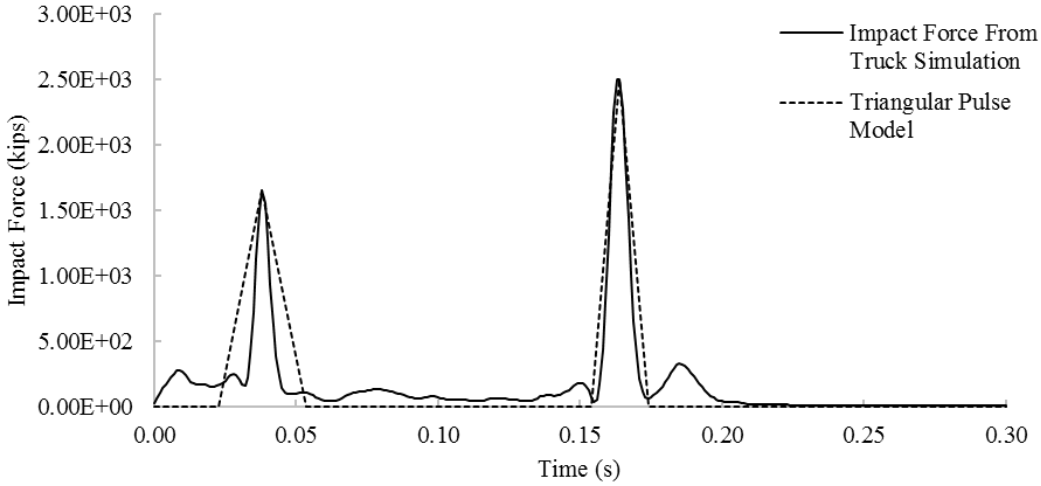

Figure 85. Graph. Pulse model for impact force time history for impact by single unit truck on bridge piers.

Similar to the approach used by Xu (2017) for single unit trucks, the impact force on bridge piers caused by the tractor-semitrailer can be represented by a well-shaped pulse. Figure 86 shows the time history of the impact force caused by impact of 80,000-lb truck on a 36-in rectangular pier at 50 mph. Three distinct peaks are observed in the impact force time-history in figure 86. The first peak is related to bumper impact on the pier while the second peak is related to the engine impact. The third peak is attributed to the trailer impacting the pier. These three peaks are characteristic of other impact scenarios also. The impact force time history in figure 86 can be reasonably represented by a three-triangle pulse time history function shown in figure 87. The proposed pulse model consists of 10 parameters: 5 parameters for the forces, and 5 parameters for the corresponding time of application of the pulse. Essentially, the pulse force starts at time t = 0 s, applies triangular forces at different time instants through 3 peaks through 5 key points and ends at time t = 0.8s.

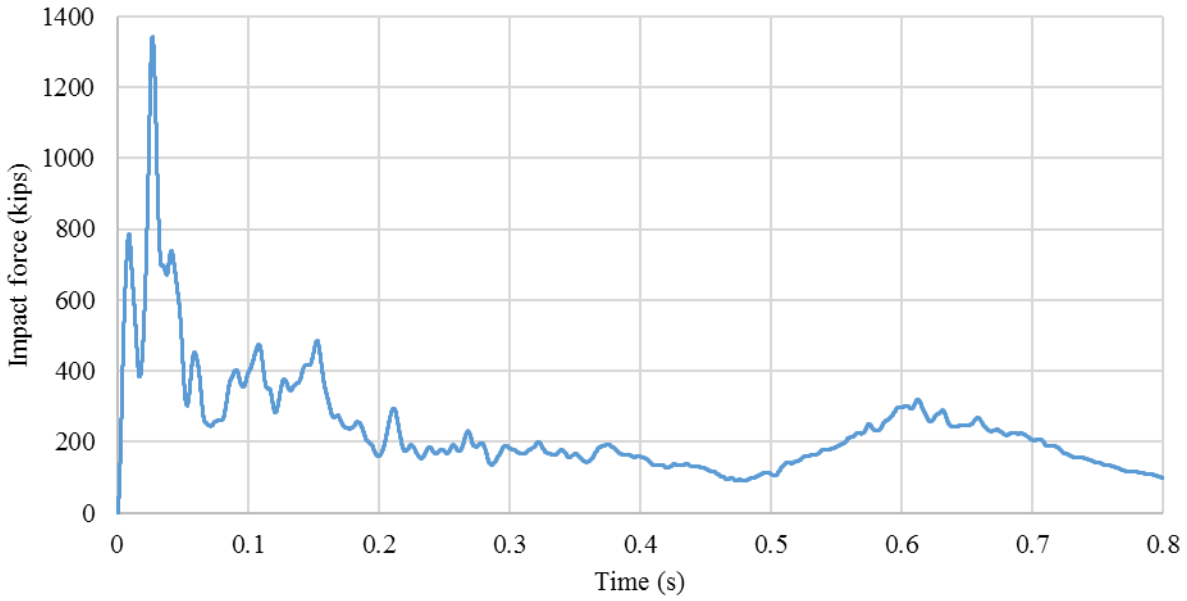

Figure 86. Graph. Time history for impact force by the tractor-semitrailer on a rectangular concrete pier.

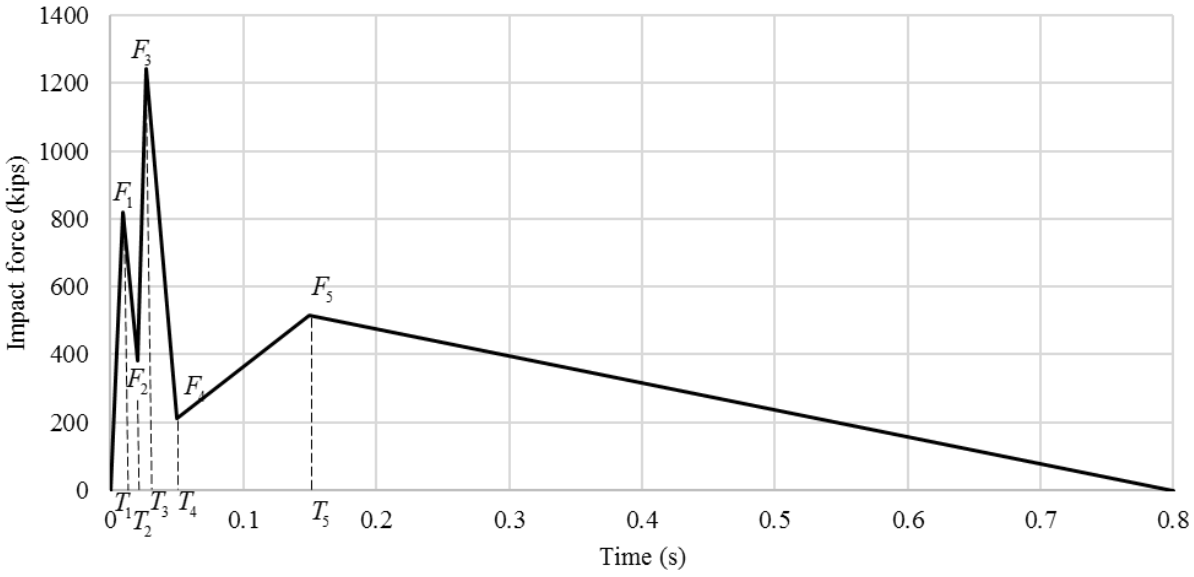

Figure 87. Graph. Proposed triangular pulse model for heavy vehicle impacts on bridge pier.

In order to generalize the proposed pulse model shown in figure 87, an extensive parametric study was carried out by varying pier size, impact speed and truck weight. The truck weight is varied between 20 tons to 40 tons with 10 ton increments by modifying the density of its cargo. The pier dimensions considered in the parametric study are shown in table 7. The truck velocity is varied in the range of 30 mph to 70 mph. For the purpose of reference, a unique descriptive

name has been given to each scenario. For example, P3_V50_W40 implies impact on pier case 3 in table 7 by a 40 ton truck with 50 mph impact velocity.

Before proceeding with the parametric simulations, a number of simulations were carried out to resolve the following two issues: (i) height where the pulse impact is applied and (ii) expressions for parameters F1 to F5 and T_1 to T_5 in figure 87. Resolutions of these two issues are described in the following sections.

Points of Application of Pulse Impacts

Figure 88 shows a contour plot of the impact force along the height of the pier as the truck impacts the pier. The case shown in figure 88 represents a 40 Ton truck impacts the 36-in rectangular pier at 50 mph velocity. It is observed from the figure 88 that there are three impact zones: (i) the first one is associated with the bumper impact between the height of 0.6 ft to 1.6 ft above the ground, (ii) the second one is due to engine impact between the height of 1.6 ft to 3.4 ft, above the ground and (iii) the third one because of the trailer impact between the height of 1.1 ft to 2.1 ft above the ground. The proposed pulse loading in figure 87 is represented as three pulses $Pulse^1$, $Pulse^2$, and $Pulse^3$ in figure 89 and is applied as a pressure (i.e., impact force divided by the area of the impact zone) on the three zones, as illustrated in figure 89. These three impact zones are 3 ft, 4 ft and 3.5 ft, respectively, over the bottom of the pier. The loading height of these three impact zones are 1-foot, 1.75-feet and 1-foot high, respectively.

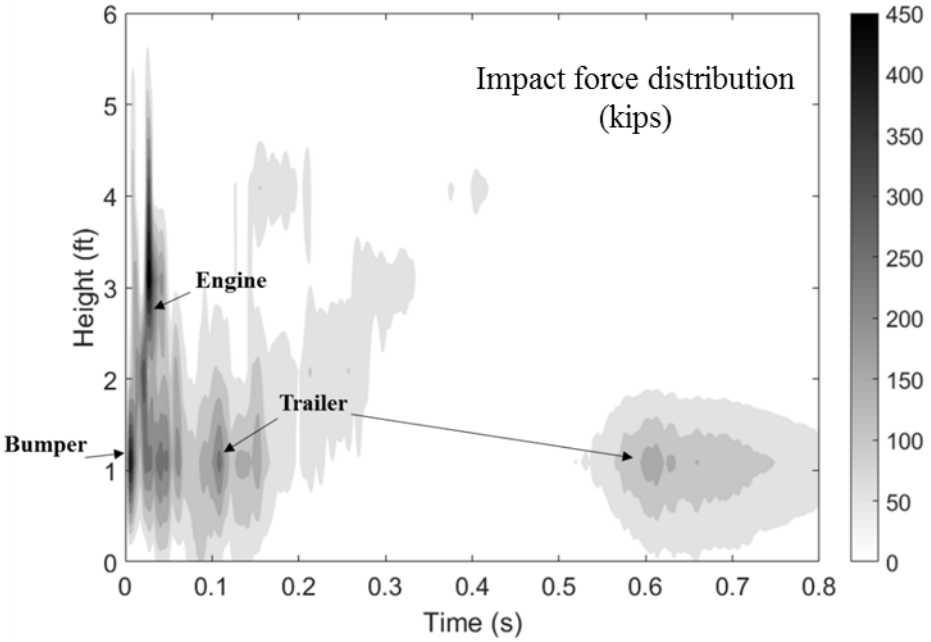

Figure 88. Graph. Contours of impact force distribution along the height of the pier for case P3_V50_M40 (unit: kips).

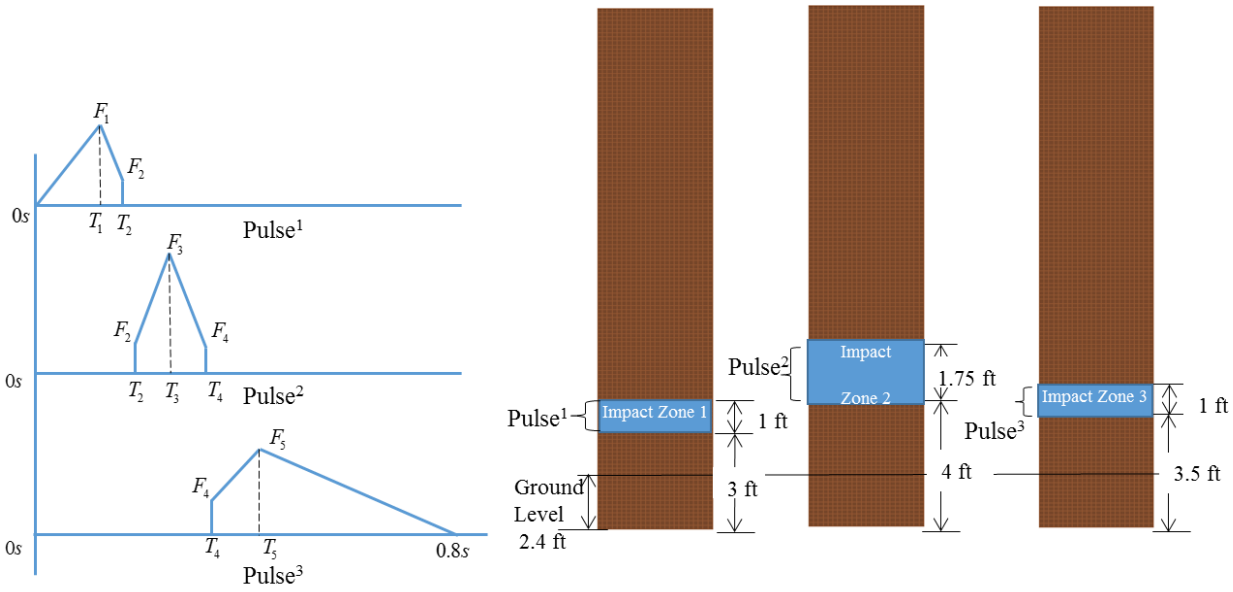

Figure 89. Illustration. Application of impact pulse loading function of the pier.

The "actual" pulse outlined in figure 86 was applied to the pier at the impact zones identified in figure 89. For example, the portion of the impact force time history in figure 86 corresponding to pulse^1 (bumper impact) is applied to impact zone 1 in figure 89. This situation is termed "original pulse simulation". Figure 90 shows the damage modes of the pier computed for actual truck impact and original pulse simulation cases. It is observed from this figure that the damage modes for both cases match reasonably well. Figure 91 shows a comparison between the displacement time-histories corresponding to the actual truck simulation and original pulse simulation for the case of P3_V50_M40. It is observed that the displacement time-histories for the two cases match reasonably well. Results in figure 90 and figure 91 demonstrate that the impact zones proposed in figure 89 are appropriate for applying pulses representing the impact loading defined in figure 87.

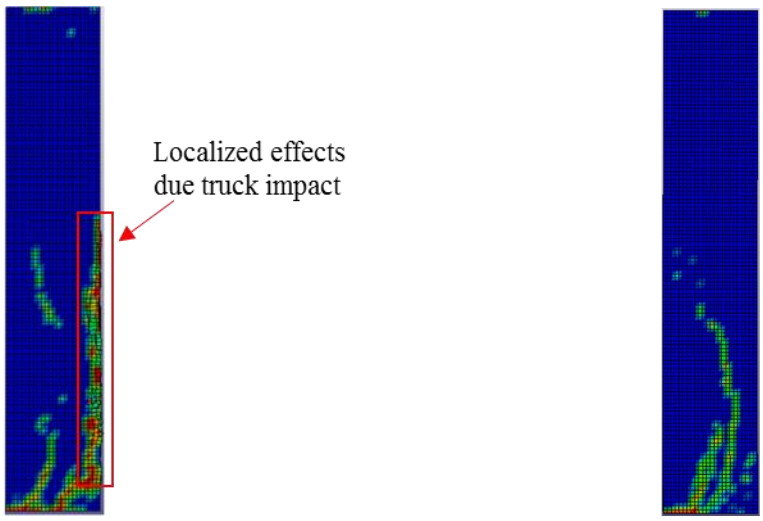

(a) Truck simulation. (b) Original pulse simulation.

Figure 90. Photo. Damage modes comparison for P3_V50_M40 case.

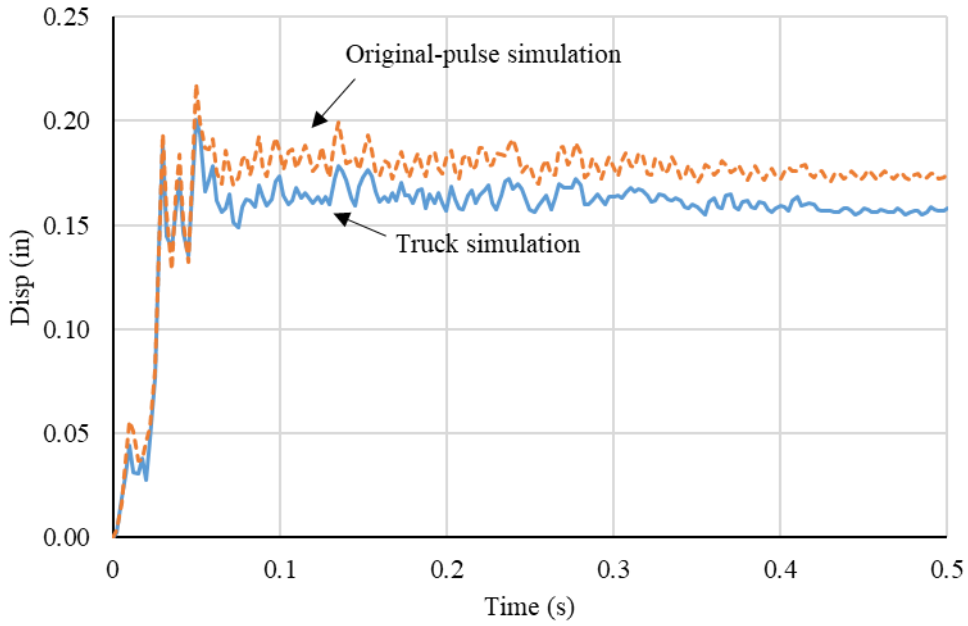

Figure 91. Graph. Displacement time-histories for P3_V50_M40 case.

Parametric Study

Effect of truck velocity

The effect of truck velocity on *F1* to *F5* are computed from truck simulations and illustrated in figure 92 to figure 96. The pier size is selected as 36 in and truck weight is 40 T. It is clear that all the forces increase with the increase of truck velocities. When the velocity increases from 30 mph to 70 mph, *F1* increases from 600 kips to 1,000 kips; *F2* increases from 320 kips to 434 kips; *F3* increase from 681 kips to 1,660 kips; *F4* increases from 172 kips to 290 kips; *F5* increases from 243 kips to 852 kips.

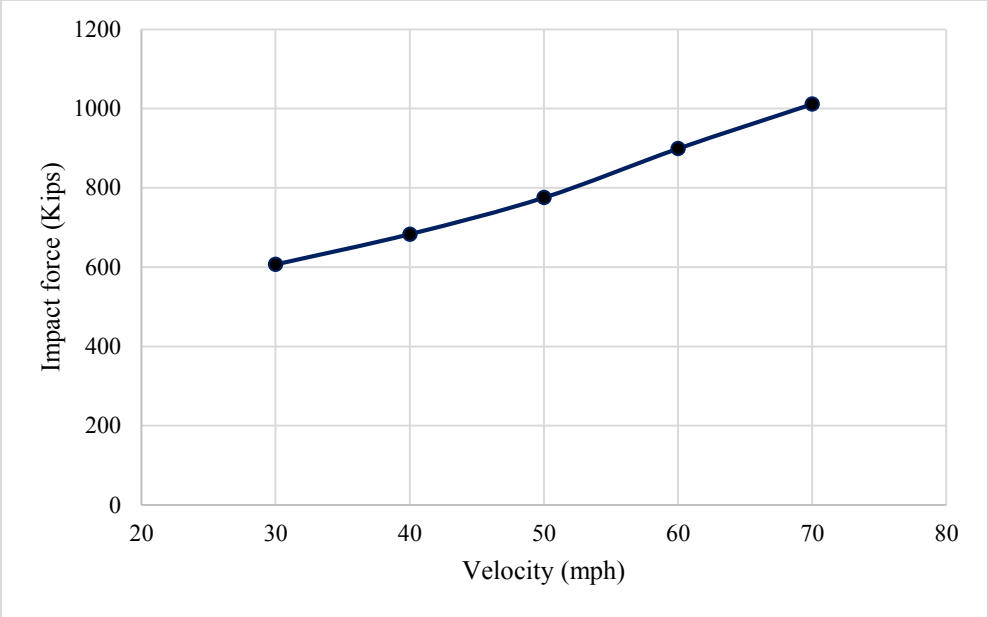

Figure 92. Graph. F1 versus truck velocity for P3_M40.

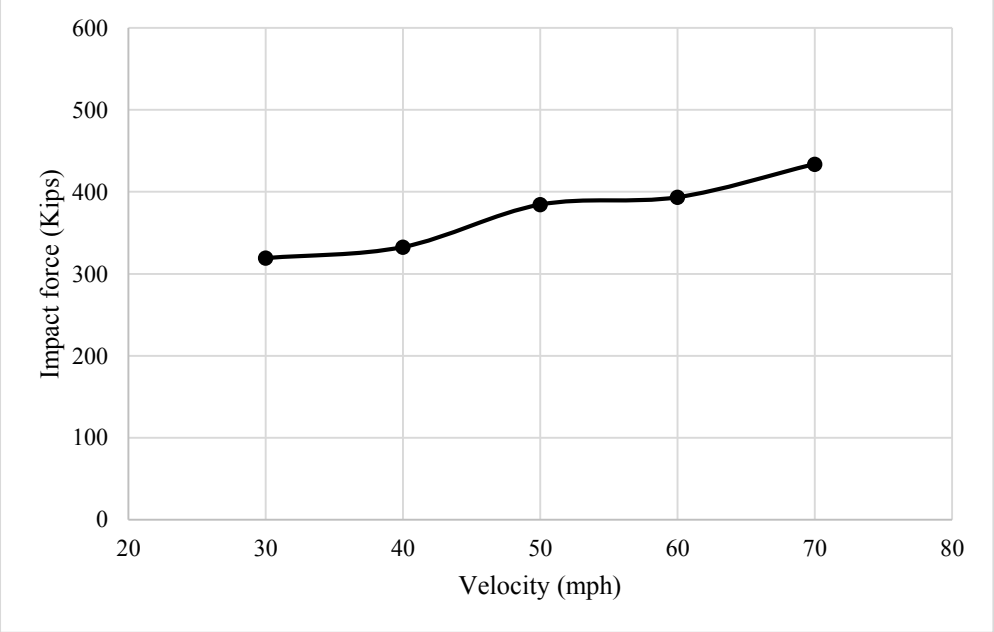

Figure 93. Graph. F2 versus truck velocity for P3_M40.

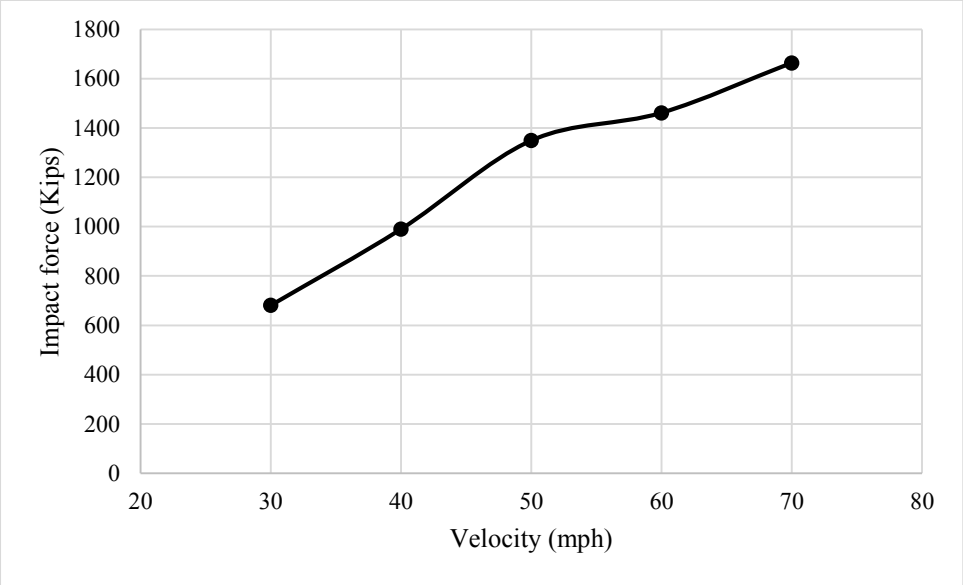

Figure 94. Graph. F3 versus truck velocity for P3_M40.

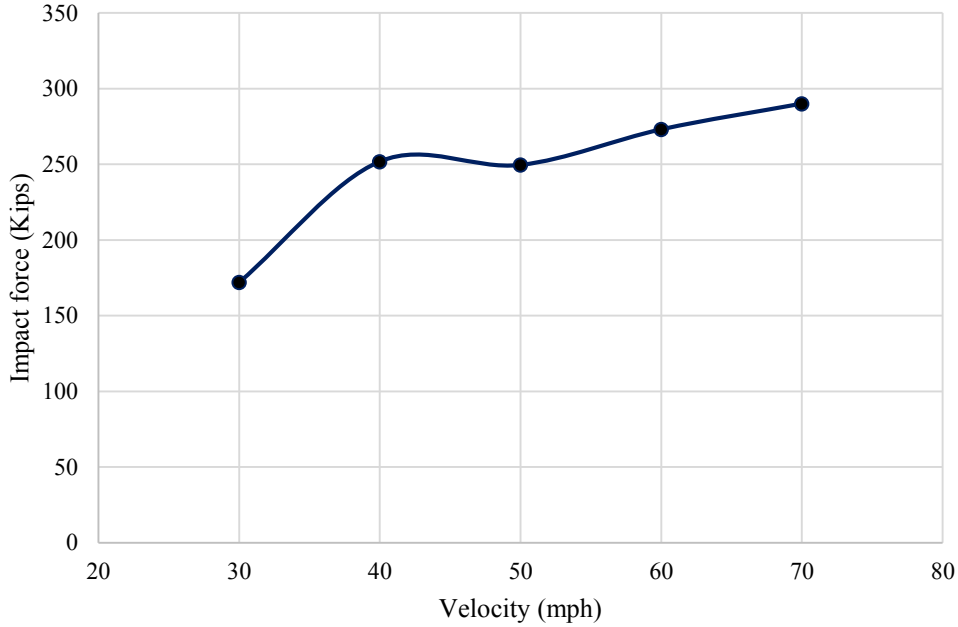

Figure 95. Graph. F4 versus truck velocity for P3_M40.

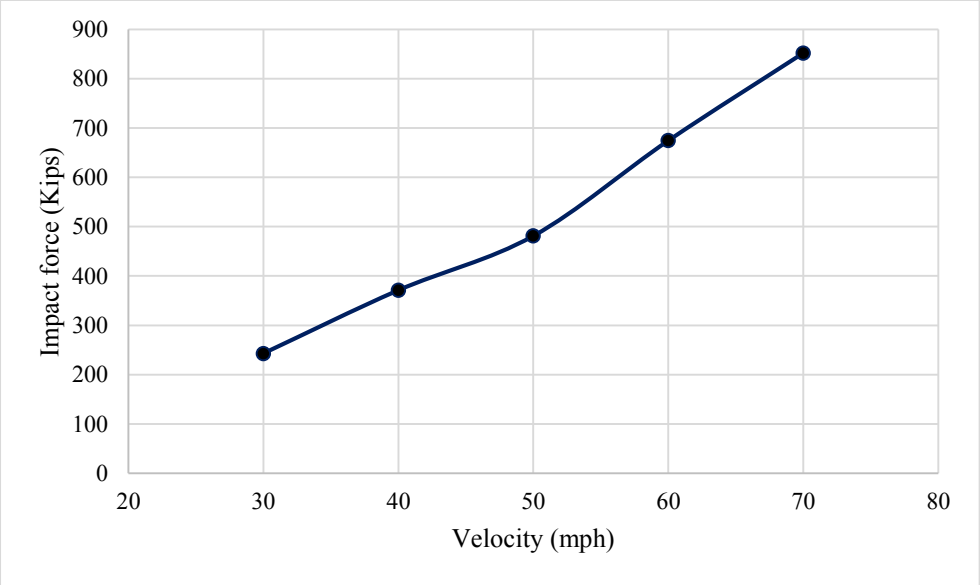

Figure 96. Graph. F5 versus truck velocity for P3_M40.

The effect of truck velocity on T1 to T4 are illustrated from figure 97 to figure 100. The pier size is selected as 36 in and truck weight is 40 T. For T1 to T4, it is clear that the time decreases as the truck velocity increases. When the velocity increases from 30 mph to 70 mph, T1 decreases from 0.014 sec to 0.007 sec; T2 decreases from 0.035 sec to 0.013 sec; T3 decreases from 0.046 sec to 0.019 sec; T4 decreases from 0.088 sec to 0.030 sec. T5 is assumed as 0.22 sec, which is not plotted in the figures. The limitations of the truck model for capturing the trailer impact time is also illustrated in Plaxico (2015).

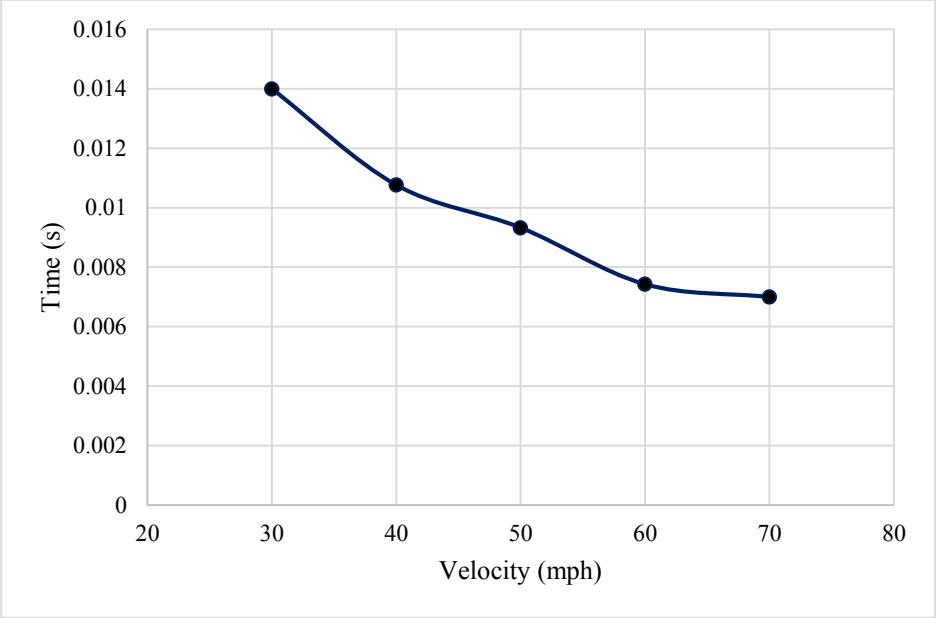

Figure 97. Graph. T1 versus truck velocity for P3_M40.

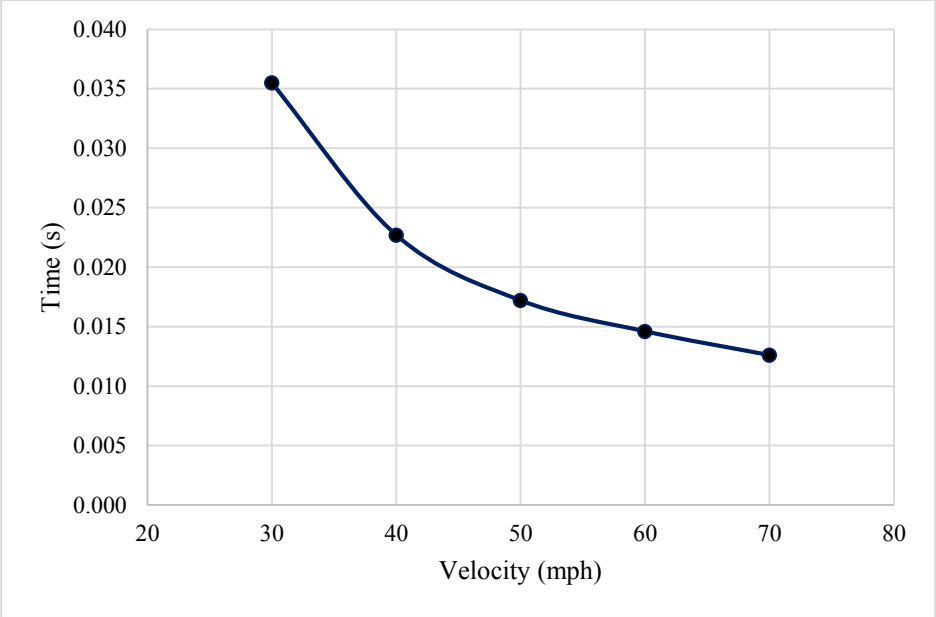

Figure 98. Graph. T2 versus truck velocity for P3_M40.

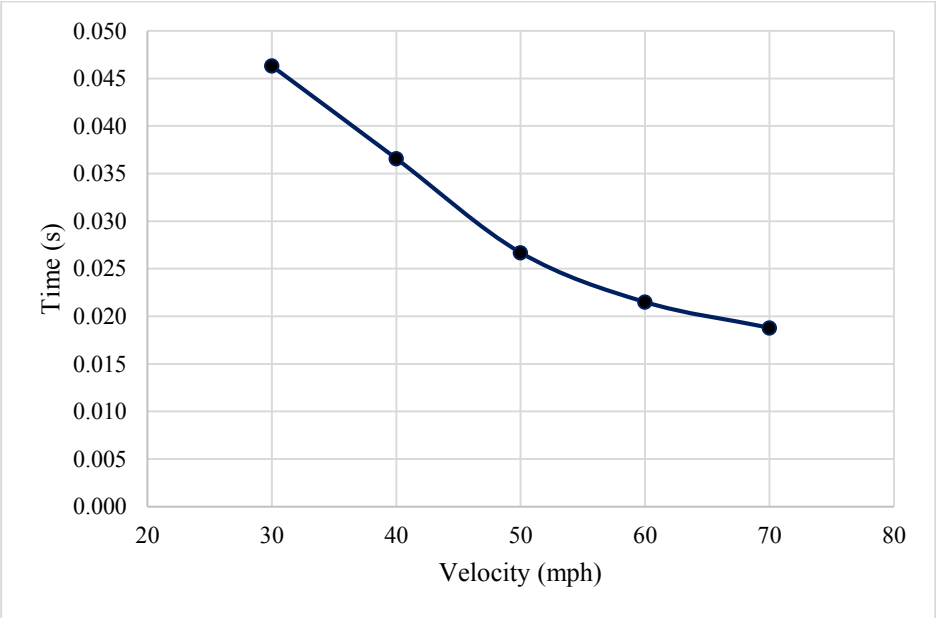

Figure 99. Graph. T3 versus truck velocity for P3_M40.

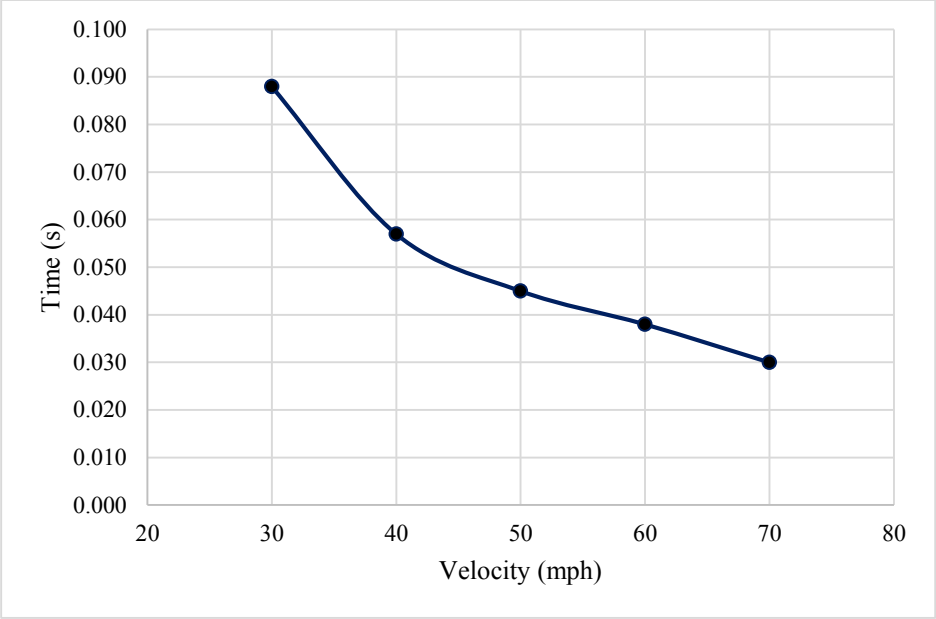

Figure 100. Graph. T4 versus truck velocity for P3_M40.

Effect of pier size

The effect of pier size on F1 to F5 are illustrated from figure 101 to figure 105. The pier size varies from 30 in to 42 in. Truck velocities of 30 mph, 50 mph, and 70 mph are considered. The weight of the truck is selected as 40 T. For F1 and F3, the impact forces are almost constant when pier size varies. For F2 and F4, in general, the impact force decreases when the pier size increases. For F5, the impact force generally increases as the pier size increases. Impact speed less than 50 mph will not generate a clear peak force by the trailer.

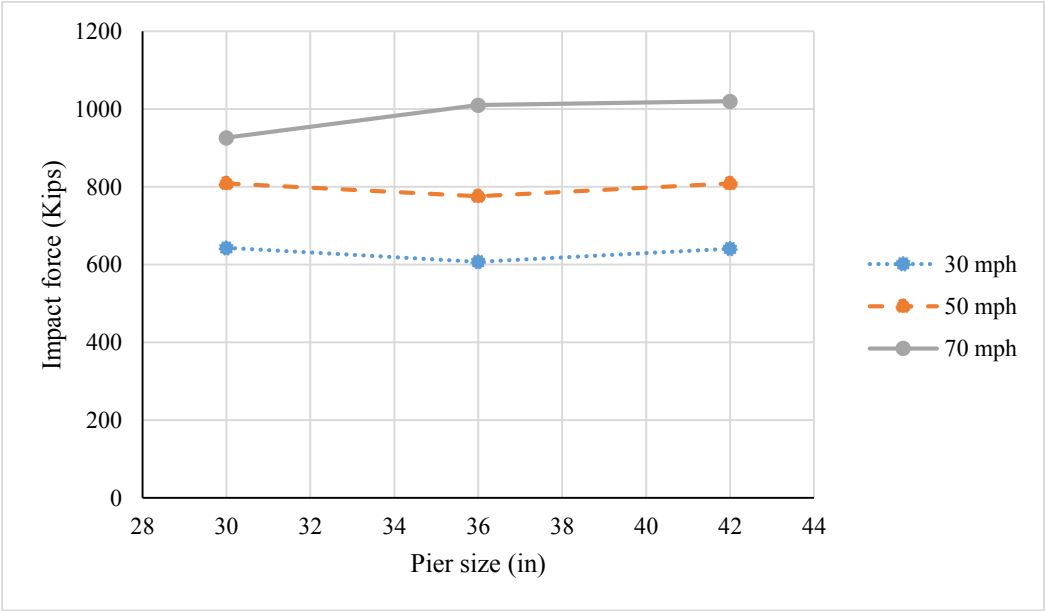

Figure 101. Graph. F1 versus pier size for M40.

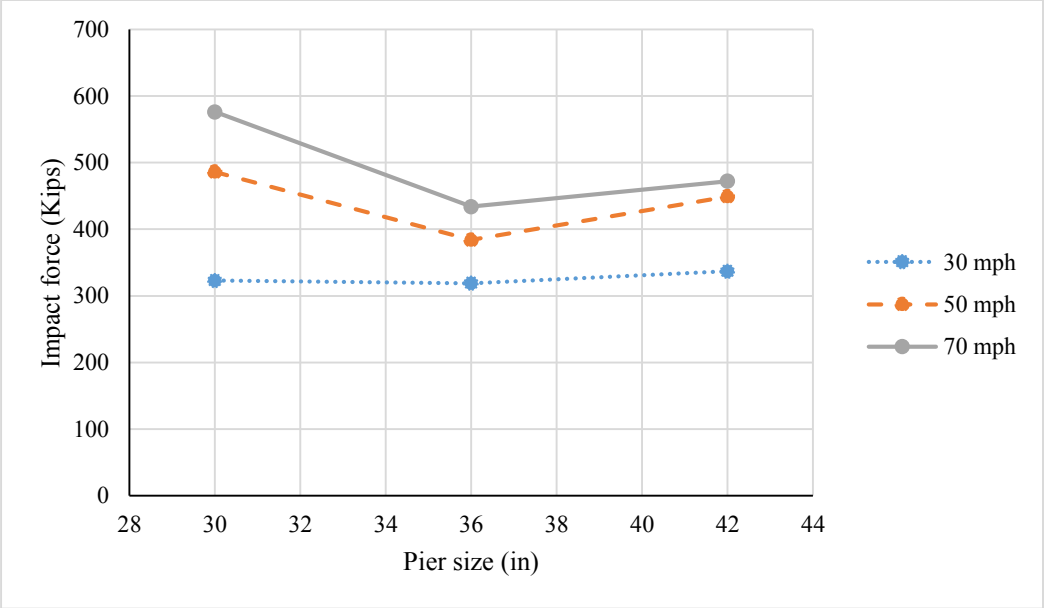

Figure 102. Graph. F2 versus pier size for M40.

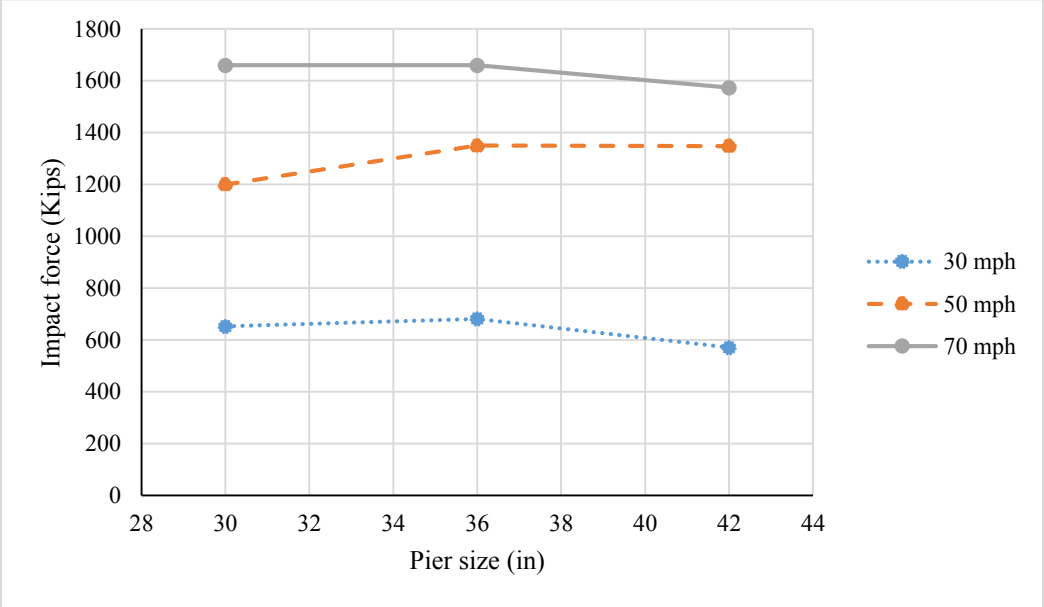

Figure 103. Graph. F3 versus pier size for M40.

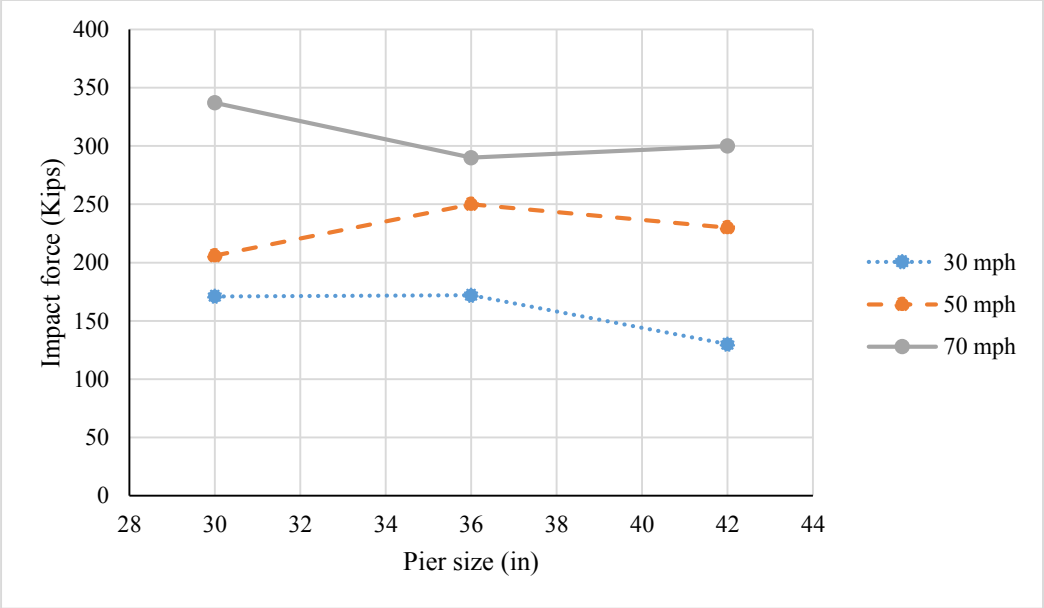

Figure 104. Graph. F4 versus pier size for M40.

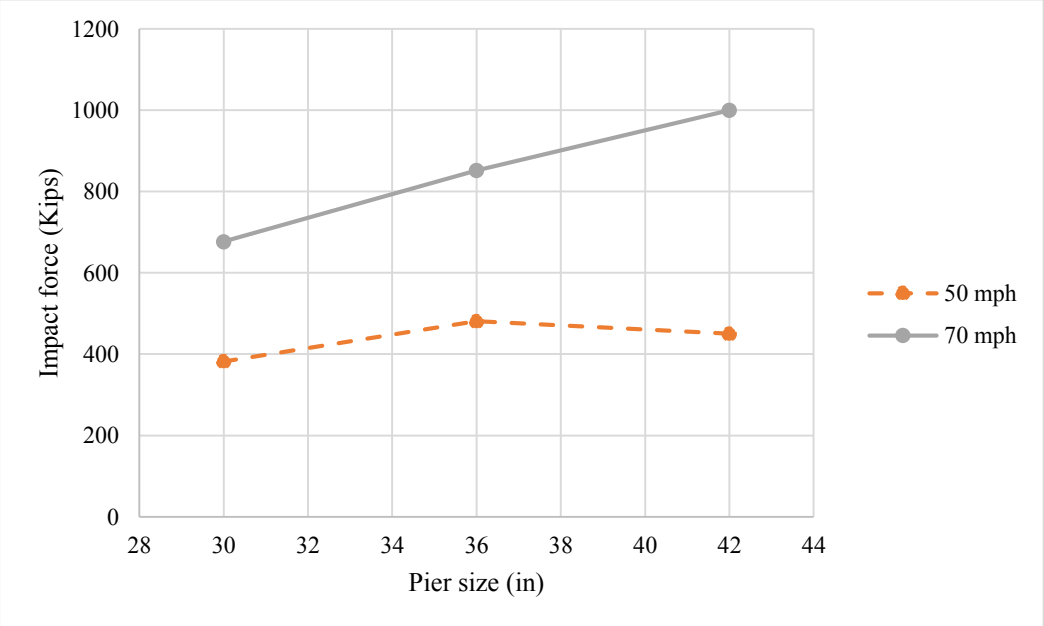

Figure 105. Graph. F5 versus pier size for M40.

The effect of pier size on T1 to T5 are illustrated from figure 106 to figure 109. The pier size varies from 30 in to 42 in. Truck velocity of 30 mph, 50 mph, and 70 mph are considered. The weight of the truck is selected as 40 T. For T1, T2, and T3, the impact time is almost constant when pier size varies. For T4, the transition time between the engine impact and trailer impact decreases when the pier size increases. For T5, the trailer impact time varies a lot when the pier size changes. This is because the impact process is complex and the trailer impact time in the simulations is affected by many other factors, which might not be directly related to the pier size. Thus, 0.22 sec is used as an approximation.

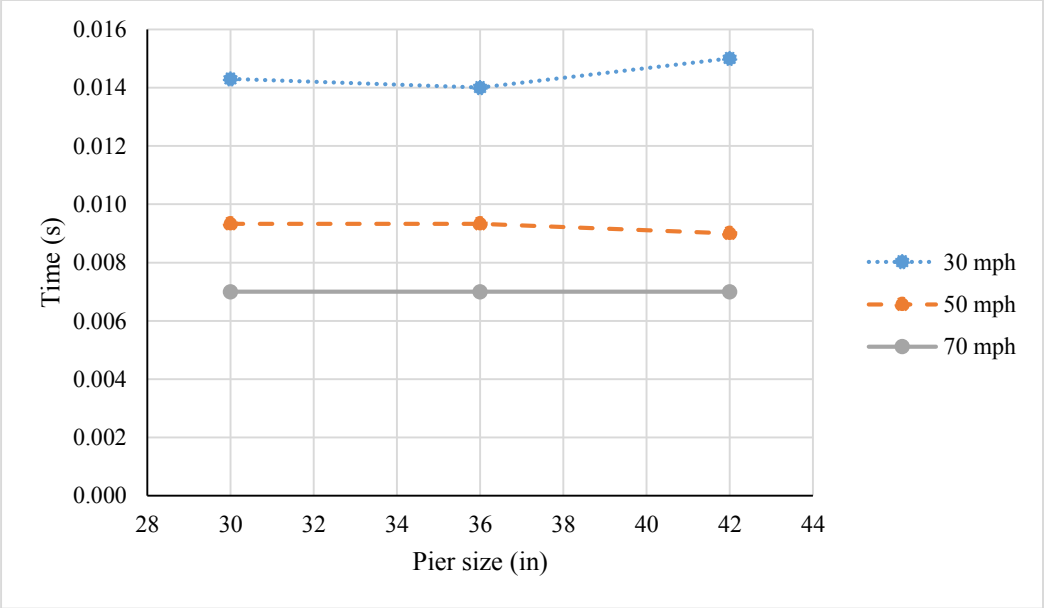

Figure 106. Graph. T1 versus pier size for M40.

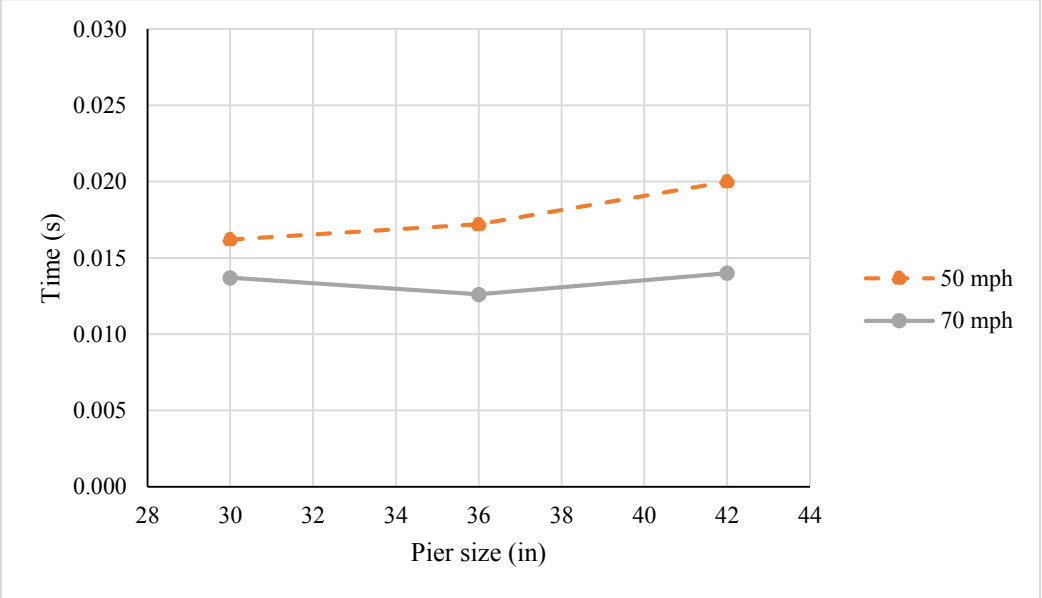

Figure 107. Graph. T2 versus pier size for M40.

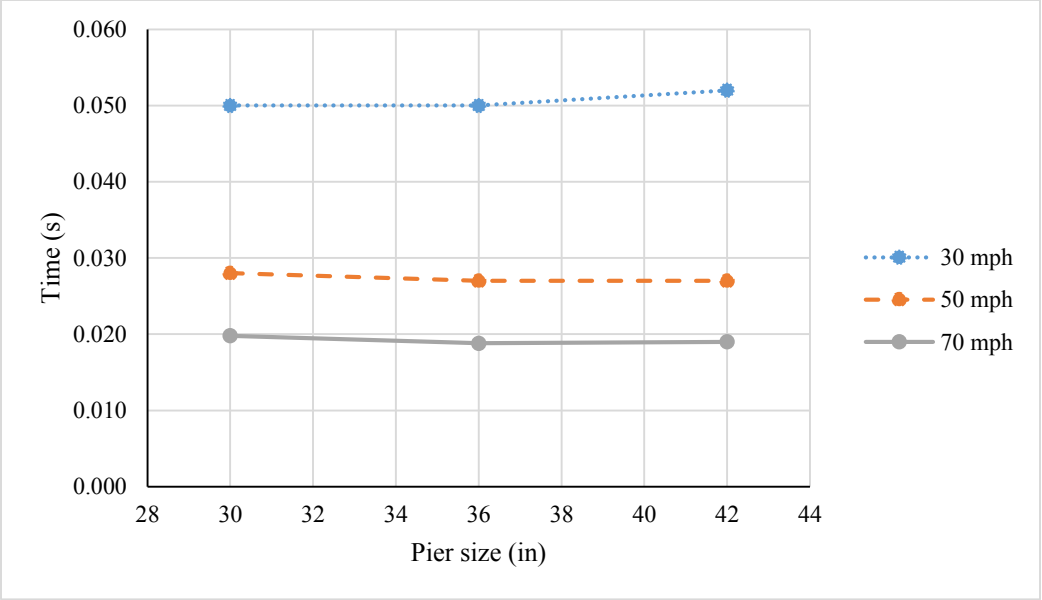

Figure 108. Graph. T3 versus pier size for M40.

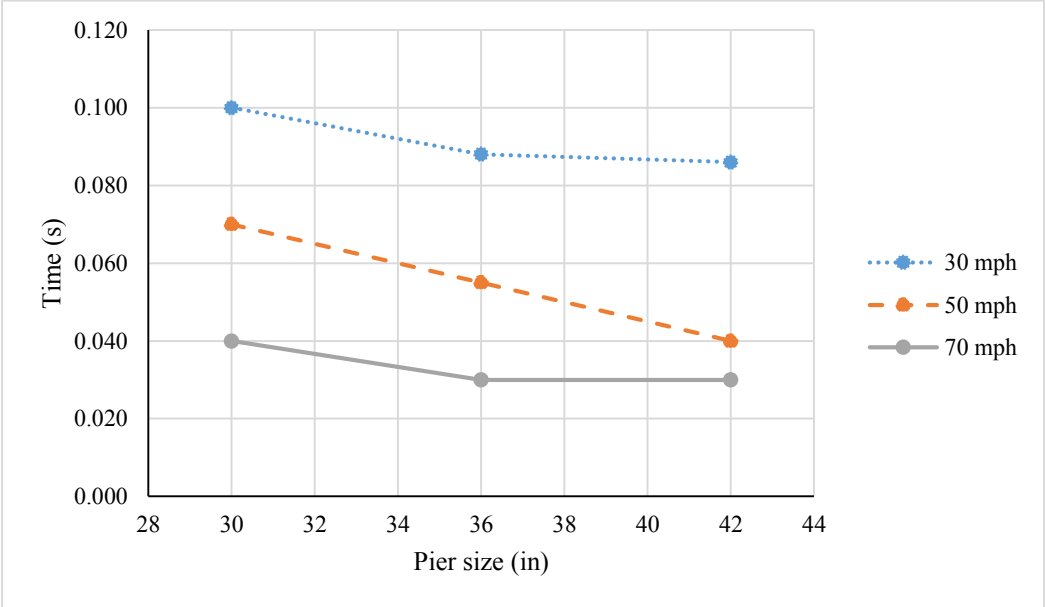

Figure 109. Graph. T4 versus pier size for M40.

Effect of truck weight

The effects of truck weight on F1 to F5 are illustrated from figure 110 to figure 114. The weight of the truck varies from 20 T to 40 T. The pier size is 36 in. Truck velocities of 30 mph, 50 mph, and 70 mph are considered. For F1 to F4, the impact forces are almost constant when the truck weight changes. This is because the truck weight is changed by changing the density of the cargo, while the F1 to F4 occur before the cargo impact. For F5, the trailer impact force increases as the cargo weight increases. Since truck traveling at 30 mph will not generate trailer impact, the results of F5 from 60-mph impact are plotted for illustration.

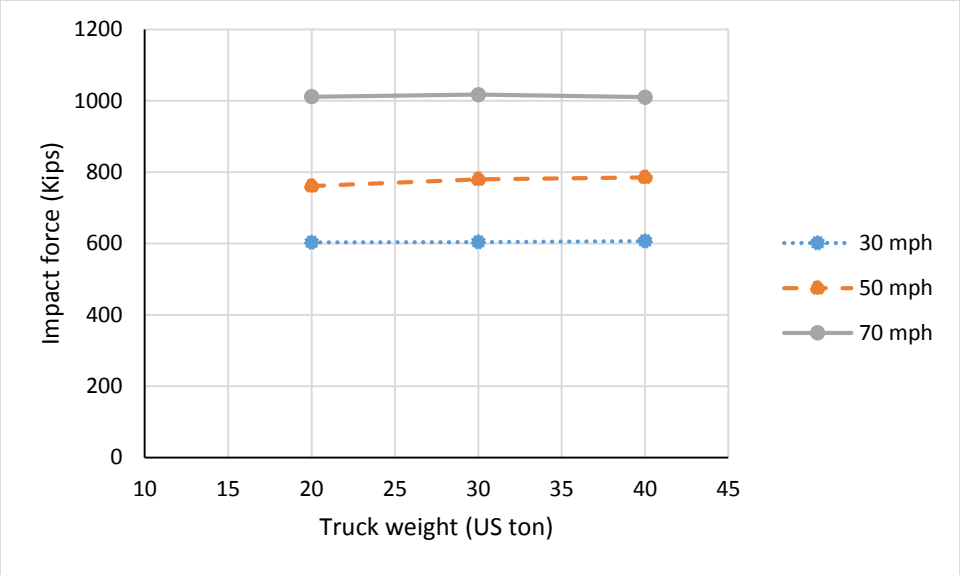

Figure 110. Graph. F1 versus truck weight for P3.

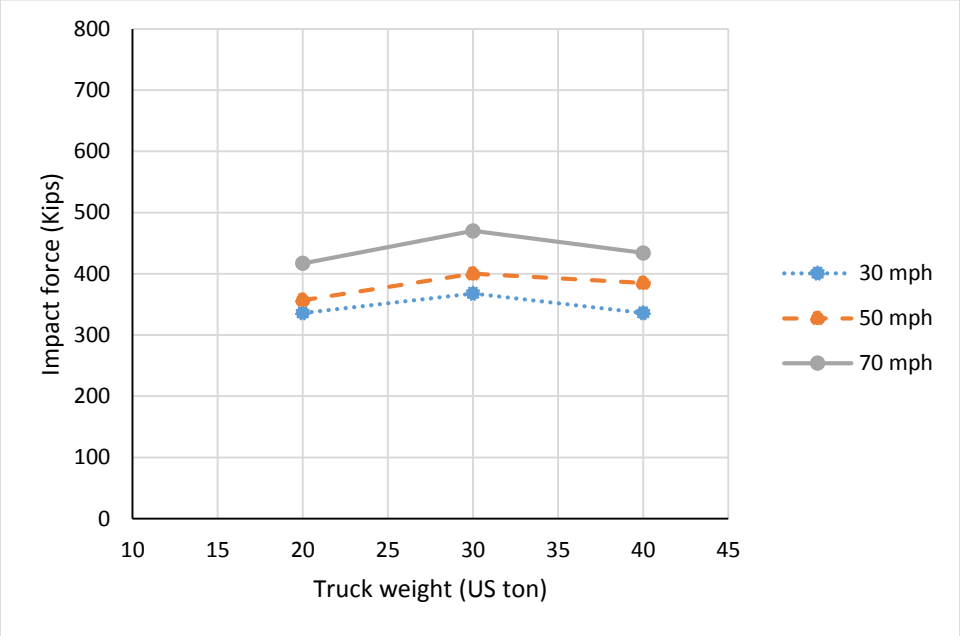

Figure 111. Graph. F2 versus truck weight for P3.

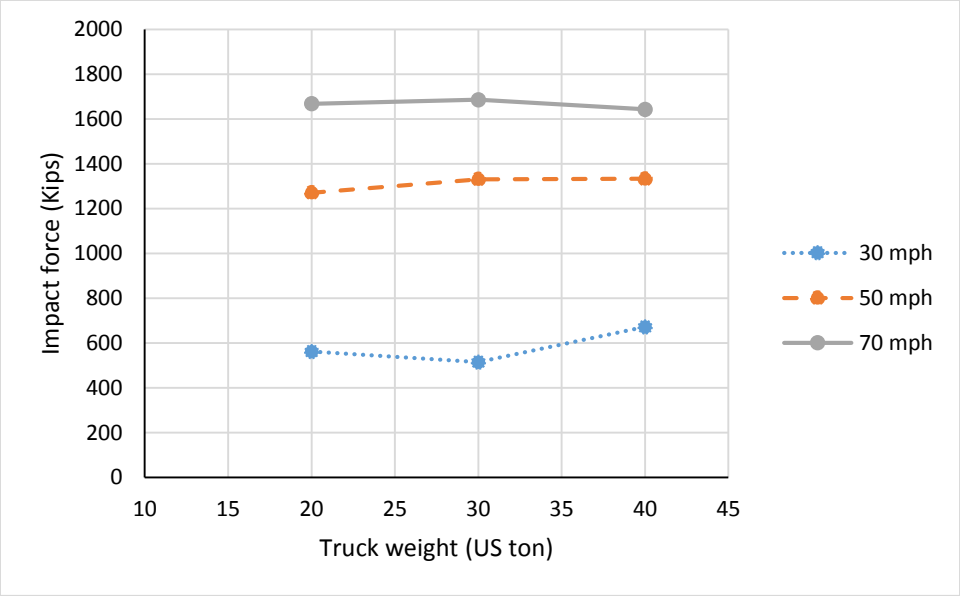

Figure 112. Graph. F3 versus truck weight for P3.

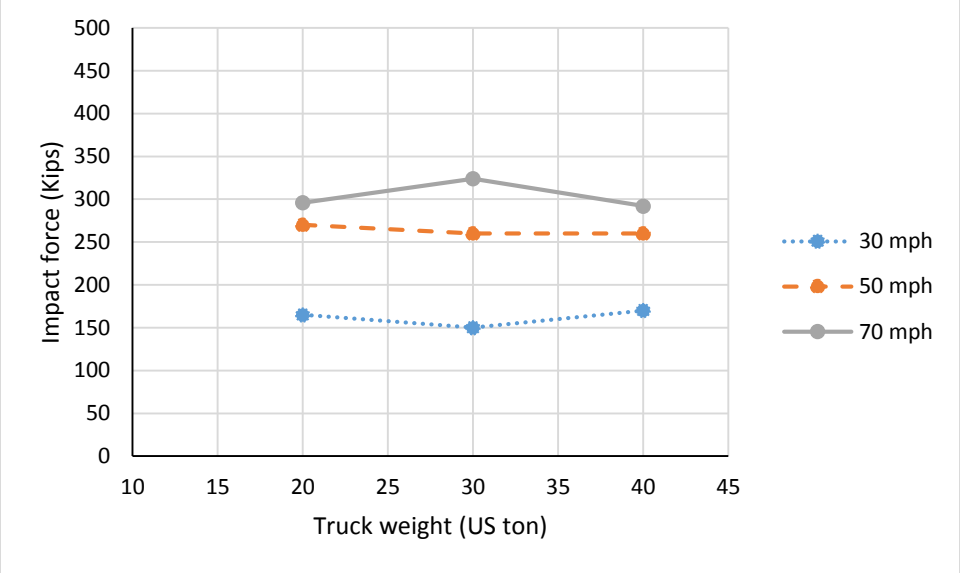

Figure 113. Graph. F4 versus truck weight for P3.

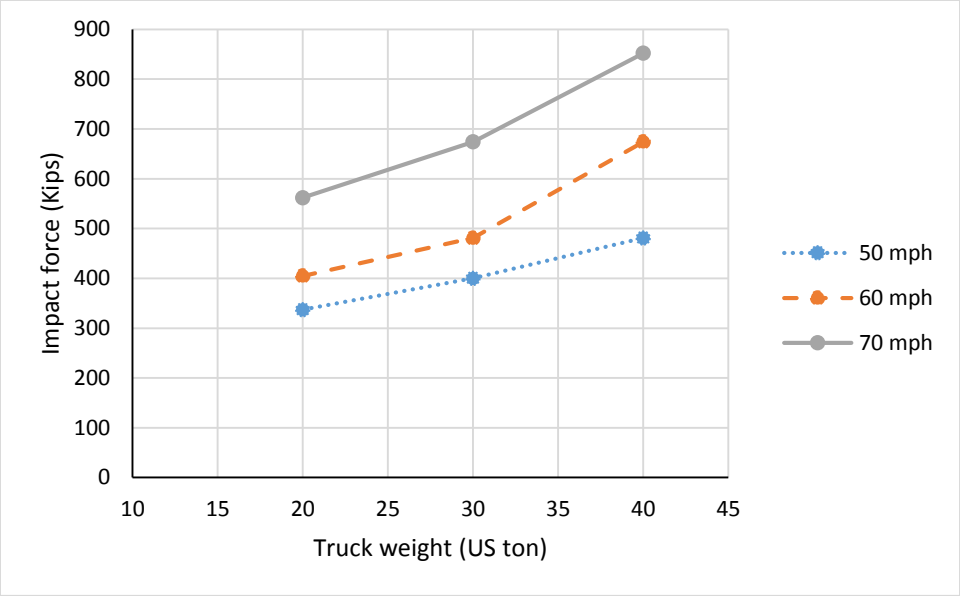

Figure 114. Graph. F5 versus truck weight for P3.

The effects of truck weight on T1 to T4 are illustrated from figure 115 to figure 118. Similar to impact forces, the impact time T1 to T4 are almost constant when truck weight changes.

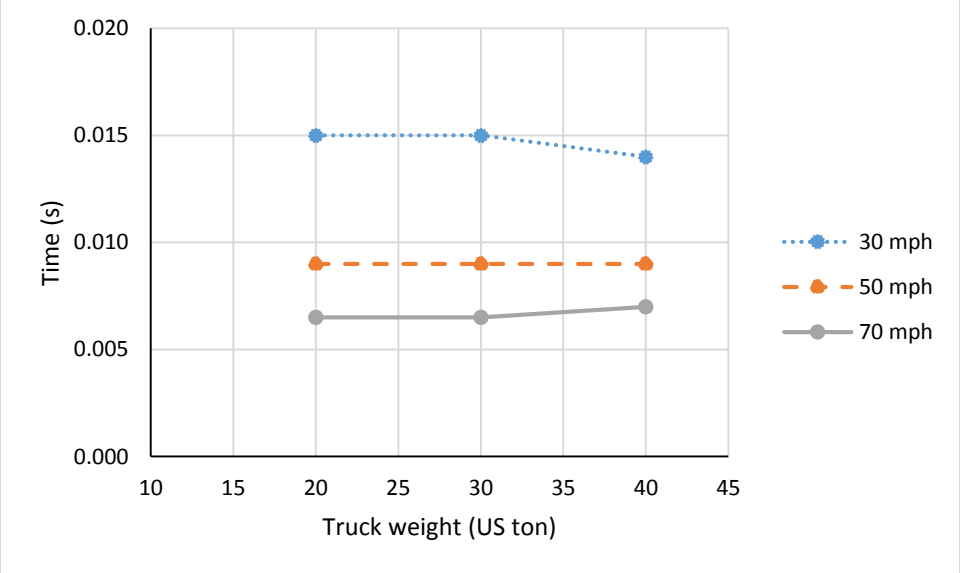

Figure 115. Graph. T1 versus truck weight for P3.

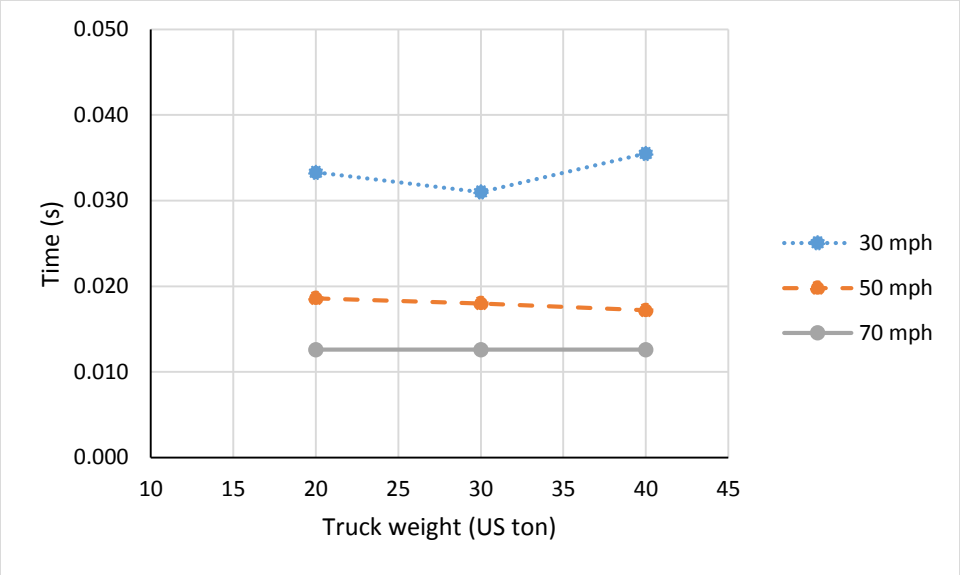

Figure 116. Graph. T2 versus truck weight for P3.

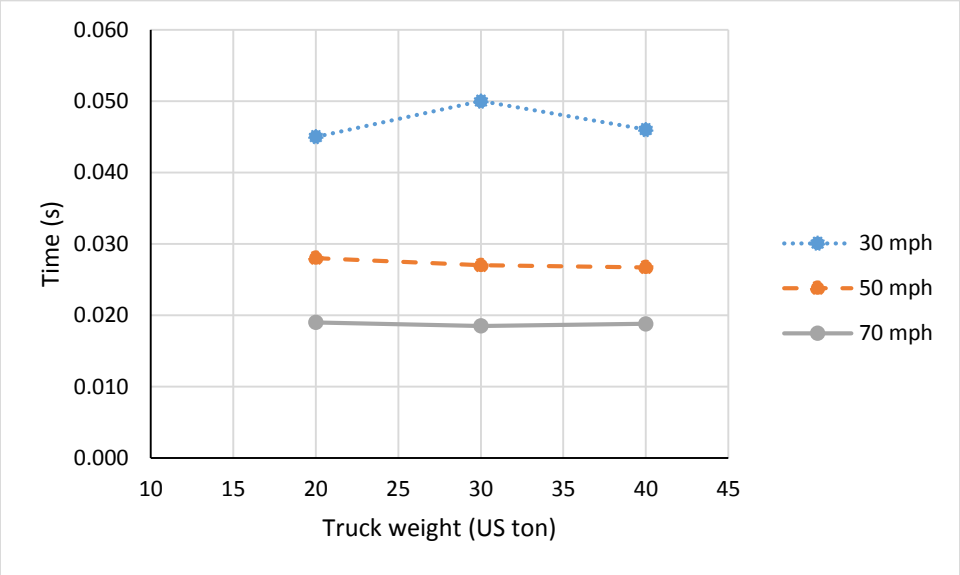

Figure 117. Graph. T3 versus truck weight for P3.

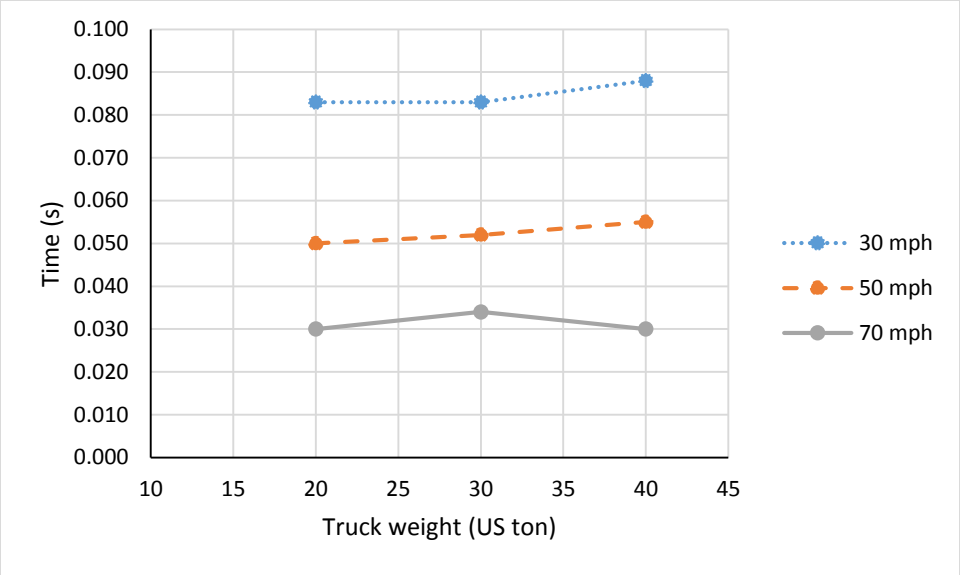

Figure 118. Graph. T4 versus truck weight for P3.

Determination of Pulse Parameters

As indicated in AASHTO (2012), the impact load on a bridge structure during a ship collision is complex and depends on many factors including structural type and shape of the ship's bow, degree of water ballast carried in the forepeak of the bow, size and velocity of the ship, geometry of the collision, and geometry and strength characteristics of the pier. The head-on ship collision impact force on a pier is expressed as,

$$P_s = 8.15V\sqrt{DWT} \tag{7}$$

where P_s is equivalent static vessel impact force (kips), DWT is the deadweight tonnage of the vessel (tons) and V is the vessel impact velocity (ft/sec).

As illustrated in figure 87, the parameters that need to be determined for the proposed pulse model are F_1 to F_5 and T_1 to T_5. Based on a parametric study of vehicular impact forces on bridge piers, truck weight (W), initial truck velocity (V), and pier size (P) have been identified as variables affecting the impact force pulses on bridge piers. Hence, the format for equations for peak forces F_1 to F_5 in the proposed triangular impact force time history is adopted from that in AASHTO (2012) for vessel collisions,

$$F_i = f\left\{\alpha(W)^{\beta}(V)^{\gamma}\left(\frac{b}{36}\right)^{\varepsilon}\right\} \tag{8}$$

where, F_i, i = 1, ..5 are peak forces (kips). In the equation (8), γ ,β ,α and εare regression parameters, W is the truck weight (US ton), V is the truck impact velocity (mph) and b is the pier width (in).

Equations of the form in equation (8) have been derived for peak forces, where F_i, i = 1, ..5, is the impact force time history derived through nonlinear optimization performed in MATLAB. Similarly, time instants T_1 to T_5 have also been derived through nonlinear regression. The data for regression are based on 45 truck simulation cases, which includes three different weights of the truck (20, 30, and 40 T), five different impact speeds (30, 40, 50, 60, and 70 mph), and 3 different rectangular pier sizes (30 in, 36 in, and 42 in). It should be noted that the piers with

24x24 in section are not considered since they are completely destroyed at impacts speeds as low as 50 mph. Equations for pulse parameters F_1 to F_5 and T_1 to T_5 are obtained as follows:

$$F_1(kips) = 109\,V^{0.52}\left(\frac{b}{36}\right)^{0.33} \quad (9)$$

$$F_2(kips) = 52\,V^{0.51}\left(\frac{b}{36}\right)^{-0.84} \quad (10)$$

$$F_3(kips) = 30\,V^{0.95} \quad (11)$$

$$F_4(kips) = 3\,V^{1.08}\left(\frac{b}{36}\right)^{-0.75} \quad (12)$$

$$F_5(kips) = 0.05\,V^{1.77}W^{0.61}\left(\frac{b}{36}\right)^{1.14} \quad (13)$$

$$T_1(s) = 0.27\,V^{-0.86} \quad (14)$$

$$T_2(s) = 1.49\,V^{-1.09}\left(\frac{b}{36}\right)^{0.64} \quad (15)$$

$$T_3(s) = 1.04\,V^{-0.93} \quad (16)$$

$$T_4(s) = 2.96\,V^{-1.05}\left(\frac{b}{36}\right)^{-1.21} \quad (17)$$

$$T_5(s) = 0.22 \quad (18)$$

Table 9 shows comparisons between impact forces corresponding to three peaks in the impact force time-history based on the finite element simulation and equations (9) to (13). These comparisons are also shown in figure 119 and figure 121. Considering the complexity of the vehicular impact process on bridge piers and the simplicity of the proposed design equations for the design of bridge piers against vehicular impacts, the estimated results match the simulated results reasonably well.

It should be noted that the idea of regression is to achieve the minimum error between an actual and corresponding estimated value. Therefore, equation (9) through (18) represent "average" or "middle" values for the demand. There was no attempt to develop envelopes for the maximum effects because that would lead to highly conservative design equations. The variability associated with equations (9) through (18) and uncertainty in their application to a design process can eventually be taken into account through the regular probabilistic design methods embedded in current codes and specifications.

Another important note is that equations (9) through (18) were derived using a single type of truck. For the truck used herein, the weight of the bumper is 0.10 ton and the weight of the engine is 1.43 ton. The weight of the truck is changed by varying only the weight of the cargo, meaning that the weight of the bumper and engine are assumed constant in all the equations. In addition, equations (9) through (12) do not incorporate bumper or engine weights even though the equations directly represent the effect of the bumper and engine. Therefore, in order to generalize equations (9) through (18), additional studies should be conducted with a variety of truck designs to confirm that they are reasonably representative of the heavy tractor semi-trailer truck population in the US.

Table 8. Standard error of parameters of equations for impact forces.

	Parameter	Standard error
Equation (9)	109.00	27.99
	0.52	0.04
	0.33	0.07
Equation (10)	52.00	25.66
	0.51	0.07
	-0.84	0.12
Equation (11)	30.00	9.08
	0.95	0.08
Equation (12)	3.00	4.64
	1.08	0.24
	-0.75	0.35
Equation (13)	0.05	0.03
	1.77	0.10
	0.61	0.07
	1.14	0.14
Equation (14)	0.27	0.02
	-0.86	0.02
Equation (15)	1.49	0.18
	-1.09	0.18
	0.64	0.30
Equation (16)	1.04	0.53
	-0.93	0.13
Equation (17)	2.96	3.00
	-1.05	0.09
	-1.21	0.30

Table 9. Comparison between simulation and regression based equations.

RUNS	F1-FEM (kips)	F1-Equation (kips)	F2-FEM (kips)	F2-Equation (kips)	F3-FEM (kips)	F3-Equation (kips)	F4-FEM (kips)	F4-Equation (kips)	F5-FEM (kips)	F5-Equation (kips)
P2_V30_W40	643	593	323	343	652	753	171	138	168	156
P2_V40_W40	690	688	355	398	971	990	191	189	247	259
P2_V50_W40	809	772	486	446	1200	1224	206	241	382	384
P2_V60_W40	877	848	504	489	1394	1456	191	293	546	530
P2_V70_W40	926	918	576	529	1657	1686	337	346	677	696
P2_V30_W30	647	593	330	343	562	753	160	138	112	131
P2_V40_W30	688	688	414	398	980	990	200	189	225	217
P2_V50_W30	809	772	400	446	1248	1224	270	241	337	323
P2_V60_W30	868	848	483	489	1416	1456	266	293	450	445
P2_V70_W30	922	918	579	529	1596	1686	341	346	585	585
P2_V30_W20	652	593	318	343	674	753	140	138	90	102
P2_V40_W20	683	688	420	398	845	990	134	189	174	170
P2_V50_W20	780	772	481	446	1290	1224	264	241	270	252
P2_V60_W20	899	848	476	489	1461	1456	312	293	337	348
P2_V70_W20	922	918	581	529	1619	1686	328	346	450	457
P3_V30_W40	607	630	319	294	681	753	172	121	247	192
P3_V40_W40	683	731	333	341	931	990	252	165	371	319
P3_V50_W40	776	820	384	382	1349	1224	250	210	481	473
P3_V60_W40	899	900	393	419	1461	1456	236	256	674	653
P3_V70_W40	1012	975	434	454	1664	1686	290	302	771	858
P3_V30_W30	576	630	368	294	605	753	150	121	168	161
P3_V40_W30	680	731	320	341	924	990	173	165	225	268
P3_V50_W30	751	820	400	382	1303	1224	260	210	463	397
P3_V60_W30	900	900	390	419	1461	1456	273	256	480	548
P3_V70_W30	1011	975	486	454	1479	1686	324	302	674	720
P3_V30_W20	600	630	336	294	580	753	165	121	112	126
P3_V40_W20	682	731	352	341	880	990	200	165	135	209
P3_V50_W20	771	820	357	382	1281	1224	170	210	337	310
P3_V60_W20	920	900	390	419	1439	1456	191	256	405	429
P3_V70_W20	1009	975	417	454	1660	1686	296	302	562	563
P4_V30_W40	623	663	337	258	630	753	130	108	263	229
P4_V40_W40	674	769	388	299	1169	990	219	147	337	380
P4_V50_W40	809	863	449	335	1364	1224	230	187	450	564
P4_V60_W40	928	947	519	368	1500	1456	300	228	773	779
P4_V70_W40	1012	1026	472	399	1600	1686	300	270	1012	1023
P4_V30_W30	623	663	286	258	607	753	145	108	225	192
P4_V40_W30	647	769	387	299	1056	990	200	147	315	319

Table 9. Comparison between simulation and regression based equations (continued).

RUNS	F1-FEM (kips)	F1-Equation (kips)	F2-FEM (kips)	F2-Equation (kips)	F3-FEM (kips)	F3-Equation (kips)	F4-FEM (kips)	F4-Equation (kips)	F5-FEM (kips)	F5-Equation (kips)
P4_V50_W30	809	863	470	335	1348	1224	240	187	450	474
P4_V60_W30	931	947	525	368	1430	1456	305	228	757	654
P4_V70_W30	1012	1026	470	399	1596	1686	211	270	899	859
P4_V30_W20	623	663	310	258	540	753	137	108	112	150
P4_V40_W20	647	769	400	299	1166	990	200	147	225	250
P4_V50_W20	809	863	470	335	1281	1224	200	187	234	370
P4_V60_W20	900	947	490	368	1484	1456	180	228	600	511
P4_V70_W20	1012	1026	640	399	1506	1686	311	270	787	671
FEM/Equation (average)	0.98		1.10		0.97		1.06		1.00	

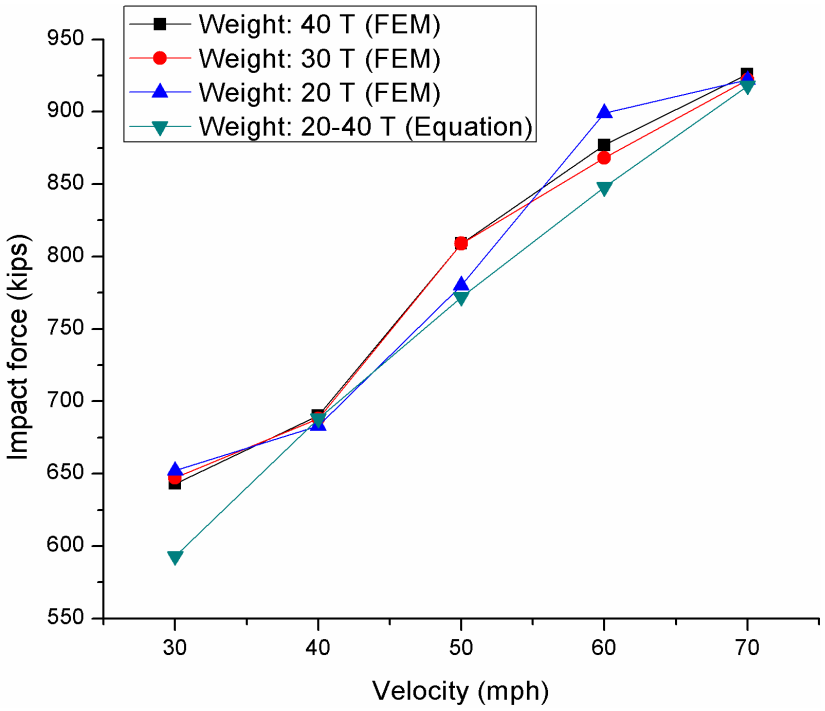

(a) 30-in pier.

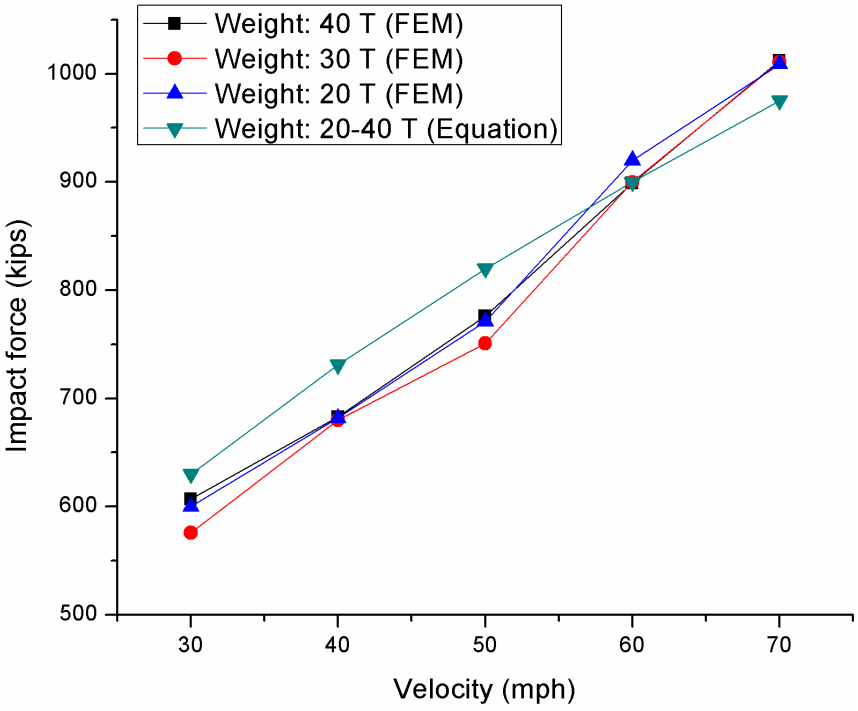

(b) 36-in pier.

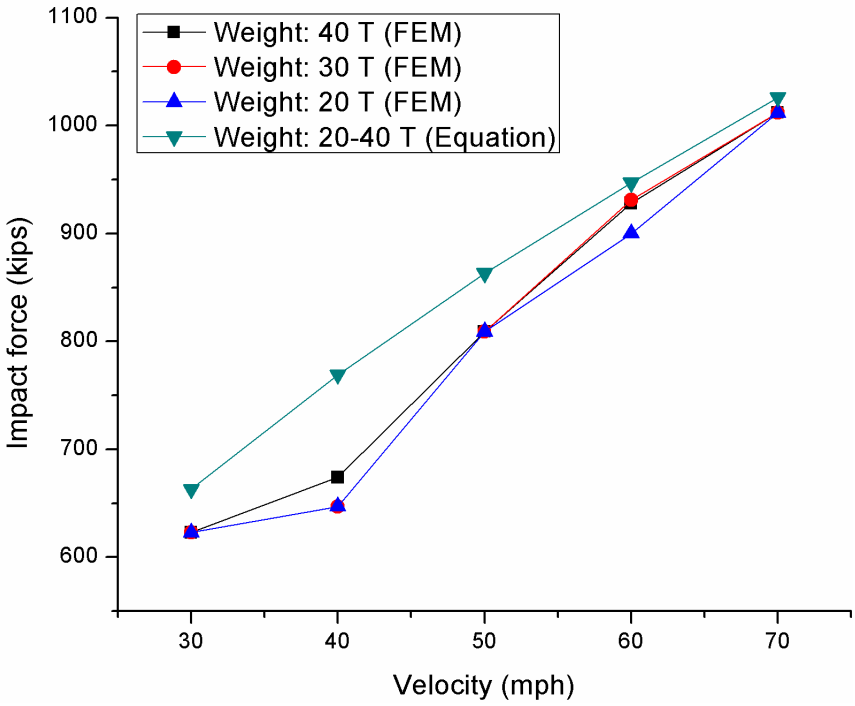

(c) 42-in pier.

Figure 119. Graphs. F1 from FEM and equation.

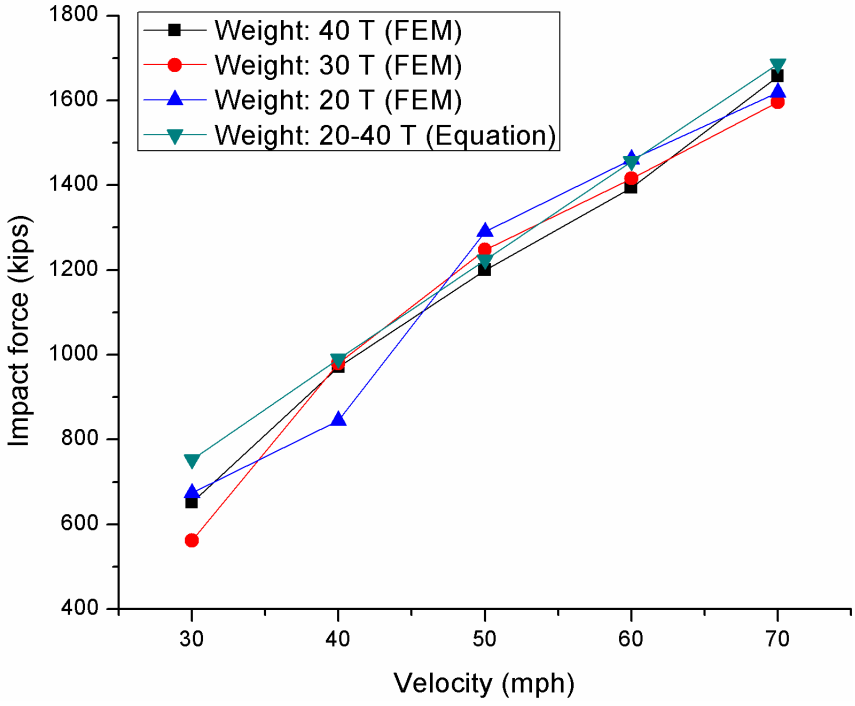

(a) 30-inch pier.

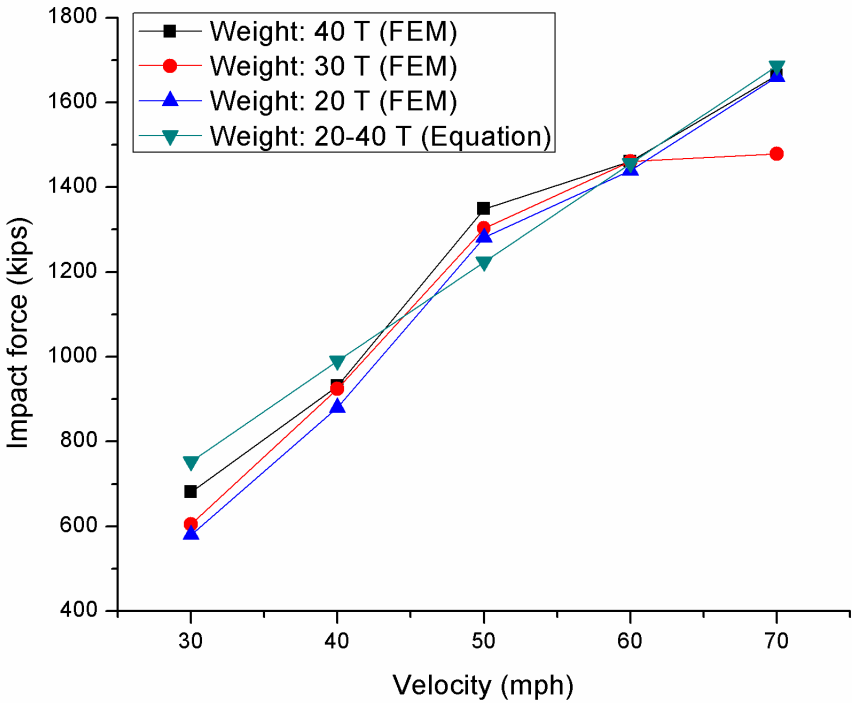

(b) 36-inch pier.

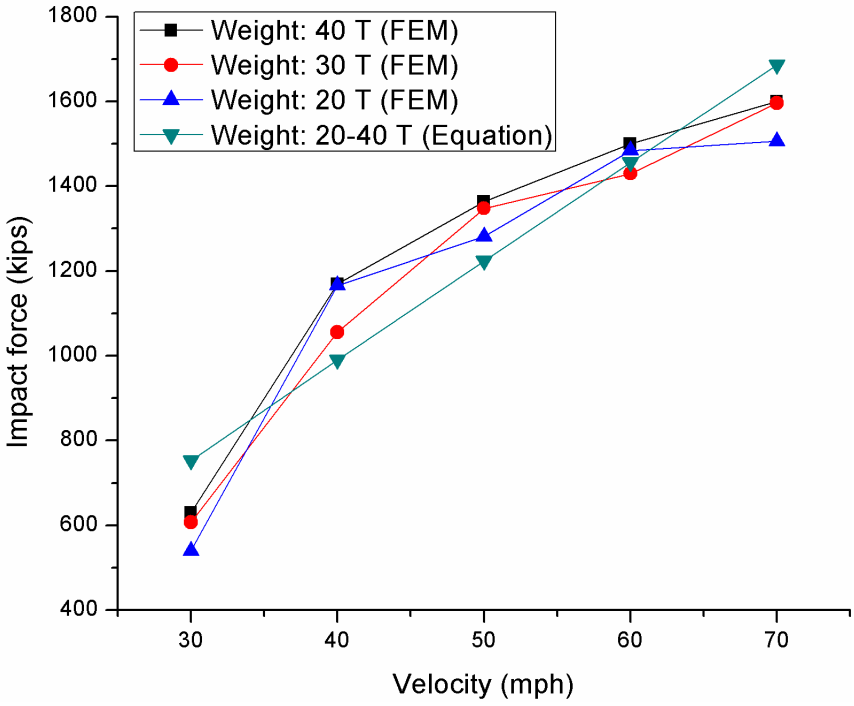

(c) 42-inch pier.

Figure 120. Graphs. F3 from FEM and equation.

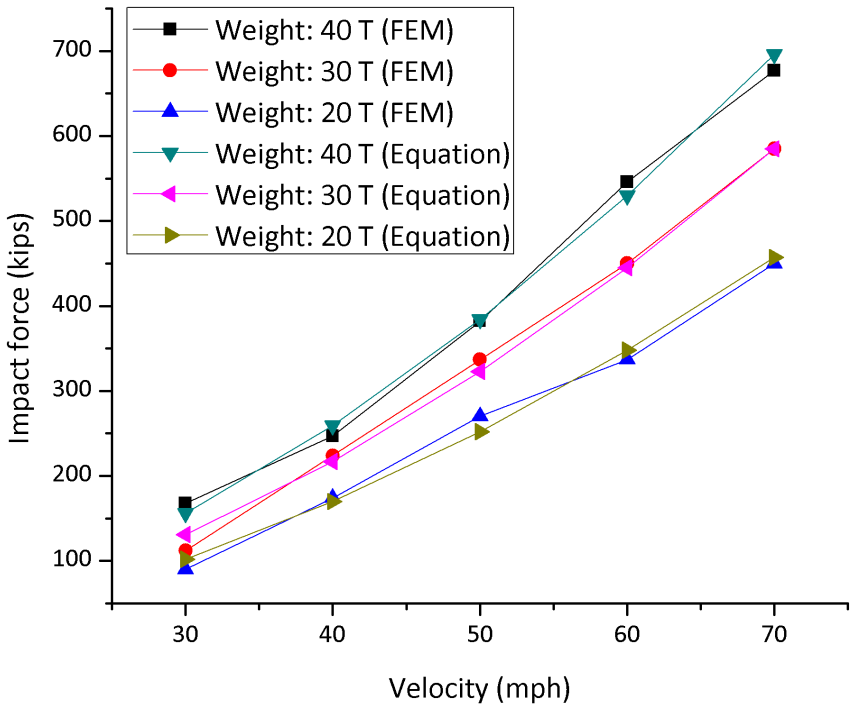

(a) 30-in pier.

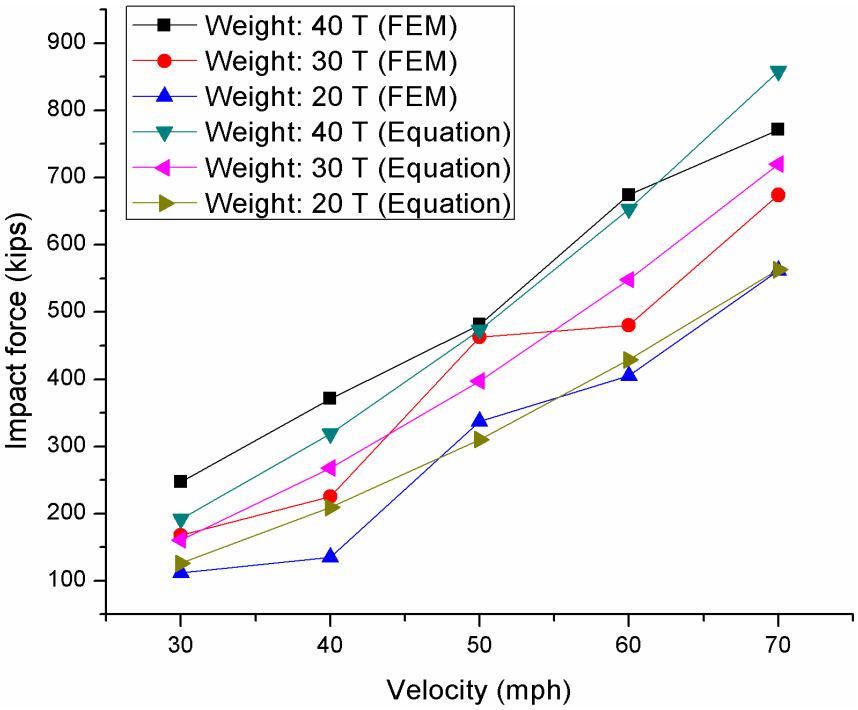

(b) 36-in pier.

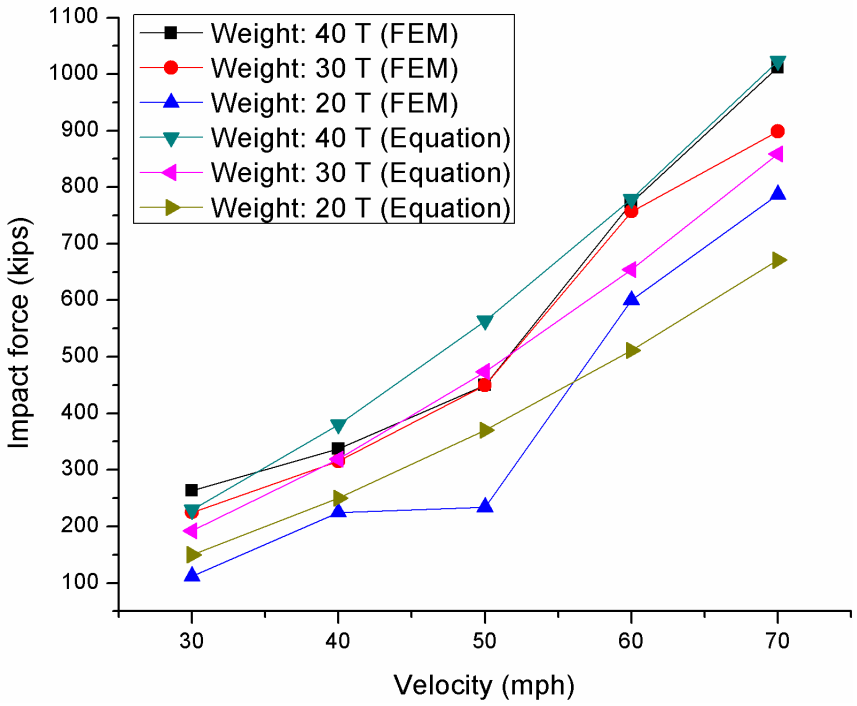

(c) 42-in pier.

Figure 121. Graphs. F5 from FEM and equation.

In order to investigate the suitability of the proposed pulse model in representing vehicular impact on bridge piers, the proposed pulse model has been applied as a pressure to the pier model in LS-DYNA as described earlier. Typical cases selected for illustration include 30 in and 36 in pier sizes, 50 and 60 mph impact velocities and 20 T and 30 T truck weights. Figure 122 and figure 123 show deformed modes and peak deformation of piers subject to truck loading (denoted as truck simulation) and impact loading by the proposed pulse model (denoted as pulse simulation). A close examination of the figure 122 shows that the general deformed shapes as well as the general mode of failure for the truck and pulse simulations match well. Most importantly, full collapse behavior is modeled correctly, as shown in figure 122 (c) and (f).

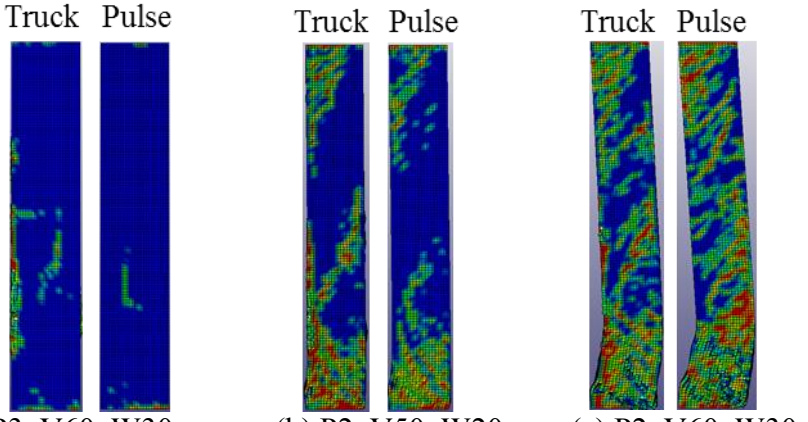

(a) P3_V60_W30. (b) P2_V50_W20. (c) P2_V60_W30.

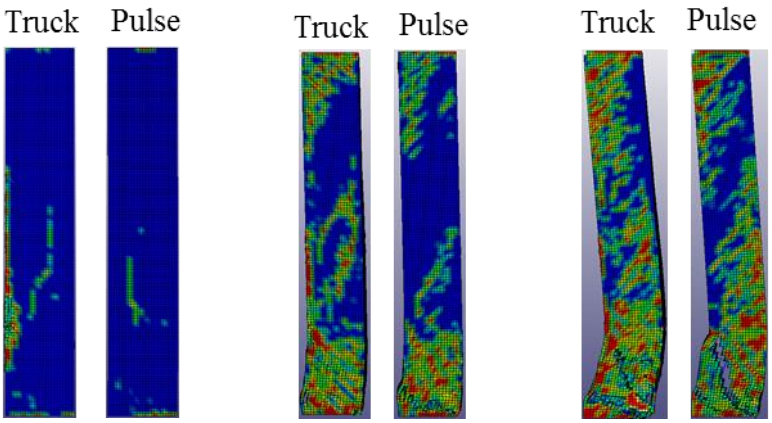

(d) P3_V60_W20. (e) P2_V50_W30. (f) P2_V70_W30.

Figure 122. Illustration. Damages to piers subjected to impact loading by truck and pulse model.

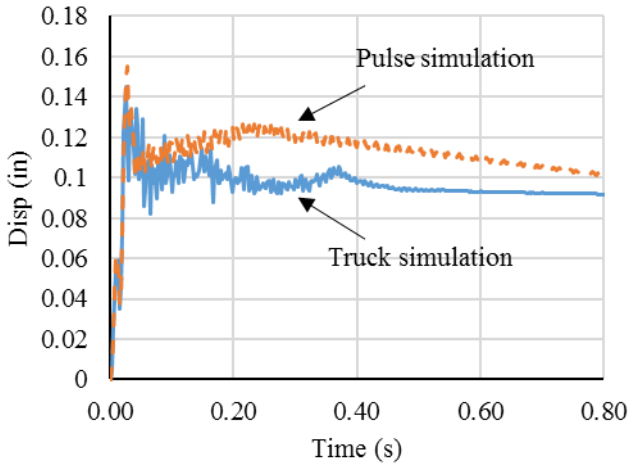

(a) Minor damage: P3_V60_W30.

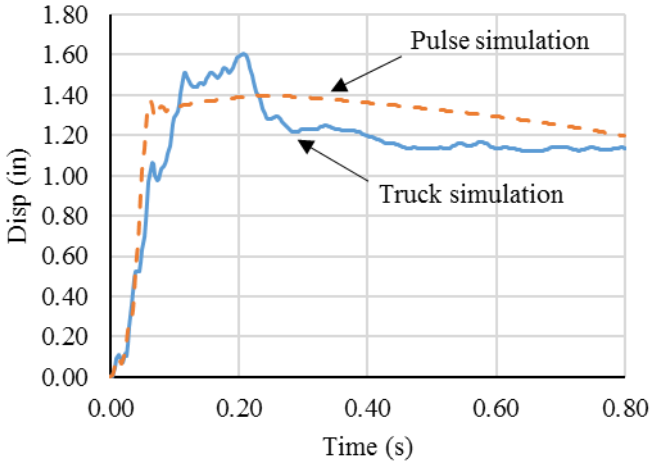

(b) Moderate damage: P2_V50_W20.

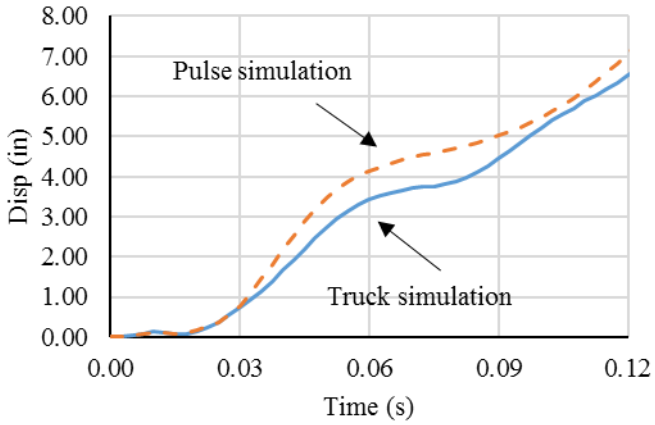

(c) Severe damage: P2_V60_W30.

Figure 123. Graph. Displacement time histories for the pier for truck and pulse simulations.

Circular Pier

The pulse model presented above for rectangular piers could also be applied to circular piers by changing the distribution of the loading around the pier. For a rectangular pier, the pulse is applied across the width of the pier (on a strip). However, when the truck impacts the circular pier, only part of the pier width will be in contact with the truck. Thus, the proposed pulse model is only applied to a part of the pier width with a non-uniform stress distribution.

Based on numerical simulation and calibration, a reasonable distribution of the forces along the surface is shown in figure 124. The impact forces are applied horizontally at the nodes of the pier. It is observed from the illustration in figure 124(a), that the loads are applied on 25% of the perimeter. The magnitude of the force decreases from the center to the edge of the pier. The detailed distribution of the forces along the contact area is shown in figure 124(b). Heights for the application of the loading is the same as those for the rectangular pier in figure 89.

To validate the pulse model for the circular pier, original pulse simulations are compared with results obtained from truck simulations, as shown in figure 125. It is observed that the damage modes of piers for the two cases match very well. This is also observed from displacement time histories for the original pulse and truck simulations for three cases of minor, moderate and severe damages in figure 126.

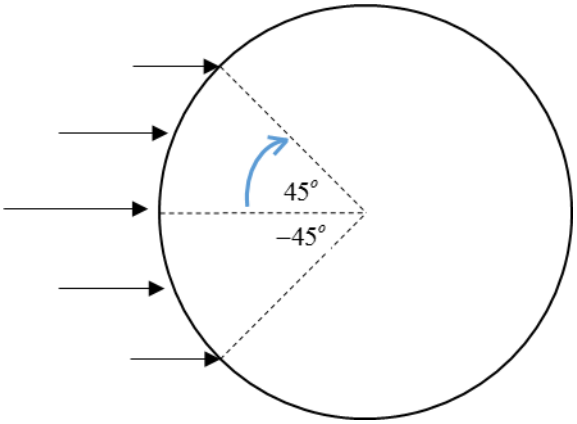

(a). Distribution of nodal forces around the surface of the pier.

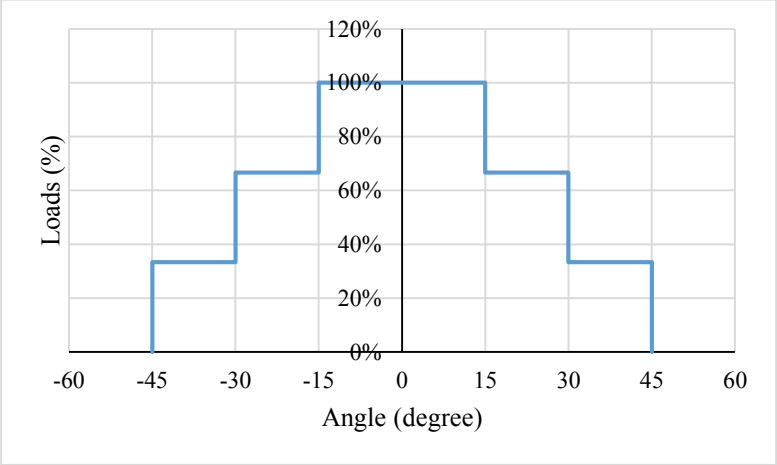

(b). Distribution of forces magnitude against the angle.

Figure 124. Illustration. Distribution of impact force pulse around the diameter of a circular pier.

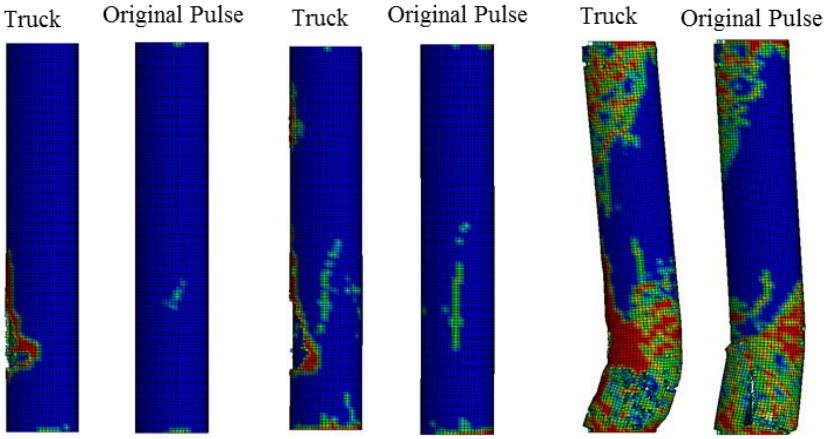

(a) P6_V30_W40. (b) P6_V50_W40. (c) P6_V70_W40.

Figure 125. Illustration. Damage modes for the circular pier based on truck simulation and original pulse simulation.

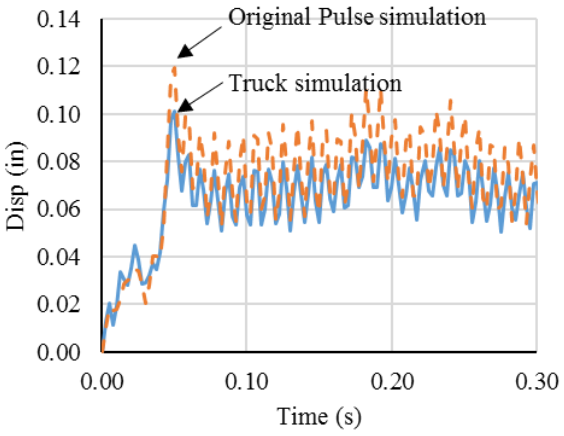

(a) P6_V30_W40.

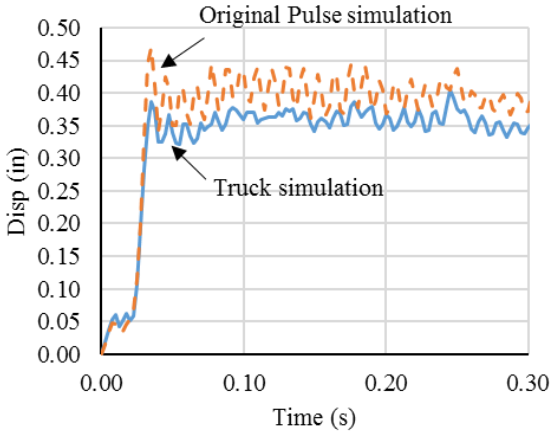

(b) P6_V50_W40.

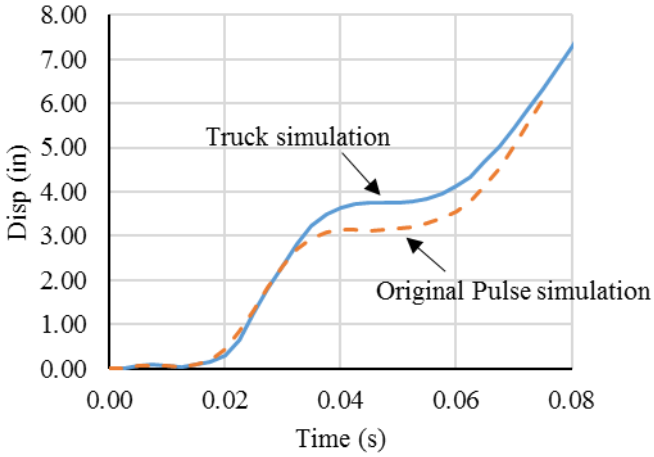

(c) P6_V70_W40.

Figure 126. Graph. Displacement time-histories for the original pulse and truck simulations for three cases of minor, moderate and severe damages to circular piers.

Figure 127 shows a comparison between the deformed shape of circular piers for pulse and truck simulations. Cases in figure 127 include 30 in and 36 in circular piers and 40 T truck traveling with impact speeds in the range of 30 to 70 mph. It is observed from figure 127 that the damage modes for truck and pulse impacts for circular piers match very well.

Figure 128 shows displacement time-histories at the point of impact for a 40 ton truck impacting a 36-in piers at impacts velocities varying from 30 mph and 70 mph. It is observed that displacement time histories for pulse and truck simulation match very well for circular piers. Also, a representative force-deformation plot for case P6_V70_W40 is shown in figure 129 for the understanding of readers.

Figure 128(d) shows a case where the pier collapses and the discrepancy between pulse simulation and truck simulation is relatively small until the pier loses its capacity. The gap does grow after the pier fully collapses but the overall matching is considered to be acceptable,

considering that the difference is in millimeters. Overall deflection during vehicular impacts can be in several inches.

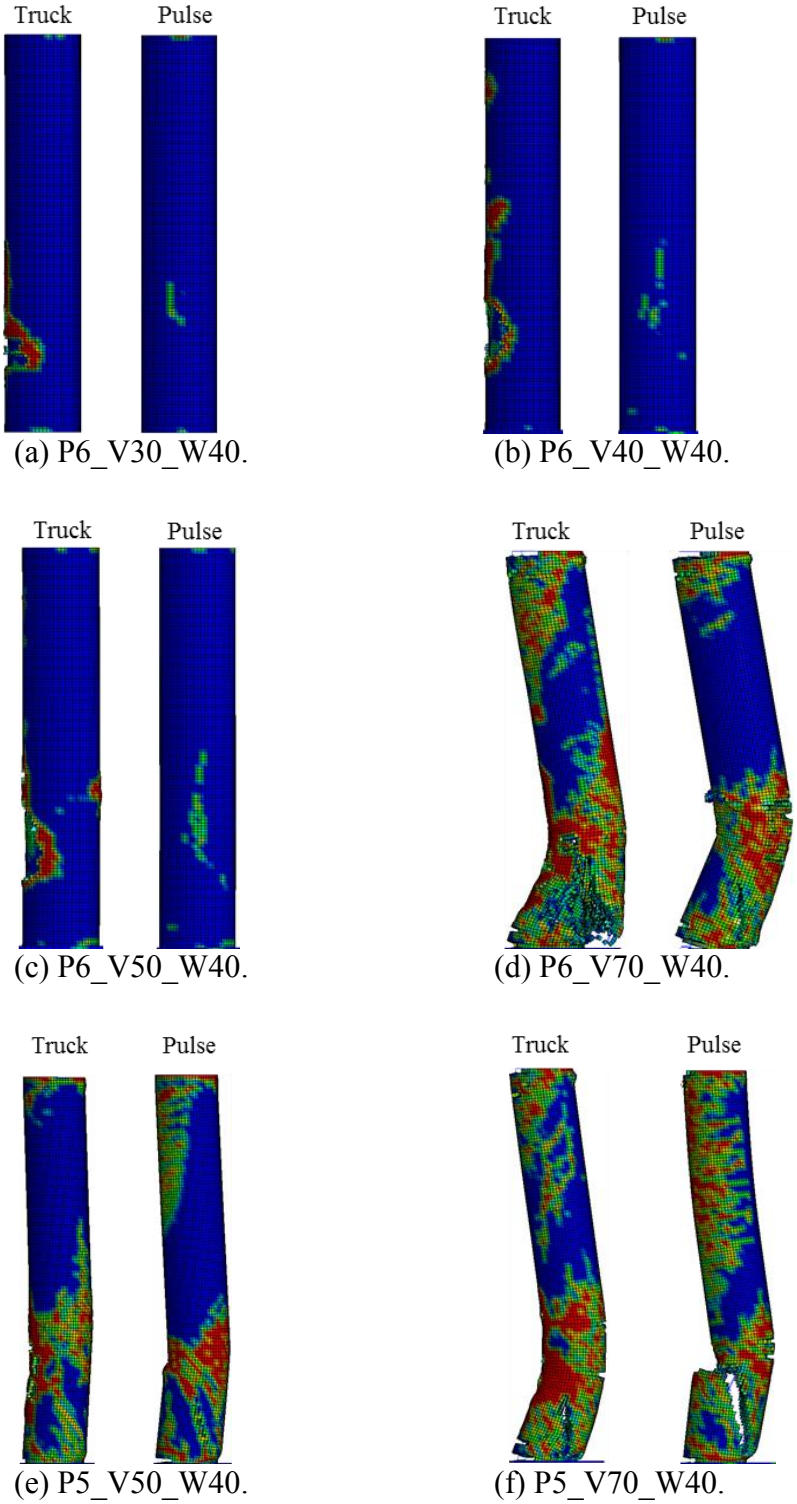

(a) P6_V30_W40. (b) P6_V40_W40.

(c) P6_V50_W40. (d) P6_V70_W40.

(e) P5_V50_W40. (f) P5_V70_W40.

Figure 127. Illustration. Damage modes using pulse and truck simulations for circular piers.

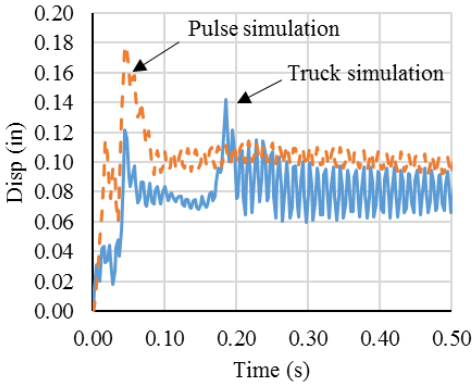

(a) P6_V30_W40.

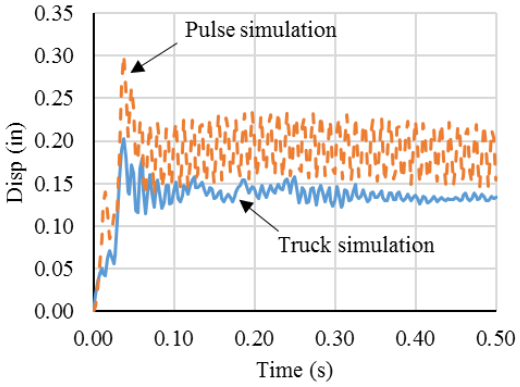

(b) P6_V40_W40.

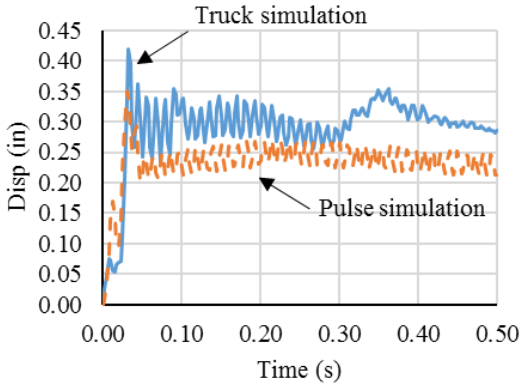

(c) P6_V50_W40.

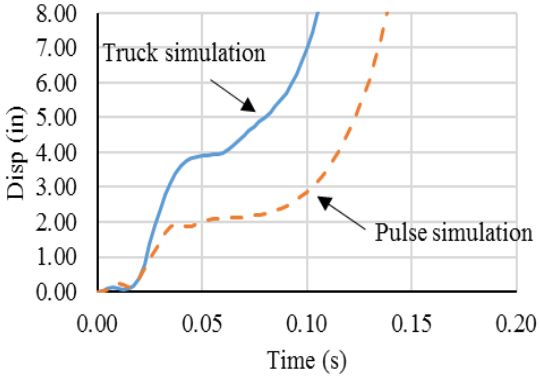

(d) P6_V70_W40.

Figure 128. Graphs. Displacement time histories for pulse and truck simulations for circular piers.

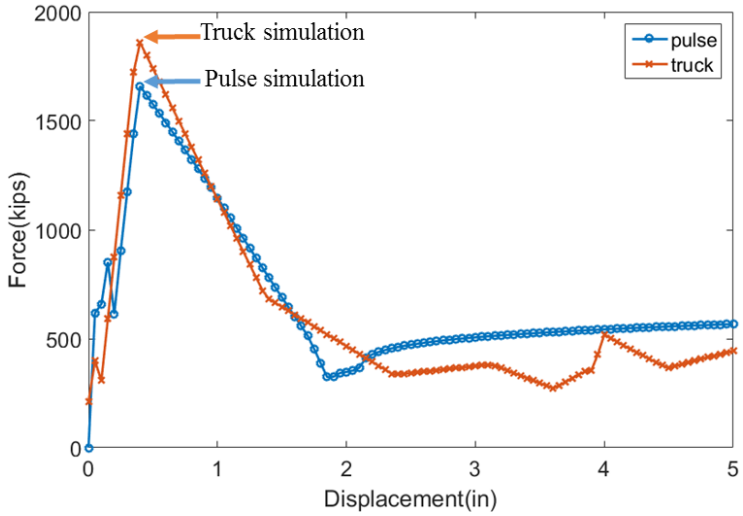

Figure 129. Graph. Force-displacement curves for pulse and truck simulations for P6_V70_W40.

CHAPTER 5. PERFORMANCE-BASED DESIGN FOR HEAVY VEHICLE SIMULATION

INTRODUCTION

One of the major developments in earthquake engineering over the past 2 decades has been the introduction and widespread use of performance-based design (PBD). In essence, performance-based design philosophy entails estimation of seismic demands in the system and its components and checking to see if they exceed the capacity associated with a required performance objective for a given hazard intensity level. Commonly accepted performance levels are Immediate Occupancy (IO) and Collapse Prevention (CP). The intensity of ground shaking (the hazard level) is typically specified via the likelihood of a seismic event, e.g., a probability of exceedance of 2% in 50 years. Demand and capacity parameters are generally associated with local or system level forces and deformations.

While PBD concepts are now well established in earthquake engineering, there has been little progress in the application of PBD ideas to impact engineering, specifically truck impact with bridge piers. Sharma et al. (2012) developed a framework to estimate the shear force capacity and demand on an RC column subject to vehicle impact for different performance levels. The proposed procedure was used for the design of RC columns to meet a set of performance objectives for different vehicle impact scenarios. Liu (2012) proposed that the ratio of peak impact force to shear capacity of the pier can be viewed as a demand to capacity parameter for piers subjected to impact by a single unit truck. They noted that a pier with a demand to capacity ratio less than 2 suffers only minor damage, while that with a ratio greater than 5 suffers severe damage during truck impact. Piers with a ratio in between 2 and 5 suffer only moderate damage.

Sharma et al. (2012) and Liu (2012) studies do not explicitly model the dynamic nature of the impact problem, but rather seek to simplify it by making a number of assumptions about structural behavior. This chapter proposes a new and comprehensive performance-based design framework that addresses this drawback. In chapter 4, detailed finite element simulations have been conducted to develop a pulse model by which to model the dynamic demand imposed by a colliding truck. The simulation data is also used to calibrate the proposed framework, which is simple enough for design office use.

CAPACITY DESIGN OF BRIDGE PIERS

Many of the documented truck versus pier accidents appear to show that failure occurred due to excessive shear demands (see, for example, figure 132(b)). This is not surprising because: 1) the AASHTO-LRFD specification (AASHTO-LRFD 2012) for vehicular impacts does not have a design philosophy that mitigates shear failure, and 2) the impact point is usually close to the lower support, which leads to small moment demands coupled with large shear forces at that location. Shear failure is a brittle mode of behavior that engineers typically like to avoid in earthquake engineering through capacity design. Capacity design is the process whereby plastic hinge mechanisms are promoted by providing over strength in shear at critical locations. Plastic

hinging is a more ductile mechanism than shear failure and can lead to increased collapse resistance.

Designing a pier for impact using the capacity design process is not as straightforward as it is in the case of earthquake engineering because dynamic effects are much more pronounced. For example, a beam tested under quasi-static loading may fail in flexure, but could suffer shear failure under rapid enough loading (Saatci and Vecchio 2009, Kishi and Bhatti 2010). Similar behavior will likely not occur under seismic loading because the rate of loading is typically not fast enough to change the mode of failure. Nevertheless, given the strong desire to eliminate brittle shear failure, the effects of capacity design are explored later on in this chapter.

Figure 130 illustrates the essence of the capacity design procedure for a column subjected to a concentrated load at 1/4 span. For a mechanism comprised of 3 plastic hinges (with capacity M_p) as shown in figure 130, the maximum shear force at the base of the pier is $8M_p/L$. Designing for a shear capacity of at least $8M_p/L$ will promote formation of the plastic hinge mechanism and protect the column against shear failure because the applied shear force is capped to $8M_p/L$ by the plastic mechanism that has formed.

Six RC bridge piers are designed according to the capacity design procedure outlined above. Based on the information in chapter 4, the impact load is considered to be concentrated 5 ft (1,524 mm) from the ground level. Table 10 and figure 131 show the geometry and reinforcements arrangements for these six redesigned piers. Twenty four inch rectangular piers are not considered because most of them are destroyed at speeds as low as 50 mph.

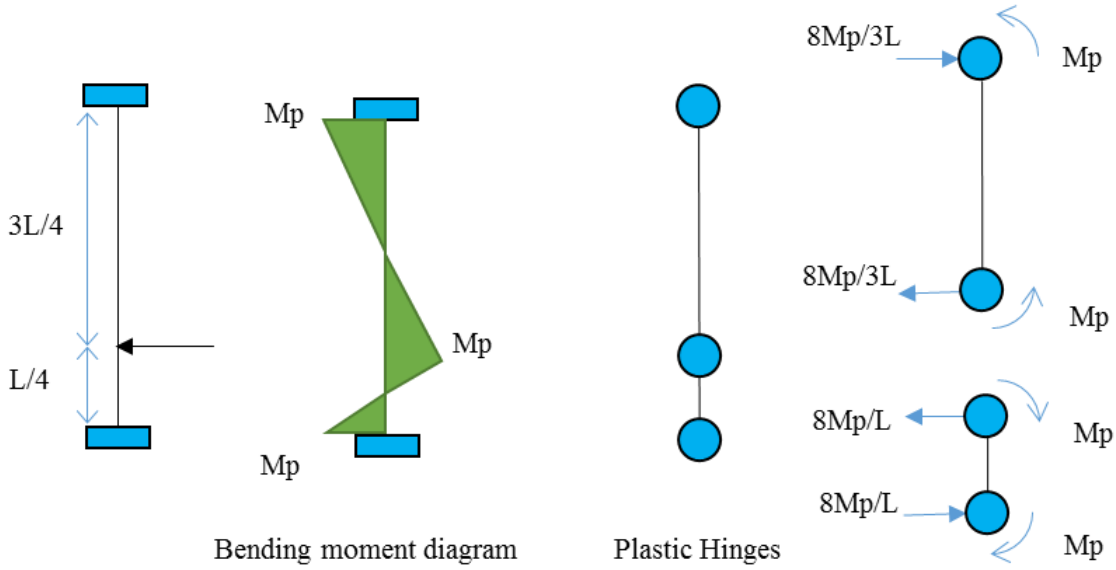

Figure 130. Illustration. Designing a pier using the capacity design procedure.

Table 10. Geometry and reinforcement arrangement for the capacity designed columns.

Section	Pier Height (ft)	Longitudinal Bars	Stirrups Bars	Shear Capacity (kips)
30x30 (rectangular)	16	Bar #10 4x4	4 x #6 6-in Spacing	588
36x36 (rectangular)	16	Bar #11 4x4	4 x #6 6-in Spacing	750
42x42 (rectangular)	16	Bar #14 4x4	4 x #6 4-in Spacing	1,257
30 (circular)	16	8 x Bar #10	2 x #6 6-in Spacing	305
36 (circular)	16	8 x Bar #14	2 x #8 6-in Spacing	617
42 (circular)	16	8 x Bar #14	2 x #8 6-in Spacing	750

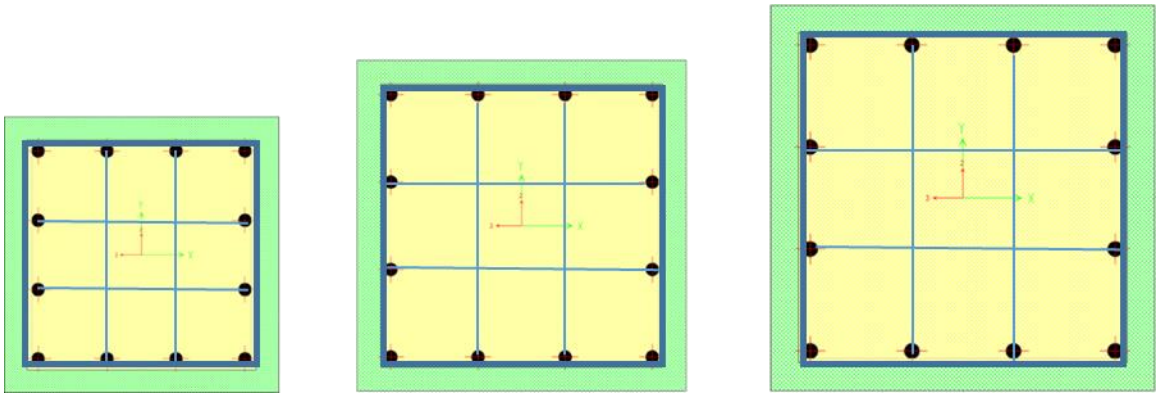

(a) 30-in rectangular pier. (b) 36-in rectangular pier. (c) 42-in rectangular pier.

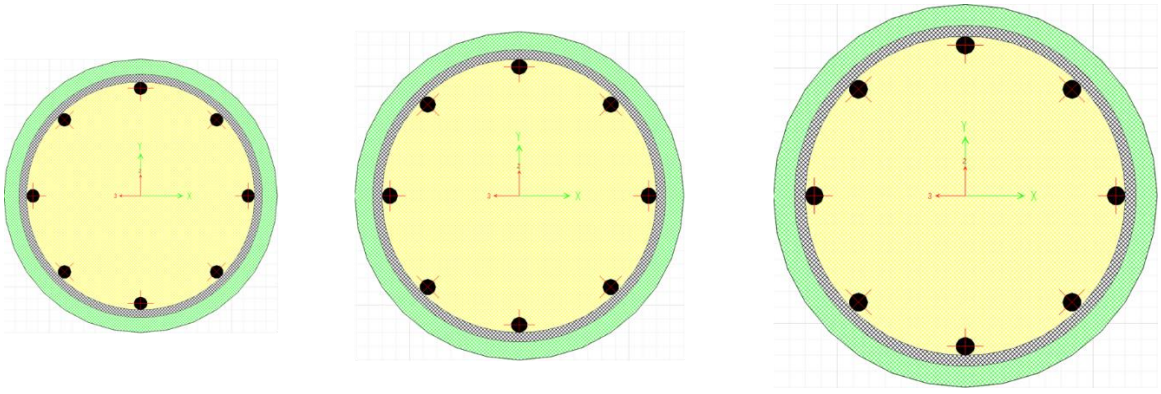

(d) 30-in circular pier. (e) 36-in circular pier. (f) 42-in circular pier.

Figure 131. Illustration. Different sections of the pier.

QUALITATIVE DESCRIPTIONS OF DAMAGE MECHANISMS

Liu (2012) identified possible failure modes of bridge piers subjected to truck collision and provided qualitative descriptions for these mechanisms. In this work, the following modes of failure are recognized:

- Concrete Cover Failure: The concrete cover fails. It either crushes under direct compressive loading or spalls off, for example, due to reflected stress waves.
- Shear Failure: The pier deforms excessively or fails primarily in shear. This failure mode is characterized by early diagonal cracking and eventual damage of the concrete core.
- Plastic Hinge Formation: The pier suffers initial flexural cracking then eventual plastic hinging as the main steel yields.

Figure 132 shows an example of shear failure as computed and observed in the aftermath of actual accidents involving truck collision with bridge piers, while figure 133 shows an example of plastic hinging. It should be noted that these modes of failure can also be categorized per the damage definitions in Liu (2012).

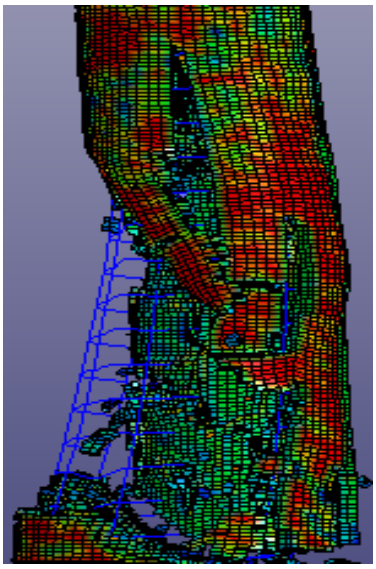

(a) FE simulation.

Source: FHWA

(b) Texas I45 bridge accident 2014.

Figure 132. Photos. Shear failure from simulation and accident.

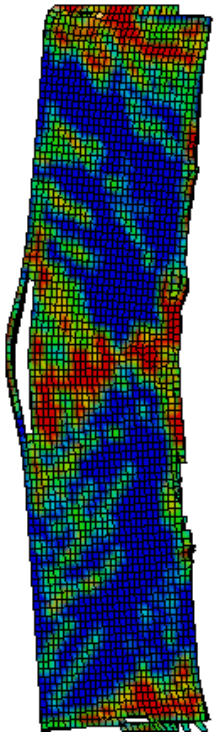

©2003 MnDoT

(a) FE simulation. (b) Minnesota I90 bridge accident (2003).

Figure 133. Photos. Flexure hinging at middle of column.

QUANTITATIVE MEASURES OF DAMAGE MODES

The above descriptions for the modes of failure are qualitative. To enable performance-based design, the actual levels of shear distortion and plastic rotation are computed for panels along the pier height. The displacements of the corner nodes of each panel (in the plane of impact) are computed and the relative displacements with respect to the panel bottom are identified as shown in figure 134. In figure 134, V_L and V_R are the relative vertical displacements of the upper left and right corner nodes, respectively, and U_L and U_R represent the relative horizontal displacements of the upper left and right corner nodes, respectively.

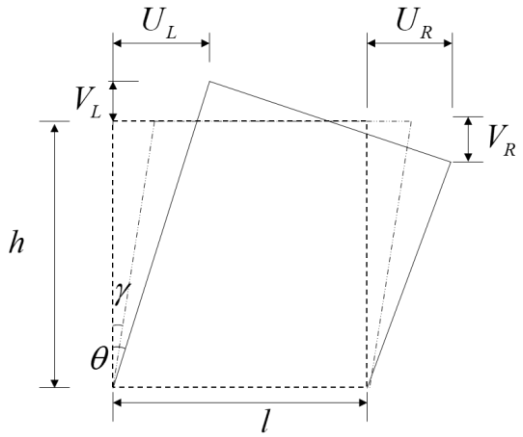

Figure 134. Illustration. Deformation of a panel subjected to lateral load.

The shear distortion and plastic rotation of the panel are computed according to Hiraishi (1984) and outlined in equations (19) through (22).

$$\theta = \frac{(V_L - V_R)}{l} \tag{19}$$

$$u_B = \int_0^h \frac{1}{l}(V_L - V_R)d_y \tag{20}$$

$$u_S = \frac{1}{2}(U_L + U_R) - u_B \tag{21}$$

$$\gamma = \frac{u_S}{h} \tag{22}$$

where θ is the plastic rotation and γ is the shear distortion, h is the height of the panel, l is the width of the panel, u_B is the lateral displacement due to bending and u_S is the lateral displacement by shear.

EFFECT OF CAPACITY DESIGN ON PIER PERFORMANCE

To investigate the effect of truck impact, each pier is vertically divided into 8 panels and the shear distortion and plastic rotation for each panel are computed per equations (19) through (22). Table 11 summarizes all the calculated results, while figure 135 shows the results of the computation for two cases. As shown in figure 135, the maximum shear distortion and plastic rotation are 0.083 and 0.016, respectively, for case C_P2_V55_W20, are 0.012 and 0.003, respectively, for case C_P3_V70_W40. The maximum shear deformation occurs at the top or bottom of each column, and substantial plastic rotation occurs around the impact location as well as at the top and bottom locations. Based on the amount of shear distortion for both of these cases, it is clear that the dominating mode of deformation of these two cases is shear, although flexural hinging still plays an important role. It is also clear from figure 135 that the piers in both cases have suffered severe damage, as evident from the extensive red contours in the pier.

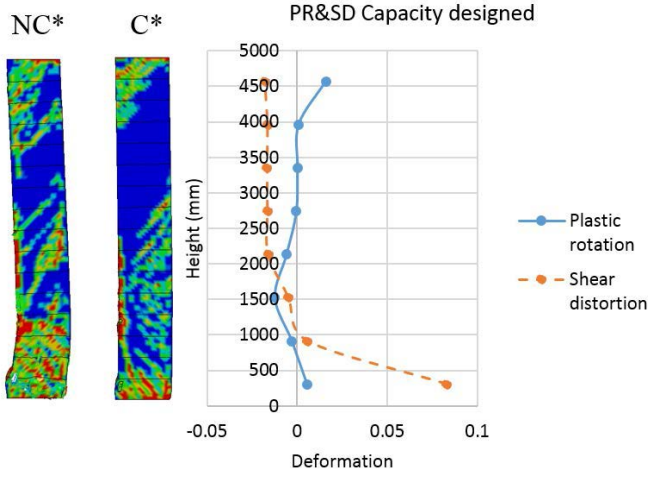

(a) P2_V55_W20.

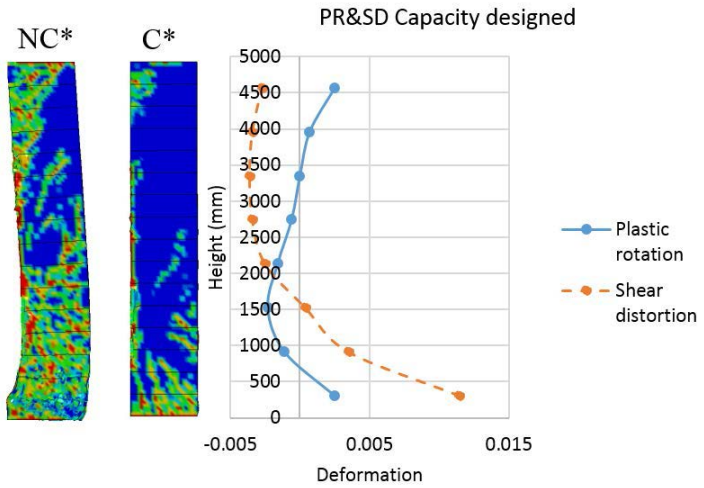

(b) P3_V70_W40.

*NC – non capacity design, *C – capacity designed

Figure 135. Photos and graphs. Shear distortion and plastic rotation results for two selected cases.

Table 11 suggests that most of the non-capacity designed piers will exhibit more extensive shear deformations during the vehicle impact event than their capacity designed counterparts. This is evident in figure 136, which plots the maximum shear distortion and plastic rotation values as a function of impact speed. For example, for case P2_V50_W40, the shear distortion decreases from 0.213 to 0.015 for capacity designed versus non-capacity designed bridge piers. The information in table 11 and figure 136 support an argument that the likelihood of excessive shear deformation, and hence achieving an undesirable mode of failure, can be decreased by using capacity design approach.

Table 11. Shear distortion and plastic rotation comparisons between capacity designed and non-capacity designed RC bridge piers.

Case	Shear Distortion (NC*)	Shear Distortion (C**)	Plastic Rotation (NC)	Plastic Rotation (C)
P2_V30_W40	0.0023	0.0023	0.0018	0.0018
P2_V40_W40	0.0040	0.0040	0.0031	0.0034
P2_V50_W40	0.2130	0.0150	0.0360	0.0036
P2_V60_W40	N/A	N/A	N/A	N/A
P2_V70_W40	N/A	N/A	N/A	N/A
P2_V30_W30	0.0023	0.0024	0.002	0.002
P2_V40_W30	0.0040	0.0040	0.0032	0.0035
P2_V50_W30	0.1331	0.0100	0.0494	0.0052
P2_V60_W30	N/A	0.0947	N/A	0.0436
P2_V70_W30	N/A	N/A	N/A	N/A
P2_V30_W20	0.0021	0.0021	0.0018	0.0018
P2_V40_W20	0.0031	0.0038	0.0020	0.0032
P2_V50_W20	0.0635	0.0090	0.006	0.0052
P2_V60_W20	N/A	0.0812	N/A	0.0443
P2_V70_W20	N/A	N/A	N/A	N/A
P3_V30_W40	0.0011	0.0010	0.0010	0.0012
P3_V40_W40	0.0020	0.0020	0.0013	0.0018
P3_V50_W40	0.0030	0.0029	0.0022	0.0023
P3_V60_W40	0.0051	0.0038	0.0018	0.0024
P3_V70_W40	N/A	0.0181	N/A	0.0027
P3_V30_W30	0.0011	0.0010	0.0007	0.0009
P3_V40_W30	0.0019	0.0014	0.0015	0.0012
P3_V50_W30	0.0023	0.0020	0.0019	0.0017
P3_V60_W30	0.0037	0.0041	0.0029	0.0028
P3_V70_W30	N/A	0.0149	N/A	0.0032
P3_V30_W20	0.0010	0.0008	0.0008	0.0007
P3_V40_W20	0.0017	0.0017	0.0014	0.0014
P3_V50_W20	0.0023	0.002	0.0019	0.0016
P3_V60_W20	0.0034	0.0038	0.0023	0.003
P3_V70_W20	N/A	0.0119	N/A	0.0023
P4_V30_W40	0.0007	0.0004	0.0004	0.0004
P4_V40_W40	0.0013	0.0015	0.0009	0.0008
P4_V50_W40	0.0015	0.0012	0.0009	0.0008
P4_V60_W40	0.0019	0.0018	0.0012	0.0011
P4_V70_W40	0.0026	0.0025	0.0015	0.0016

*NC – non capacity design, *C – capacity designed

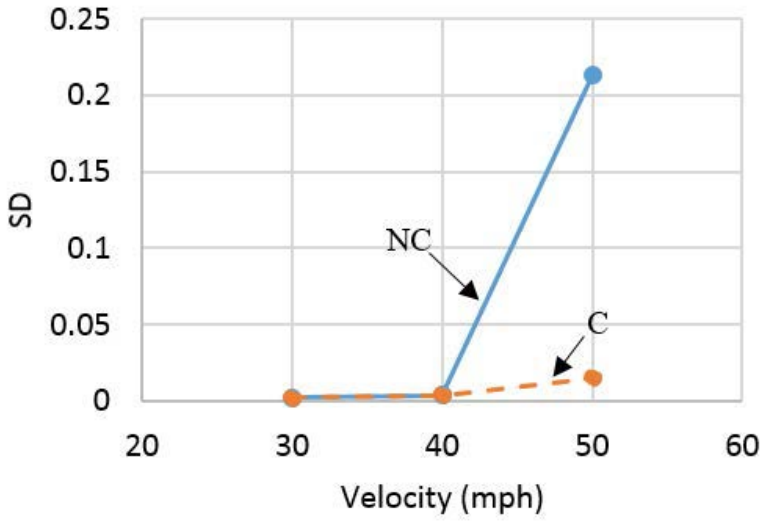

(a) 40-Ton truck.

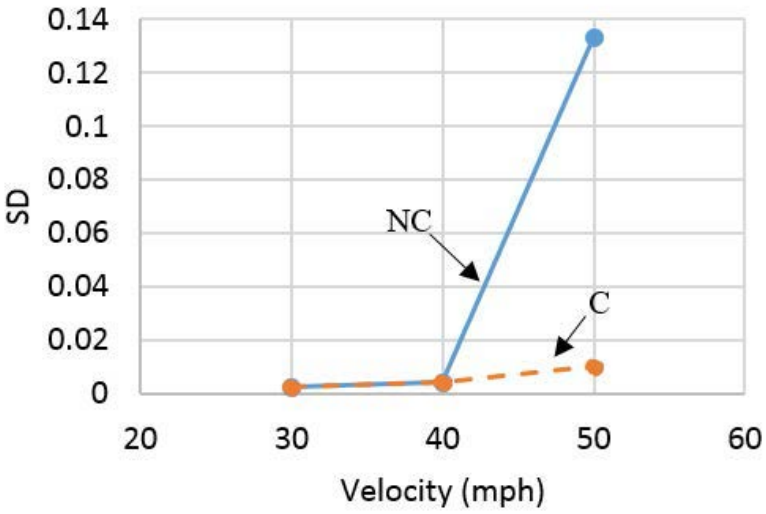

(b) 30-Ton truck.

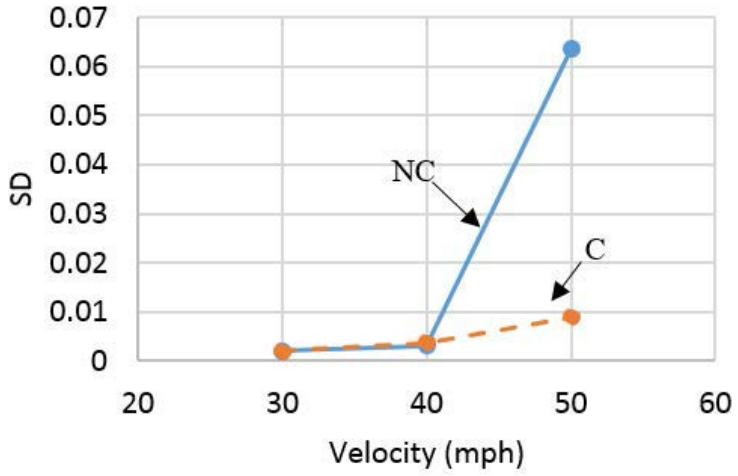

(c) 20-Ton truck.

Figure 136. Graphs. Maximum shear distortion versus truck speed for both capacity designed and non-capacity designed piers (30 inch).

PROPOSED PERFORMANCE-BASED DESIGN FRAMEWORK

A performance-based design framework requires specification of 3 things: 1) demand (D), 2) capacity (C), and 3) a performance objective for a given hazard level. In general, computation of demand for the vehicle impact problem is complicated because it entails running a vehicle model. However, that can be greatly simplified by using the proposed impulse model. As in earthquake engineering, local demands can be obtained by using an elastic model or an inelastic one. Since the objective is to propose a framework that is suitable for design office use, an elastic model is selected. The model employs a reduced moment of inertia (35% of the gross section) to account for the effect of concrete cracking.

The impulse model proposed in chapter 4 is applied to an elastic model of the pier, which is then used to compute the peak shear and moment demands. The capacity of the pier to resist the applied loads is computed from well-established design techniques, e.g., in ACI-318 (2011). Since D is computed from an elastic model and C is computed assuming inelastic behavior, the ratio of D/C is essentially a qualitative indicator of severity of the event. In other words, a high D/C ratio means that the event was a severe one and vice versa. The use of such qualitative indicators for performance-based design is well established in earthquake engineering (FEMA 356, 2000), e.g., the *m* factor, which is a demand modifier intended to account for the expected ductility of the member.

The performance objective is typically a qualitative one, e.g., damage is minor, moderate or major as defined in Liu (2012). Following Liu (2012) and in line with the previous definitions for damage, the failure modes associated with the minor damage state are tensile cracking of concrete and minor yielding of the longitudinal reinforcement. Bridge piers with minor damage are fully functional immediately after impact. Moderate damage is defined by the occurrence of

major yielding and plastic deformations within the steel reinforcement as well as minor concrete core deterioration. Closure of the bridge may be necessary for repair of a moderately damaged bridge pier. Severe damage is associated with plastic hinge formation in the pier and/or major damage of the concrete core. A bridge with severe damage will not collapse, but likely be prohibitive to repair and need to be replaced after the impact event. Figure 137 shows examples of piers impacted by a heavy truck and judged to have minor, moderate and major damage as obtained from the finite element data.

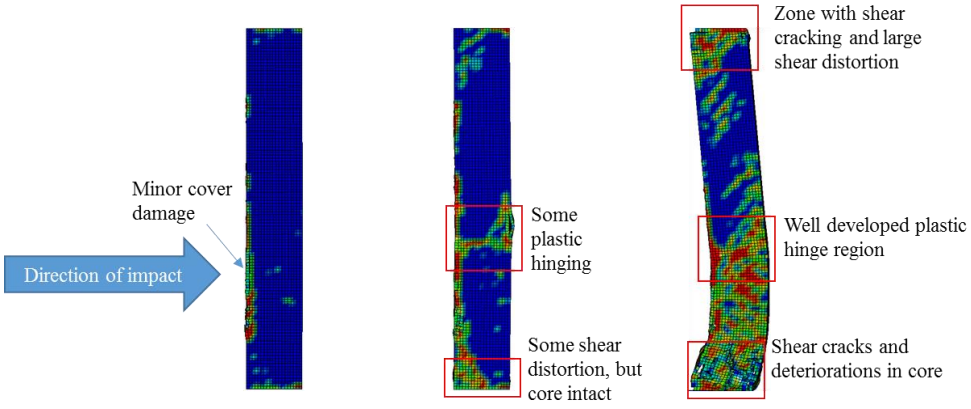

(a) Minor damage. (b) Moderate damage. (c) Severe damage.

Figure 137. Illustration. Examples of the various modes of failure by the heavy truck impact.

To make the damage assessment process more quantitative, two quantities are computed for each pier, the maximum shear distortion (SD) and plastic rotation (PR). The use of such quantities as performance criteria is common in seismic performance-based design. It is not, however, feasible to adapt earthquake-related SD and PR values to impact because the type of demand is different; seismic effects entail cyclic loads, whereas impact is mostly monotonic. As such, the damage states are estimated as noted above from the finite element data obtained in this research and can be refined in the future as more experimental data becomes available. Also, unlike earthquake engineering, the hazard level is not random. For example, a bridge on a highway with a permissible speed of 70 mph will likely not see speeds well in excess of this number, particularly since most impact situations are accidental. In addition, it does not make sense to tie the performance objective to truck speeds because trucks on a highway will likely be travelling at the highest permissible speed.

A performance-based approach based on maximum shear distortion (SD) and plastic rotation (PR) for the design of bridge piers impacted by single unit trucks was developed by Xu (2017). As outlined in Xu (2017), PR and SD values associated with minor, moderate and major damage for single unit trucks on bridge piers are listed in table 12. Figure 138 shows a plot of the PR and SD quantities versus the demand capacity ratio (D/C) for single unit trucks (Xu 2017). There is a clear trend in that the quantities increase almost linearly with increase in the D/C ratio. By correlating the observed damage modes and superimposing them on the data in figure 138, it is possible to select general regions that could be used for performance-based design. For example, the data in figure 138 and table 12 show that the D/C ratio should be less than 1.25 to ensure minor damage and should be between 1.25 and 2.00 for moderate damage. Values that exceed 2.00 are likely to suffer severe damage that may cause collapse. Xu (2017) has proposed a

design approach based on information in table 12 and figure 138 for the design of bridge piers impacted by medium weight trucks.

Table 12. Performance levels, corresponding damage state, shear distortion or plastic rotation for single-unit truck (Xu 2017).

Performance Level	Damage State	D/C Range	Max(SD, PR)
Immediate use	Minor	[0, 1.25]	[0, 0.010]
Damage control	Moderate	[1.25, 2.00]	[0.010, 0.075]
Near collapse	Severe	[2.00, 3.00]	[0.075, 0.150]

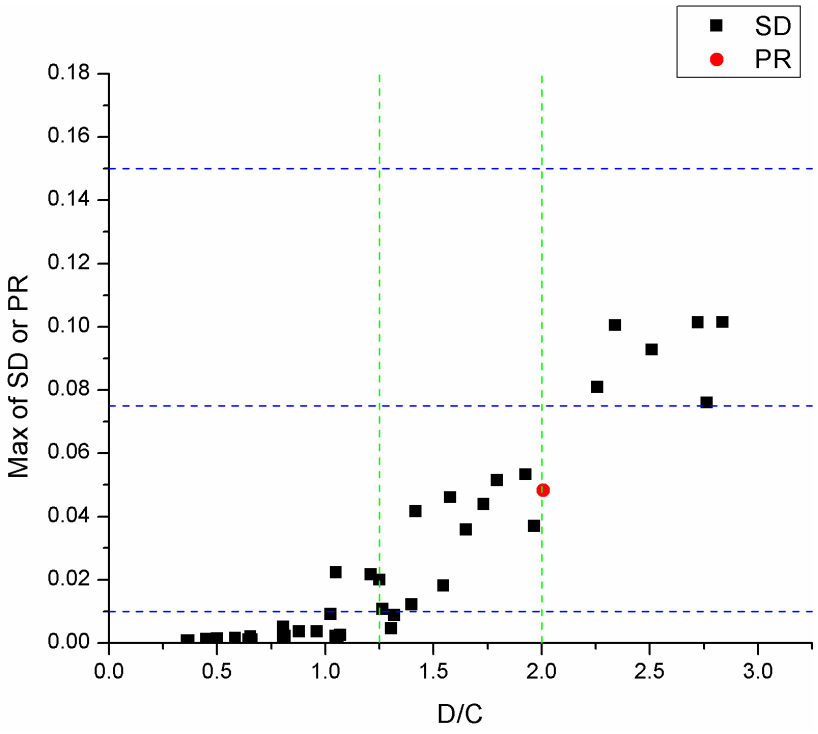

Figure 138. Graphs. Plastic rotation & shear distortion versus D/C ratio for bridge piers impacted by single-unit truck (Xu 2017).

For heavy vehicle impact investigated in this research, the maximum PR and SD quantities versus the D/C ratio are plotted in figure 139 and figure 140. Data for bumper and engine impact (figure 139) and trailer impact (figure 140) are plotted separately. By correlating the observed damage modes and superimposing them on the data in figure 139 and figure 140, it is possible to select general regions that could be used for performance-based design. For example, the data in figure 139 and table 13 show that the D/C ratio should be less than 2.00 to ensure minor damage and should be between 2.00 and 2.75 for moderate damage. Values that exceed 2.75 are likely to suffer severe damage as a result of engine impact.

Engine impact sets the stage for the subsequent trailer impact, which has different characteristics. Even if limited to D/C < 2.75, engine impact creates initial damage in the form of substantial

concrete cracking. Cracked concrete degrades the concrete's contribution to shear resistance. In other words, the subsequent trailer impact is primarily resisted by the steel shear reinforcement.

Unlike the bumper and engine impacts, the force time history associated with trailer impact is substantially lower, but has a much longer duration. The long duration of the trailer pulse makes it more similar to quasi-static loading. To consider the sequence of impact, if the bumper/engine impact caused minor damage, the shear capacity C is computed based on the full section. For piers with moderate damage caused by bumper/engine, shear capacity C is computed based on the steel stirrups only and the concrete contribution is ignored because the concrete could potentially be severely damaged by the initial bumper/engine impact. In this case the capacity is denoted Cs.

The data in figure 139 and figure 140 suggest the following design philosophy for this situation:

- Immediate Use (Minor damage): (larger of D1/C or D2/C) < 2.00 for bumper/engine impact and D3/C < 0.75 for trailer impact.
- Damage Control (Moderate damage): (larger of D1/C or D2/C) < 2.00 for bumper/engine impact and 0.75 ≤ D3/C < 1.2 for trailer impact.
- Damage Control (Moderate damage): 2.00 ≤ (larger of D1/C or D2/C) < 2.75 for bumper/engine impact and 0.75 ≤ D3/Cs < 1.2 for trailer impact.
- Near Collapse (Severe damage): 2.00 ≤ (larger of D1/C or D2/C) < 2.75 for bumper/engine impact and 1.2 ≤ D3/Cs < 1.6 for trailer impact.

Here, D1 represents the base shear from bumper impact, and D2 represents the base shear from engine impact, and D3 represents the base shear from trailer impact.

Table 13. Performance levels, corresponding damage state, shear distortion or plastic rotation (bumper/engine impact for tractor-trailer).

Performance Level	Damage State	Max (D1/C, D2/C)	Max(SD,PR)
Immediate use	Minor	[0, 2.00]	[0, 0.010]
Damage control	Moderate	[0, 2.75]	[0.010, 0.075]
Near collapse	Severe	[2.00, 2.75]	[0.075, 0.150]

Table 14. Performance levels, corresponding damage state, shear distortion or plastic rotation (trailer impact for tractor-trailer).

Performance Level	Damage State	D3/C(D3/Cs)	Max(SD,PR)
Immediate use	Minor	[0, 0.75]	[0, 0.010]
Damage control	Moderate	[0.75, 1.20]	[0.010, 0.075]
Near collapse	Severe	[1.20, 1.60]	[0.075, 0.150]

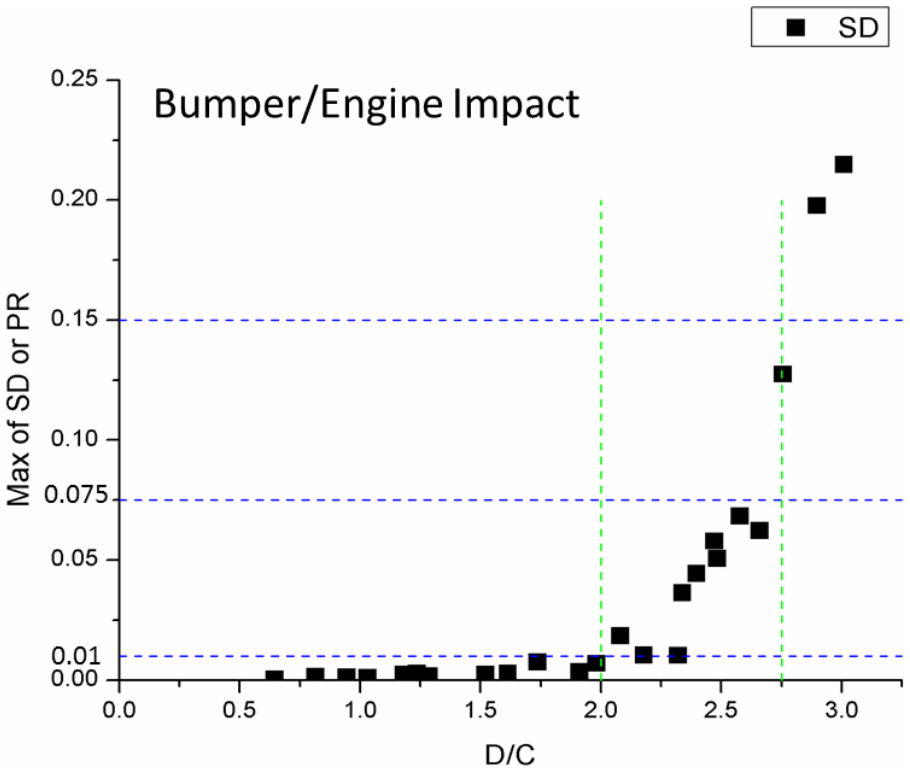

Figure 139. Graph. Max of SD or PR versus D/C for the bumper and engine impact of tractor-semitrailer.

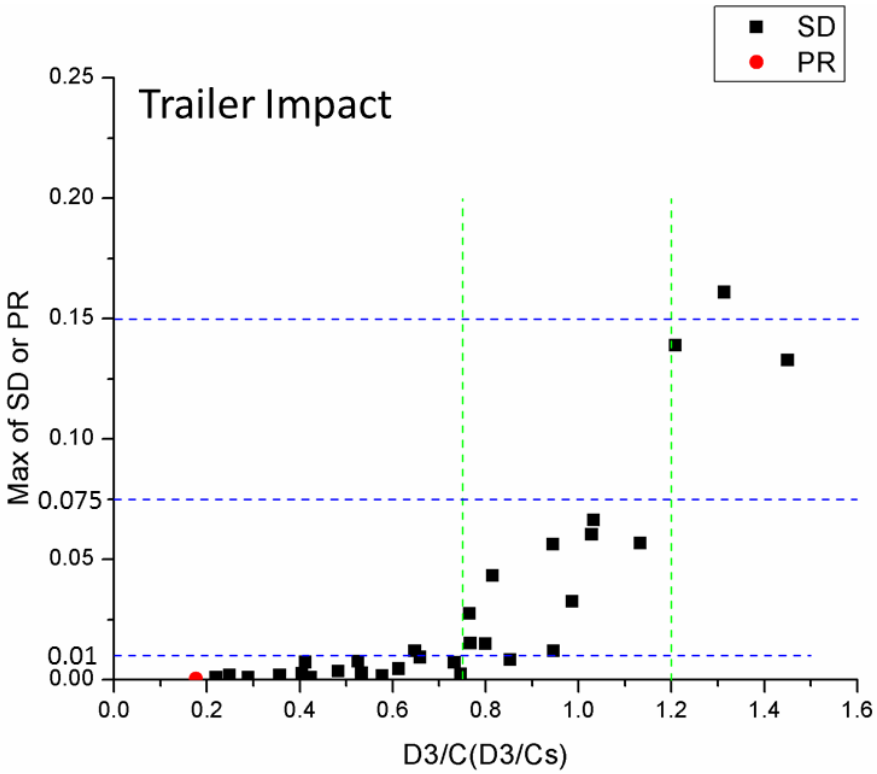

Figure 140. Graph. Max of SD or PR versus D/C for the trailer impact of tractor-semitrailer.

SINGLE UNIT TRUCK VERSUS TRACTOR-SEMITRAILER IMPACT

Xu (2017) investigated the impact of single unit trucks on bridge piers. Figure 141, figure 142, and figure 143 show a comparison between the effects of impact by the single unit truck and the tractor trailer used in this work. The demands delivered by the heavy truck and single-unit truck are computed for a 36-in elastic pier impacted by a 40-Ton tractor-semitrailer and a 10-Ton single-unit truck. The impact speeds for both trucks are 50 mph. The engine impact and cargo impact scenario for the two truck models are shown and compared in figure 141 and figure 142, respectively. The impact force time histories from the simulations are plotted in figure 143.

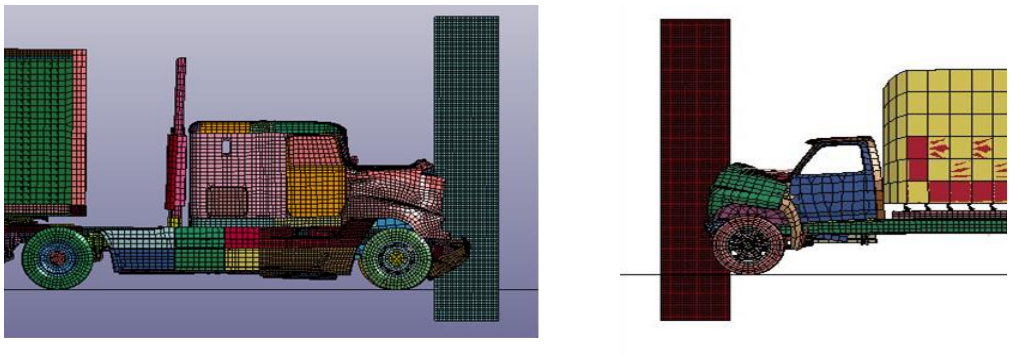

(a) Heavy truck. (b) Single-unit truck.

Figure 141. Photos. Engine impact scenario in LS-DYNA for heavy truck and single-unit truck.

(a) Heavy truck. (b) Single-unit truck.

Figure 142. Photos. Cargo impact scenario in LS-DYNA for heavy truck and single-unit truck.

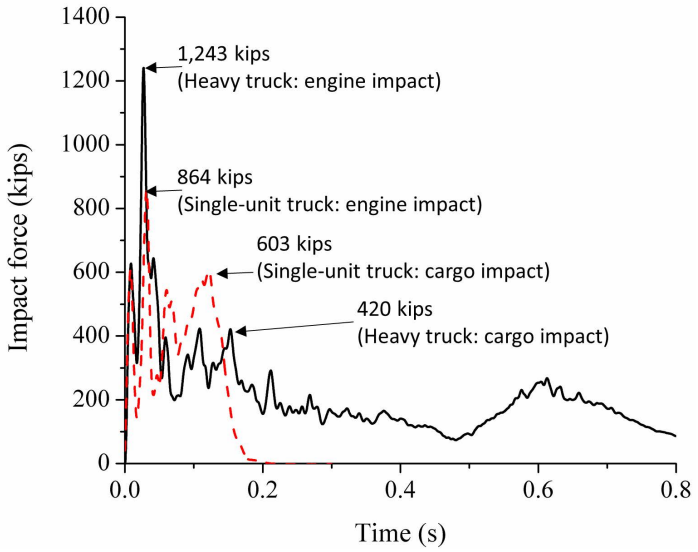

Figure 143. Graph. Impact force time histories of single-unit truck and heavy truck in LS-DYNA.

It is clear from figure 143 that the peak impact force caused by a heavy truck, i.e., tractor-semitrailer, is much higher than that for the single-unit truck. In this case, the peak force for both trucks occurs when the engine hits the pier. Also, the cargo impact demands are different in terms of the amplitude and duration of each impact pulse as shown in figure 143. The single-unit truck has a higher cargo impact force but much shorter impulse duration than those for the heavy truck, which could result in different impact behaviors of the collided pier. It has also been observed that the cargo impact forces for the heavy truck are usually applied at a lower height to the pier. Hence, the shear damage mode is more prominent in the heavy truck impact event, rather than flexure.

PROPOSED DESIGN PROCEDURE

The information presented in this report is synthesized into the following proposed performance-based design methodology:

1. Design the pier for strength/service limit states.

2. Determine the design speed and weight of the impacting truck based on local traffic conditions and owner requirements.

3. Determine the desired performance level: Immediate Use (Minor damage), Damage Control (Moderate damage) or Near Collapse (Severe Damage). Select the required D/C ratio.

4. Apply the pulse model to an elastic model of the pier (with reduced stiffness to account for shear cracking) to get the elastic base shear demands (D1, D2, and D3).

5. Determine required shear capacity C = D2/(D/C) ratio. Assuming a three-hinge mechanism, use the capacity design procedure to calculate the required Mp = 5ft * C/2. Select the longitudinal flexural reinforcement to satisfy Mp.

6. Select a stirrup configuration to satisfy C and compute the capacity of the steel stirrups, Cs_{design}. Compute the actual shear capacity C_{design} and moment capacity M_{design}.

7. Use the actual capacity to check if the plastic mechanism is still preferred over shear failure. Use M_{design} in the 3 hinge capacity design configuration to get the shear value, and make sure the shear value is less than the shear capacity (C_{design}). If not, either decrease moment capacity if overdesigned (but not less than Mp) or increase the shear capacity, C_{design}.

8. Calculate the larger of $D1/C_{design}$ and $D2/C_{design}$, associated with bumper and engine impacts, respectively, and $D3/C_{design}$ or $D3/Cs_{design}$ for the trailer impact.

9. Check to see if the computed demand to capacity ratios corresponds to the desired damage level. If not, go back and change the pier size or desired performance level:

    - Immediate Use (Minor damage): (larger of $D1/C_{design}$ or $D2/C_{design}$) < 2.00 for bumper/engine impact and $D3/C_{design}$ < 0.75 for trailer impact.
    - Damage Control (Moderate damage): (larger of $D1/C_{design}$ or $D2/C_{design}$) < 2.00 for bumper/engine impact and $0.75 \leq D3/C_{design} < 1.20$ for trailer impact.
    - Damage Control (Moderate damage): $2.00 \leq$ (larger of $D1/C_{design}$ or $D2/C_{design}$) < 2.75 for bumper/engine impact and $0.75 < D3/Cs_{design} < 1.20$ for trailer impact.
    - Damage Control (Severe damage): $2.00 \leq$ (larger of $D1/C_{design}$ or $D2/C_{design}$) < 2.75 for bumper/engine impact and $1.20 \leq D3/Cs_{design} < 1.60$ for trailer impact.

    Here, D1 represents the base shear from bumper impact, and D2 represents the base shear from engine impact, and D3 represents the base shear from trailer impact, as discussed previously.

VALIDATION OF THE PROPOSED FRAMEWORK

Three piers with characteristics that are different than those used earlier are selected to validate the proposed performance-based design framework. The geometries and reinforcing details of the selected piers are shown in table 15. The piers are capacity designed to minimize shear failure as noted earlier. Following the design procedure outlined earlier, the selected piers are then designed for impact by trucks with different approach speeds and weights as outlined in table 16.

Each specific case is modeled using the detailed computational models developed earlier and the actual peak SD and PR values computed. These values are listed in table 16 and the actual damage states according to the previously defined damage ranges are specified based on the information in table 13, table 14, figure 139 and figure 140. As shown in table 16, the predictions

are accurate for all five cases. These results show that the proposed framework is reasonable, given the complexity of the collision process being modeled.

Table 15. Pier geometry for validation study.

Column ID	Column Dimension (in)	Column Height (ft)	Longitudinal Bars	Stirrups	C_{design} (kips)	CS_{design} (kips)
1	39 (circular)	20	8 x Bar #14	Bar #6 Spacing of 3 in	740	550
2	33 (rectangular)	18	Bar #10 4×4	4 x Bar #6 Spacing of 6 in	600	464
3	33 (rectangular)	20	Bar #10 4×4	4 x Bar #6 Spacing of 6 in	600	464

Table 16. Selected cases for validation of proposed method.

Case	Truck Characteristics	Column ID	$D2/C_{design}$	$D3/C_{design}$ ($D3/Cs_{design}$)	Predicted Damage Level	Max(SD, PR)	Actual Damage Level
1	50mph_80kips	1	1.40	0.64	Minor	0.003	Minor
2	60mph_80kips	3	2.22	1.31	Severe	0.161	Severe
3	60mph_40kips	2	2.25	0.78	Moderate	0.030	Moderate
4	60mph_60kips	3	2.22	1.10	Moderate	0.059	Moderate
5	40mph_80kips	3	1.85	0.55	Minor	0.003	Minor

CHAPTER 6. CONCLUSIONS, LIMITATIONS AND FUTURE WORK

SUMMARY AND CONCLUSIONS

An extensive investigation of vehicular impact on bridge piers has been conducted to develop a performance-based procedure. The work carried out in this research includes calibration of a material model using available data in the literature, validation of the material model and damage modes through pendulum impact testing on a large scale three column pier-bent model, and development of a performance-based guideline for the design of bridge piers against impact by heavy trucks. Key highlights and conclusions of this research are as follows.

- Modeling of concrete piers in LS-DYNA was done using the Continuous Surface Cap Model (CSCM). Based on impact test data available in the literature, input parameters for this model were calibrated so that both the damage modes and force / displacement time-history from numerical simulation match well with those from the test.
- A large scale model of a three-column pier bent was constructed at the Federal Outdoor Laboratory (FOIL) located at the FHWA center in McLean, VA. This model was ½ scale to a prototype bridge in New York in length and height, although pier sizes were scaled down to 1/3rd because of limitations with the impactor weight. Two outer piers of the model were impacted by a 2-ton pendulum at approximately 20 mph. Data obtained from this test were used to validate both the material model as well as damage modes observed during numerical simulations. The pendulum impact was designed to simulate vehicular impact characteristics.
- Based on extensive simulations of collision between a truck model and a calibrated model of a pier, a three-triangular pulse model was proposed for simulating impact by a tractor-trailer on bridge piers. Parameters of this pulse model, including the height where the triangular pulses are applied to simulate vehicular impact, were derived based on nonlinear regression of impact force information obtained from more than 45 cases of impact of tractor-trailers of different weights and velocities on piers of different sizes. The accuracy of this pulse model was demonstrated through comparison between results using truck impact and pulse application.
- A performance-based approach for the design of bridge piers was developed by quantifying damage in terms of plastic rotation and shear distortion and the performance in terms of demand / capacity (D/C) ratios. The approach is simple enough for design office use and proposes three levels of performance immediate use, damage control and near collapse. Applicability of the proposed design approach was demonstrated through several cases that were not included in the calibration of the proposed design method.

LIMITATIONS AND FUTURE WORK

- The impact on bridge piers is affected by the characteristics of the cargo. In this research, the cargo consisted of sand ballast. Further work is needed to investigate the effect of other cargo types based on data from actual trucks that impacted bridge piers. This work

may result in further adjustment of the parameters of the pulse model proposed in this research.

- The pulse equations were derived using a single type of truck that had given bumper characteristics and engine weight. Therefore, in order to generalize the proposed pulse equations, additional studies should be conducted with a variety of truck designs to confirm that they are reasonably representative of the heavy tractor semi-trailer truck population in the US. By considering the uncertainties from the truck and bridge pier, the performance-based design proposed in this study could be more comprehensive.
- Although the large-scale pendulum test provided valuable information, a full-scale test using a tractor-semitrailer is needed to further verify damage modes and the proposed performance-based approach. The two full-scale tests carried out by the Texas Transportation Institute on rigid piers don't represent impact of heavy weight trucks on concrete bridge piers in a realistic manner because real piers are flexible and can suffer damage. Such tests need to be carried out on full-scale pier bent model that can represent the behavior of a whole bridge during impact.

ACKNOWLEDGMENTS

The authors sincerely acknowledge support of Dr. Chuck Plaxico of RoadSafe, LLC, with the finite element model of the tractor-semitrailer in LS-DYNA, and Mr. Christopher Story and Eduardo Arispe of Federal Outdoor Impact Laboratory (FOIL) at FHWA center in McLean, VA for the help with impact testing.

This research was also supported, in part, under National Science Foundation Grants CNS-0958379, CNS-0855217, ACI-1126113 and the City University of New York High Performance Computing Center at the College of Staten Island.

Any opinions, findings and conclusions or recommendations expressed in this publication are those of the authors and do not necessarily reflect the views of the Federal Highway Administration or the National Science Foundation.

REFERENCES

AASHTO (1998). "Bridge Specifications." *American Association of State Highway and Transportation Officials, 2nd ed., Washington, DC*, 1116.

AASHTO (2012). "*AASHTO LRFD Bridge Design Specifications*", American Association of State Highway and Transportation Officials.

Abdelkarim, O. I., and ElGawady, M. A. (2016). "Design of short reinforced concrete bridge columns under vehicle collision." *Transportation Research Record: Journal of the Transportation Research Board*(2592), 27-37.

Abdelkarim, O. I., and ElGawady, M. A. (2016). "Performance of hollow-core FRP–concrete–steel bridge columns subjected to vehicle collision." *Engineering Structures*, 123, 517-531.

Abdelkarim, O. I., and ElGawady, M. A. (2017). "Performance of bridge piers under vehicle collision." *Engineering Structures*, 140, 337-352.

Abu-Odeh, A. "Modeling and simulation of bogie impacts on concrete bridge rails using LS-DYNA." *Proc., 10th international LS-DYNA Users Conference, Livermore Software Technology Corporations, June*, 8-10.

ACI-318. (2011). "Building code requirements for structural concrete (318-11) and commentary-(318R-11)." *Detroit, Michigan: American Concrete Institute*.

Adhikary, S. D., Li, B., and Fujikake, K. (2012). "Dynamic behavior of reinforced concrete beams under varying rates of concentrated loading." *International Journal of Impact Engineering*, 47, 24-38.

Agrawal, A. K., and Chen, C. (2011). "Bridge vehicle impact assessment." University Transportation Research Center, New York State Department of Transportation.

Agrawal, A. K., Liu, G. Y., and Alampalli, S. "Effects of truck impacts on bridge piers." *Proc., Advanced Materials Research*, Trans Tech Publ, 13-25.

AuYeung, S., and Alipour, A. "Performance of RC Members under Impact Loads." *Proc., Geotechnical and Structural Engineering Congress 2016*, 14-24.

Banthia, N., Mindess, S., and Bentur, A. (1987). "Impact behaviour of concrete beams." *Materials and Structures*, 20(4), 293-302.

Brara, A., and Klepaczko, J. R. (2007). "Fracture energy of concrete at high loading rates in tension." *International Journal of Impact Engineering*, 34(3), 424-435.

Buth, C. E., Brackin, M. S., Williams, W. F., and Fry, G. T. (2011). "Collision loads on bridge piers: phase 2. Report of guidelines for designing bridge piers and abutments for vehicle collisions."

Buth, C. E., Williams, W. F., Brackin, M. S., Lord, D., Geedipally, S. R., and Abu-Odeh, A. Y. (2010). "Analysis of large truck collisions with bridge piers: phase 1. Report of guidelines for designing bridge piers and abutments for vehicle collisions."

Chen, L., El-Tawil, S., and Xiao, Y. (2016a). "Reduced models for simulating collisions between trucks and bridge piers." *Journal of Bridge Engineering*, 21(6), 04016020.

Chen, L., Xiao, Y., and El-Tawil, S. (2016b). "Impact Tests of Model RC Columns by an Equivalent Truck Frame." *Journal of Structural Engineering*, 142(5), 04016002.

Chen, L., Xiao, Y., Xiao, G., Liu, C., and Agrawal, A. K. (2015). "Test and numerical simulation of truck collision with anti-ram bollards." *International Journal of Impact Engineering*, 75, 30-39.

Chung, C. H., Lee, J., and Gil, J. H. (2014). "Structural performance evaluation of a precast prefabricated bridge column under vehicle impact loading." *Structure and Infrastructure Engineering*, 10(6), 777-791.

El-Tawil, S., Severino, E., and Fonseca, P. (2005). "Vehicle collision with bridge piers." *Journal of Bridge Engineering*, 10(3), 345-353.

FEMA, P. (2000). "Commentary for the seismic rehabilitation of buildings." *FEMA-356, Federal Emergency Management Agency, Washington, DC*.

Fujikake, K., Li, B., and Soeun, S. (2009). "Impact response of reinforced concrete beam and its analytical evaluation." *Journal of Structural Engineering*, 135(8), 938-950.

Grote, D., Park, S., and Zhou, M. (2001). "Dynamic behavior of concrete at high strain rates and pressures: I. experimental characterization." *International Journal of Impact Engineering*, 25(9), 869-886.

Hallquist, J. O. (2006). "LS-DYNA theory manual." *Livermore software technology corporation*, 3, 25-31.

Harik, I., Shaaban, A., Gesund, H., Valli, G., and Wang, S. (1990). "United States bridge failures, 1951–1988." *Journal of Performance of Constructed Facilities*, 4(4), 272-277.

Hiraishi, H. "Evaluation of shear and flexural deformations of flexural type shear walls." *Proc., Proceeding of 8th WCEE*.

Joshi, A. S., and Gupta, L. M. (2012). "A simulation study on quantifying damage in bridge piers subjected to vehicle collisions." *International Journal of Advanced Structural Engineering*, 4(1), 1-13.

Kaewunruen, S., and Remennikov, A. M. (2007). "Field trials for dynamic characteristics of railway track and its components using impact excitation technique." *Ndt & E International*, 40(7), 510-519.

Kishi, N., and Bhatti, A. Q. (2010). "An equivalent fracture energy concept for nonlinear dynamic response analysis of prototype RC girders subjected to falling-weight impact loading." *International Journal of Impact Engineering*, 37(1), 103-113.

Kishi, N., Nakano, O., Matsuoka, K., and Ando, T. "Experimental study on ultimate strength of flexural-failure-type RC beams under impact loading." *Proc., Transactions of the 16th International Conference on Structural Mechanics in Reactor Technology (SMIRT)*.

Krauthammer, T., Elfahal, M., Lim, J., Ohno, T., Beppu, M., and Markeset, G. (2003). "Size effect for high-strength concrete cylinders subjected to axial impact." *International Journal of Impact Engineering*, 28(9), 1001-1016.

Lee, George C., Mai Tong, and W. Phillip Yen. "Design of highway bridges against extreme hazard events: Issues, principles and approaches." (2006).

Lifshitz, J., Gov, F., and Gandelsman, M. (1995). "Instrumented low-velocity impact of CFRP beams." *International journal of impact engineering*, 16(2), 201-215.

Liu, G., (2012). "*Behavior of Bridge Piers during Vehicular Impacts*." Ph.D thesis, City College of New York, City University of New York.

Magallanes, J. M., Wu, Y., Malvar, L. J., and Crawford, J. E. "Recent improvements to release III of the K&C concrete model." *Proc., 11th international LS-DYNA Users conference*, Livermore Software Technology Corporation Livermore, CA, 6-8.

Marzougui, D., Dolci, S., Yonten, K., Eskandarian, A., and Story, C. (2012). "1100C Pendulum Nose Development." NCAC Report.

Miele, C. R., Plaxico, C., Stephens, D., and Simunovic, S. (2010). "U26: Enhanced Finite Element Analysis Crash Model of Tractor-Trailers (Phase C)."

Murray, Y. D. (2007). "Users manual for LS-DYNA concrete material model 159."

Murray, Y. D., Abu-Odeh, A. Y., and Bligh, R. P. (2007). "Evaluation of LS-DYNA concrete material model 159."

Priestley, M. N., Seible, F., Xiao, Y., and Verma, R. (1994). "Steel jacket retrofitting of reinforced concrete bridge columns for enhanced shear strength-part 1: Theoretical considerations and test design." *Structural Journal*, 91(4), 394-405.

Saatci, S., and Vecchio, F. J. (2009). "Effects of shear mechanisms on impact behavior of reinforced concrete beams." *ACI structural Journal*, 106(1), 78.

Sharma, H., Gardoni, P., and Hurlebaus, S. (2014). "Probabilistic demand model and performance-based fragility estimates for RC column subject to vehicle collision." *Engineering Structures*, 74, 86-95.

Sharma, H., Hurlebaus, S., and Gardoni, P. (2012). "Performance-based response evaluation of reinforced concrete columns subject to vehicle impact." *International Journal of Impact Engineering*, 43, 52-62.

Shkolnikov, M. B. "Strain rates in crashworthiness." *Proc., Proceedings of 8th International LS-Dyna Users Conference, Troy, MI, USA*.

Steel, K., and Sorensen, A. D. (2014). "Reliability Analysis of a Circular Bridge Pier Subject to Intentional Vehicular Impact." *Vulnerability, Uncertainty, and Risk: Quantification, Mitigation, and Management*, 2702-2709.

Van Doormaal, J., Weerheijm, J., and Sluys, L. (1994). "Experimental and numerical determination of the dynamic fracture energy of concrete." *Le Journal de Physique IV*, 4(C8), C8-501-C508-506.

Weerheijm, J. (1992). "Concrete under impact tensile loading and lateral compression." Ph.D thesis, TU Delft, Delft University of Technology

Wu, Y., Crawford, J. E., and Magallanes, J. M. "Performance of LS-DYNA concrete constitutive models." *Proc., 12th International LS-DYNA users conference*, 3-5.

Xu, X., (2017). "*Performance based approach for loading and design of bridge piers impacted by medium weight trucks*." Ph.D thesis, City College of New York, City University of New York.

Yi, Z. (2009). "*Blast load effects on highway bridges*." Ph.D thesis, CITY UNIVERSITY OF NEW YORK.

Zimmerman, R. (2012). *Transport, the Environment and Security: Making the Connection*, Edward Elgar Publishing.

Zineddin, M., and Krauthammer, T. (2007). "Dynamic response and behavior of reinforced concrete slabs under impact loading." *International Journal of Impact Engineering*, 34(9), 1517-1534.

Publication FHWA-HIF-18-062